Colloidal Ordering
Under External Electric Fields

by

Ning Li

A Thesis Submitted in Partial Fulfilment of

the Requirements for the Degree of

Master of Science

Department of Physics and Physical Oceanography

Memorial University of Newfoundland

March 27, 2008

St. John's Newfoundland

Abstract

Colloidal science is an important branch of "soft condensed matter", which incorporates insights from chemistry, physics and biology. In this thesis, I will present the synthesis of fluorescently labeled core-shell silica colloids, and the laser scanning confocal microscopy studies of these colloidal silica particles under an external linear or rotating high-frequency alternating electric field. The external AC field controls the averaged dipolar interaction between the silica microspheres. We investigated bond order parameters upon increasing the field and found the threshold of the field to form dual-particle bonds and the average bond direction dependence on the field. We also studied the pair correlation function of these silica colloids in external electric fields. Moreover, we studied the equilibrium sedimentation profiles of these colloidal suspensions and found the dependence of isothermal osmotic compressibility on the applied electric field energy.

Acknowledgements

I thank my supervisor Dr. Yethiraj for his great help during our research and my thesis correction.

I would also like to thank several others: Dr. Leunissen for her help on Poisson Superfish software; Mr. van Kats for his generous synthesis advice; Dr. Saika-Voivod and Dr. Agarwal for their cooperation and helpful discussions in our research; Mr. Fitzgerald for our collaborative set up of electric field simulations and gold-coated electrodes for sample cells; Mr. Newman for collaboration in particle tracking IDL programming; Dr. Morrow, Dr. Poduska, Dr. Merschrod, Dr. Clouter, and Mr. Gulliver for their help with instruments; Dr. Davis (Chemistry Department Head) and Mr. Gulliver for use of their first-year laboratory in the summer of 2006; Mr. Whelan in the Physics Machine Shop for making the masks for gold coating; and again Dr. Agarwal for all the photographs he took for my thesis.

Contents

Abstract **i**

Acknowledgements **ii**

1 Introduction **1**

1.1 Colloids 2

1.1.1 Definition of Colloids 2

1.1.2 Forces in Colloidal Systems 4

1.2 Colloids in External Electric Fields 9

1.3 Experimental Methods in Colloidal Study 13

2 Experimental Preparation **21**

2.1 Synthesis Of Colloidal Silica Microspheres 22

2.1.1 Nonfluorescent Silica Particles 23

2.1.2 Fluorescent-Labeled Silica Particles 34

2.1.3 Seeded Growth of Core-Shell particles 40

2.2 Image Processing of Confocal Images Using IDL 57

2.2.1 General Method for Particle Tracking 58
2.2.2 Structural Analysis of Colloidal System 63
2.3 Electric Field Simulation and Construction 75
2.3.1 Simulation of Electric Field 75
2.3.2 Design and Construction of Electric Field Cells 83

3 Experiments, Data Analysis and Results 97
3.1 Experimental Procedures 98
3.1.1 Sample Preparation 98
3.1.2 Experimental Setup 103
3.1.3 Experiment Procedure 106
3.2 Data Acquisition, Analysis and Results 113
3.2.1 Data Acquisition 113
3.2.2 Order Parameter Analysis and Results 120
3.3 Conclusions 143

Outlook 147

Bibliography 149

A IDL procedures 155

B Igor Pro procedures 175

List of Tables

2.1 Diameters and flow rates of peristaltic tubing 47

2.2 Summary of centrifuge and ultrasonication conditions for different particle sizes 54

2.3 Summary of seeded growth 55

List of Figures

1.1 Schematic diagram of DLVO theory 7

1.2 Dipole-dipole interactions 10

1.3 Schematic setup of confocal system 15

1.4 Schematic drawing of conjugate focal pinhole 16

1.5 Airy disk 17

1.6 x-y view confocal image of core-shell silica colloids 18

1.7 x-z view confocal image of core-shell silica colloids 19

2.1 Ethanol distillation setup 25

2.2 Schematic drawing of TEOS distillation setup 27

2.3 SEM image of nonfluorescent silica particles NL0 28

2.4 SEM image and size distribution of NL1 and NL2 35

2.5 Sketches of chemicals 37

2.6 Fluorescent-labeled silica seeds 41

2.7 Tubing setup for seeded growth 46

2.8 Schematic drawing of seeded growth setup 49

2.9 SEM images of core-shell silica particles. 53

2.10 A frame from confocal image of core-shell silica particle 57
2.11 Identify Particles with IDL 61
2.12 Example of the particle number density distribution from a three-dimensional image stack. 71
2.13 Completed electric field cells 76
2.14 Side-view sketch of linear field electrodes. 78
2.15 Simulation result of linear field geometry. 79
2.16 Example image of an acceptable range in side-view linear field simulation 81
2.17 Example image of an acceptable range in top-view rotating field simulation 84
2.18 The design of the linear field mask 86
2.19 Brass mask for linear field. 87
2.20 The designing sketch of the rotating field mask 89
2.21 Brass mask for rotating field. 90
2.22 The gold-film-electrodes coated on glass slides for two-electrode linear field cell. 91
2.23 The gold-film-electrodes coated on glass slides for four-electrode rotating field cell. 91
2.24 Completed two-electrode linear field cell. 95
2.25 Completed four-electrode rotating field cell. 96
2.26 Overlap of the “wire” part of the four-electrode cell 96

3.1 Sketch for four-electrode cell electric set up 104
3.2 Z steps and bin of histogram 108
3.3 Example of sedimentation profile 110
3.4 Bond density vs brightness threshold from Experiment S1 . . . 115
3.5 Features found vs volume fraction for Experiment S1 116
3.6 E_0 vs Λ 119
3.7 Experiment S1: Bond density vs ϕ profile 120
3.8 Two bonded particles 122
3.9 Experiment L1: Bond density vs volume fraction profile 124
3.10 β_1 vs Λ 125
3.11 Experiment S1: $\langle \cos^2 \theta \rangle$ vs ϕ profile 127
3.12 Bond angle parameter vs volume fraction profile for Experiment L1 128
3.13 α_0 vs Λ 130
3.14 Experiment S2: α_0 vs $\langle E^2 \rangle$ 132
3.15 g(r) vs r/σ in Experiment S1 135
3.16 g(r) vs r/σ in Experiment L1 136
3.17 Pair correlation function at the first peak for Experiments S1, S2 and L1 137
3.18 Experiment S1: ϕ vs Z_p 140
3.19 χ_{T} vs Λ 141

Chapter 1

Introduction

In this chapter, we will introduce colloids, colloidal interaction forces and colloidal phase behavior. We will also review the effect of external electric fields on colloidal suspensions. Finally, the primary experimental method we used in the work of this thesis, confocal microscopy, will be described.

1.1 Colloids

1.1.1 Definition of Colloids

In 1861 Thomas Graham first gave the name *colloid* to the substances in an aqueous solution which could not pass through a parchment membrane when he was studying osmosis, after the Greek $\kappa o\lambda\lambda\alpha$ meaning glue [1]. He deduced that the low diffusion rates of colloidal particles implied they were fairly large, at least 1 nm in modern terms. On the other hand, the failure of the particles to sediment implied they had an upper size limit of approximately 1 μm. Fluid or solid particles in this size range dispersed in a fluid medium are known as colloidal dispersions. Graham's definition of the range of colloidal particle sizes is still widely used today [2]: for example, polymer solutions, blood cells and paint are all colloidal dispersions.

Colloidal particles normally have at least one characteristic dimension at the length range of a few nanometers to a few micrometers, which are much larger than the surrounding medium molecules so that the medium can be regarded as a continuum characterized by macroscopic properties such as density, dielectric constant and viscosity. But on the other hand, the colloidal particles are small enough to undergo Brownian motion, a phenomenon caused by fluctuations in the random collisions of medium molecules [1].

Use of colloids dates back to the earliest records of civilization, such as stabi-

lized colloidal pigments used in Stone Age cave paintings and manipulation of colloidal systems involved in ancient pottery making [2]. In the modern world, colloids still play an important role in science and industry. The food industry is a typical example that uses colloid techniques, as well as the production of paints and ceramic. Colloidal science is an important branch of "soft condensed matter", which incorporate subjects such as chemistry, physics and biology. The properties of colloids that interest physicists are their potential to invent novel materials by controlling crystallinity (such as photonic bandgap materials) or by controlling rheological properties (such as electrorheological fluids, which we will discuss more in the next section), as well as their function as a model system to study condensed matter.

As a model system of condensed matter (i.e. atoms and molecules), colloids had been shown in the 1970's [3] to have structures and inter-particle forces which can be treated in the same way as in simple liquids. Therefore, statistical mechanical concepts used in the theory of simple liquids can be analogized to an ensemble of colloids, leading to, for example, similar equations of state when the pressure is replaced by osmotic pressure. Indeed, the phase behavior of colloidal systems, such as freezing and melting of colloidal crystals, shows striking resemblance to that of atomic or molecular systems. The thermodynamic analogy can be utilized to experimentally study condensed matter theories [2]:

- The large size of colloids (1nm - 1μm) allows for easy experimental

techniques to probe colloids, such as light scattering and microscopy. But for atomic or molecular systems this is either very difficult or impossible.

- Also due to the large size of colloids, the typical time scale for colloidal processes is long enough to study real-time dynamics of colloidal particles using simple microscopy techniques.

- Phase transitions can be easily achieved in colloids by changing the particle and solvent properties, or adding an external field such as an electric field or a magnetic field. One can easily modify inter-particle forces in colloids; this is too difficult or perhaps impossible for atomic or molecular systems.

1.1.2 Forces in Colloidal Systems

The forces in colloidal systems play a critical role in studies of colloidal dynamics and phase behavior. The simplest model is to assume all colloidal particles are hard-sphere like, which means there is no interaction between colloidal particles beyond their radius but there is infinitely large repulsion between particles on contact. The phase behavior of hard-sphere colloids was studied by Pusey and van Megen [4, 5]. The only parameter that determines the phase behavior of ideal hard-sphere particles is the volume fraction of particles, ϕ. In a dilute system ($\phi \to 0$), particles are far away from each other and behave like a dilute gas. So long as $\phi < 0.49$, the system will be-

have like a fluid. If we keep increasing ϕ the system will show a fluid-crystal coexistence phase for $0.49 < \phi < 0.54$. For $\phi > 0.54$, the colloids behave like a solid. The system can be compressed up to $\phi = 0.74$ which is the maximum volume fraction for close packing. However, Pusey and van Megen [5] also showed that the system can be trapped in an amorphous or glass phase when ϕ is larger than approximately 0.58 and well below 0.64, the volume fraction of random close packing of spheres.

Most real colloidal systems are normally more complicated than hard spheres, because forces other than short-range repulsion exist in colloidal systems, which also lead to a richness in the phase behavior. A short discussion about forces in colloidal dispersions is presented here (we only discuss the simple case, i.e. size-monodispersed spherical particles in pure liquid or electrolyte solution) [1, 2, 6, 7]. Forces between colloidal particles and solvent include:

- Brownian force, which represents the thermal energy of molecular chaos, has a magnitude of $O(k_{\mathrm{B}}T/\sigma)$, where k_{B} is Boltzmann's constant, T is absolute temperature, and σ is a representative length, e.g. particle diameter (same below).

- Viscous force on a particle moving at a velocity v through a medium of viscosity η is $O(\eta\sigma v)$.

Inter-particle forces include:

- The attractive van der Waals force between two colloidal particles (also

known as the dispersion force) may cause aggregation for colloidal particles. One can calculate the dispersion force by summing over van der Waals forces from all pairs of molecules from different particles [8], resulting in a magnitude of $O(H\sigma/h)$ at short particle separations. The Hamaker constant H depends on the nature of the particles and the medium in between. h is the separation between two particles.

- The repulsive electrostatic double-layer forces can keep the colloidal system stable against the dispersion force. In most cases, particularly in polar media, colloidal particles possess an electrostatic charge due to the dissociation of their surface groups, which will get them charged and repulsing each other. The colloidal suspension as a whole is electrically neutral, so the counterions in the solvent move onto the particles and form an electrostatic double-layer, which affects considerably the electrostatic forces between colloidal particles. The final repulsive electrostatic double-layer force is of a magnitude of $O(Ce^{-\kappa h})$ at short particle separations, where C is a constant, h is the separation, and κ^{-1} is called the Debye-Hückel screening length (or Debye length). The Debye length here is normally much smaller than particle size in colloidal systems (close to hard spheres), and can be decreased by increasing solvent ionic strength (i.e. salt concentration) in colloidal dispersions. κ^{-1} is an important parameter indicating the "softness" of the dispersion, about which we will show more details in 3.1.1.

- Derjaguin and Landau (1941) and Verwey and Overbeek (1948) independently explained the stability of colloids by combining the attractive dispersion force and repulsive electrostatic double-layer force, which is commonly known as the DLVO theory. In this theory the free energy of interaction in its simplest form is [7]:

$$V_{int} = -\frac{Ha}{12h} + Ce^{-\kappa h} \ , \tag{1.1}$$

where a is particle radius. From DLVO theory we can obtain the schematic diagram of the variation of free energy with particle separation, which is shown in Figure 1.1. The DLVO theory proposes that

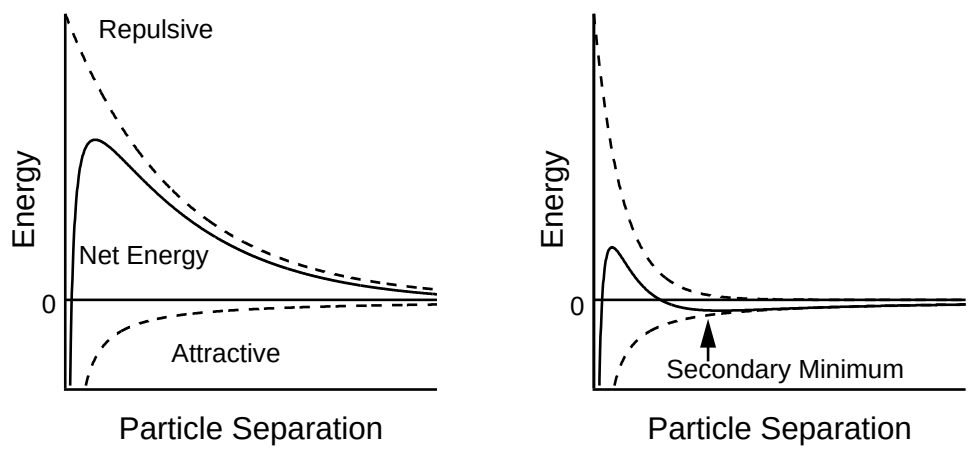

(a) Free energy vs. particle separation. (b) At higher salt concentrations.

Figure 1.1: Schematic diagram of the variation of free energy with particle separation according to DLVO theory [9]. The two pictures correspond to different κ^{-1}. (a) The net energy is given by the sum of the double layer repulsion and the van der Waals attractive forces that the particles experience as they approach one another. (b) The diagram at higher salt concentrations shows the possibility of a secondary minimum.

an energy barrier resulting from the repulsive force prevents two particles from approaching one another and adhering together (Figure 1.1a). But if the particles collide with sufficient energy to overcome that barrier, the attractive force will pull them into contact where they adhere strongly and irreversibly together. In certain situations (e.g. in high salt concentrations), there is a possibility of a "secondary minimum" where a much weaker and potentially reversible adhesion between particles exists (Figure 1.1b). These weak flocs are sufficiently stable not to be broken up by Brownian motion but may dissociate under an externally applied force such as vigorous agitation.

Besides particle-solvent interactions and inter-particle interactions, external fields also play an important role in colloidal phase behavior. The most common external field is gravitation, which gives the effective gravitational force (combined with buoyancy) $F_g = \frac{4}{3}\pi a^3 \Delta\rho g$ for spherical colloidal particles, where a is particle diameter and $\Delta\rho$ is density difference between particle and surrounding fluid and g is acceleration due to gravity. Gravitational force is negligible if the gravitational length $l_g = k_\mathrm{B}T/F_g$ is much larger than particle diameter. But in our case it is not negligible as $l_g \approx 2a$ (we have $l_g = 1.92$ μm for Experiment S1 and S2 (0.77 μm diameter spheres) and $l_g = 0.59$ μm for Experiment L1 (1.14 μm diameter spheres)). External electric or magnetic fields are also important methods to modify inter-particle forces and therefore easily modify phase behaviors in colloidal systems. We will introduce external electric fields, which are more interesting in our case,

in the next section.

1.2 Colloids in External Electric Fields

Colloidal particles in an external electric field whose dielectric constant is different from that of the nonpolarizable solvent acquire an electric dipole moment parallel to the external field [10]. The behavior of the colloids is governed by the dipole-dipole interaction, whose strength can be tuned by the magnitude of the field. Since their rheological properties (viscosity, yield stress, shear modulus, etc) can be reversibly changed by the external field, such suspensions are called electrorheological (ER) fluids. Similarly there exists magnetorheological (MR) fluids for external magnetic fields.

The energy of dipolar interaction shown in Figure 1.2a [10] is given by [11]

$$U_{dip}(R,\theta) = -\frac{4\pi\varepsilon_0\varepsilon_f\beta^2 a^6 E_0^2}{R^3}\left(\frac{3\cos^2\theta - 1}{2}\right) , \tag{1.2}$$

where $\beta = \frac{\varepsilon_p - \varepsilon_f}{\varepsilon_p + 2\varepsilon_f}$, ε_p and ε_f are dielectric constants for colloidal particles and the surrounding fluid, and a is the particle radius. E_0^2 here is the local field energy, where $\vec{E}_0$, for the simplest case, is a high frequency (mega-Hertz) sinusoidal AC field. The field frequency is so high that particles can only see an averaged field and the effects of ion migration are minimized. θ is the angle between separation $\vec{R}$ and $\vec{E}_0$. R here is limited to be much

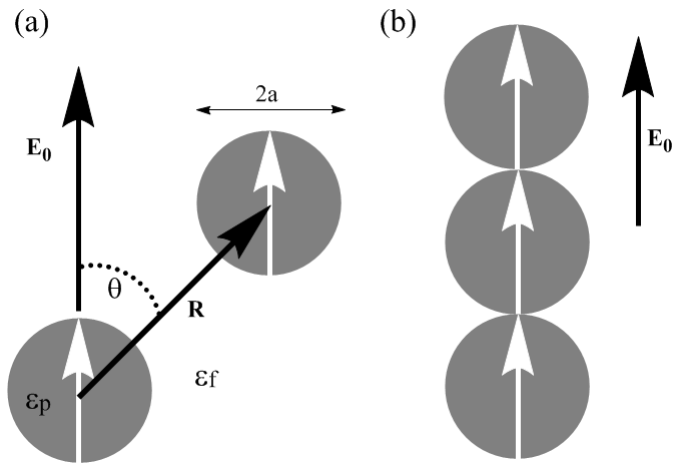

Figure 1.2: Dipole-dipole interactions. (a) Field induced dipoles (white arrows) on colloidal particles with radius a interact with each other. (b) When field is strong enough colloidal particles form a chain along field.

greater than particle radius, i.e. $R \gg a$, given that the dipole induced by the external field is not affected by neighboring particles, known as the point-dipole approximation. We can see that three salient characteristics from Equation 1.2 are:

- Angular dependence. The interaction switches sign at $\theta_0 \approx 54.7°$ where $3\cos^2\theta - 1 = 0$. So the dipolar interaction is attractive when $\theta < \theta_0$, and repulsive when $\theta > \theta_0$. This leads to head-to-toe chain formation of colloidal particles when the field is strong enough (see Figure 1.2b).

- Particle size dependence. U_{dip} strongly depends on a as it changes as a^6.

- The interaction can be tuned by external field, which provides a convenient method for studying phase transition in colloids as the dipo-

lar interaction dominates in colloids when the applied field is strong enough.

In addition, we introduce the "lambda parameter" Λ describing the relative strength of electric dipolar energy to thermal energy:

$$\Lambda = \frac{\pi \varepsilon_0 \varepsilon_f \beta^2 a^3 E_0^2}{2 k_{\mathrm{B}} T} \ . \tag{1.3}$$

Λ is dimensionless as it is the ratio of dipolar energy to thermal energy. Here a^6/R^3 is reduced to $\frac{1}{8}a^3$ as the particles closely interact ($R \to 2a$). We can rewrite the dipolar energy as:

$$\frac{U_{dip}(R,\theta)}{k_{\mathrm{B}} T} = -\frac{\Lambda}{(R/\sigma)^3} \left(\frac{3\cos^2\theta - 1}{2} \right) \ , \tag{1.4}$$

where $\sigma = 2a$ is the diameter of spheres.

Since the late 1980's, the equilibrium structure of ER fluids has seen a resurgence and is an interesting subject for many theoretical and experimental studies. In an earlier theoretical study on electric field induced phase transition, Tao *et al.* found that the colloidal system experiences a liquid-solid phase transition when the applied field exceeded a critical strength [12]. Later Tao and Sun proposed the structure for the ground state of the induced ER solid to be a body-centered-tetragonal (bct) lattice with $\mathbf{a_1} = \sqrt{6}a\hat{\mathbf{x}},\ \mathbf{a_2} = \sqrt{6}a\hat{\mathbf{y}},\ \mathbf{a_3} = 2a\hat{\mathbf{z}}$, where a is the particle radius [13].

Then Tao *et al.* confirmed this structure with Monte Carlo simulation [14] and a laser diffraction experiment [15]. With the development of confocal microscopy (which will be introduced in the next section), real-space studies of colloidal structures became possible. The three-dimensional bct structure of silica colloidal spheres was first observed with confocal microscopy by Dassanayake *et al.* [16].

Yethiraj *et al.* demonstrated the tunability of the "softness" and the dipolar interactions of density matched colloidal dispersions by changing the salt concentration and external electric field, and the corresponding phase diagrams mimicking atomic crystals [17]. The real-space access of colloidal structures *via* confocal microscopy, combined with the tunability through external fields, provides a powerful method to study colloidal phase behavior and therefore gives better understanding of phase transitions in atomic systems such as the melting transition [17] and the martensitic transition (i.e. a diffusionless crystal-crystal transition) [18].

Colloids form chains along a linear external AC electric field, but will not "crystallize" into the bct structure if the volume fraction of colloidal particles is low. The kinetics of the colloidal chain-growth at relatively high fields (kV/cm) has been extensively studied using different methods such as digital video microscopy [19] and light scattering [20]. However, quantitative investigations into the low field (and low volume fraction) situation where

colloidal particles start to approach their nearest neighbors and form two-particle-bond have not been done yet. Our research addresses the following issues (see chapter 3 for detail):

- Characterization of colloid structure at low electric fields ($\Lambda \lesssim 300$) and low volume fraction ($\phi \lesssim 30\%$) with various order parameters (bond density order parameter β_1, bond orientational order parameter α_0, as well as the pair correlation function g(r)).

- The feasibility of modifying colloid structure dramatically by switching from linear to rotating electric fields

- The use of gravitational sedimentation profiles to detect apparent osmotic compressibility (χ_{T}) in almost hard-sphere-like colloids.

1.3 Experimental Methods in Colloidal Study

The techniques typically used to study colloids fall into three categories [6]: scattering (such as x-ray, neutron and laser scattering), rheology and microscopy. Light scattering, which normally uses laser light in the visible spectrum, is the most popular technique among scattering techniques as the wavelength of the scattering source is close to the size of colloidal particles. This technique accurately measures both structure and dynamics of colloidal suspensions by averaging over large ensembles of the colloidal system, but fails to probe details of local structure on the single particle level. The

rheological technique, which studies the response of the colloids to external perturbations [21], is also not appropriate for our study because it lacks a direct probe into short length scale structure unless incorporated with optical techniques [22,23]. In principle, optical microscopy can be used as a probe of local structure. But obtaining three-dimensional structure information from conventional optical microscopy is impossible.

In order to study the local two-particle-bond formation in colloids, we used laser scanning confocal microscopy (confocal microscopy for short), which, when combined with refractive index matching and colloids with fluorescent labeled core and nonfluorescent labeled shell (see chapter 2 for more detail), has numerous advantages compared to conventional optical microscopy and other techniques as shown below.

Better resolution

A laser scanning confocal microscope incorporates two principal ideas [6]: point by point illumination of the sample and rejection of out of focus light. Figure 1.3 shows a basic optical path in a typical confocal microscope: Laser source (black line) coming out of a screen with pinhole (P1) is directed by a dichroic mirror to two mirrors which can respectively scan in the x and y directions. The laser then passes through the microscope objective and excites the fluorescent sample. The frequency of fluorescent light (gray line) emitted from sample objects is lower than that of the laser, as its photon en-

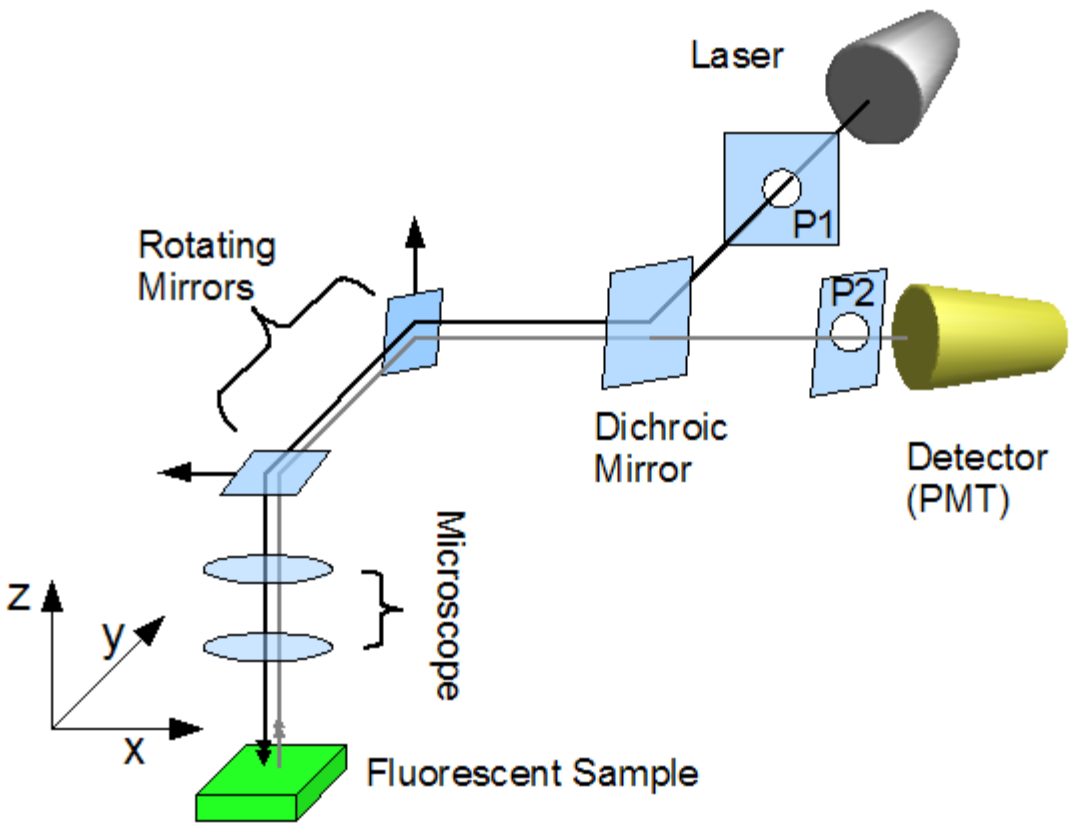

Figure 1.3: Schematic setup of confocal system. P1 and P2 are two screens with adjustable pinhole. Black line is incoming laser light, gray line is excitation light from fluorescent sample.

ergy is lower than the absorbed photon. The emitted fluorescent light goes back through the same path as the laser and passes the dichroic mirror as its frequency is lower than the laser (i.e. longer wavelength). Finally, the fluorescent light passes a pinhole (P2) placed in the conjugate focal (hence the term confocal) plane of the sample (see Figure 1.4). Therefore the light out

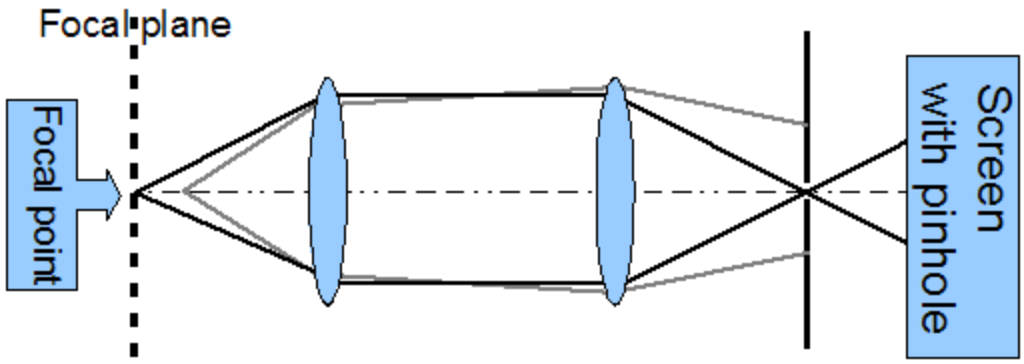

Figure 1.4: Schematic drawing of conjugate focal pinhole showing the function of pinhole: in the confocal microscope system, only the light signal from the conjugate focal point of the pinhole in front of the detector can pass through the pinhole. This focal point is the place we observe our fluorescent sample. Light from any position out of focus (gray line) will be excluded by the pinhole.

of focus will be excluded by the pinhole and only the in-focus sample emitted light can finally reach the detector such as a photomultiplier tube (PMT).

The resolution of the confocal microscope is higher than conventional optical microscopes not only because pinhole P2 rejects light out of focus, but

also due to the function of P1 [24]. We know that the image of a point laser source is not a perfect point but an Airy disk, whose intensity mainly concentrates in the center as shown in Figure 1.5. The light intensity distribution

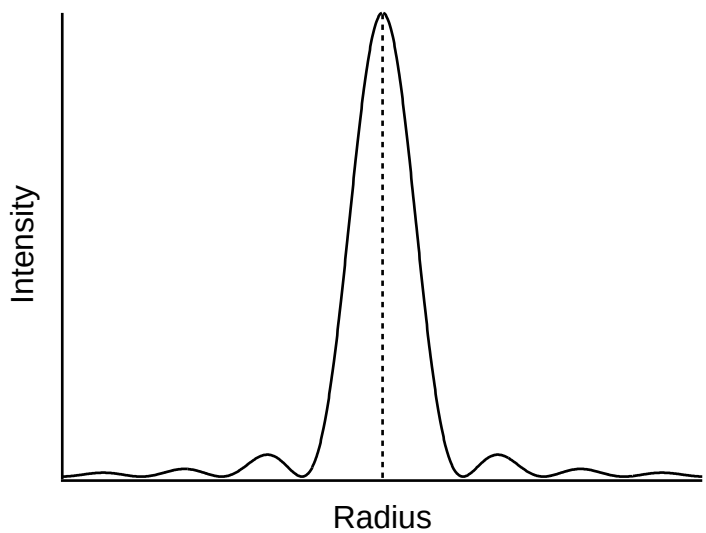

Figure 1.5: Intensity vs Radius diagram of a Airy disk. Central dash line is located at zero radius, i.e. center of the light spot.

is given by the point-spread function (PSF) of the microscope lens system. In the focal plane PSF is ideally given by [25]

$$I(\nu) = \left(\frac{2J_1(\nu)}{\nu}\right)^2 , \tag{1.5}$$

where $J_1(\nu)$ is the first-order Bessel function, $\nu = 2\pi(NA)r/\lambda = kr(NA)$, r is the distance from the center point, and $NA = n\sin\theta$ is the numerical aperture of the lens (n is refractive index of immersing medium of the lens and θ is half the total collecting angle of the lens). From Equation 1.5 we

obtain that the first minimum of intensity occurs at radius $r_1 = 0.61\lambda/NA$. Within this about 82% of the total intensity is included. On the other hand, the distribution of excitation fluorescent light in the plane of detection is proportional to the square of the PSF. Therefore, we use the P1 pinhole to make our laser source close to a perfect point light source, which can greatly enhance the resolution of the detected image from excitation light. Figure 1.6 shows a confocal image of almost monodispersed core-shell silica colloids with 1.14 μm diameter (3.4% polydispersity) and 0.47 μm fluorescent core.

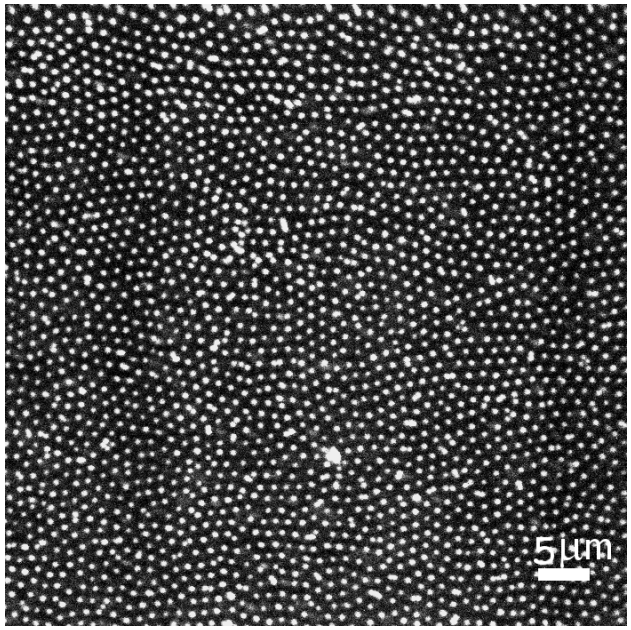

Figure 1.6: x-y view confocal image of 1.14 μm core-shell silica colloids. This is the bottom layer of a sample with approximately 4% volume fraction. The area shown in this image is 60μm×60μm, 1× magnification.

The localization of the image of the point laser source is even worse along

the z direction (i.e. along the optical axis). The PSF for a plane containing the optical axis is given by a different form:

$$I(u) = \left(\frac{\sin(u/4)}{u/4} \right) \ , \tag{1.6}$$

where $u = 2\pi(NA)^2 z/(n\lambda) = k(NA)^2 z/n$, z is the distance along the optical axis. Here the first minimum is normally larger than that of the x-y plane, which explains why we need to zoom the x dimension by a factor of 2 to get a more spherical looking (shown in Figure 1.7) side view of colloids sediment as the particles in z direction appear to be longer than actual size (see more details in 2.2.2).

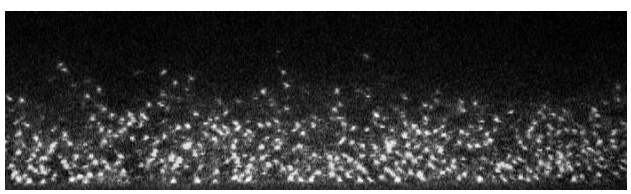

Figure 1.7: x-z view confocal image of core-shell silica colloids. Rebuilt confocal image for the side view of sedimented 0.77 μm silica colloids, where zoomed ratio is x:z = 2:1.

In addition to optical resolution enhancements from confocal imaging, the core-shell silica colloidal sample also gives better effective resolution because only the fluorescent cores contribute to the signal; the nonfluorescent shell is invisible in a refractive index matched medium. Thus the signal from two touching spheres is well separated. For example, the white dots in Figure

1.6 are actually the fluorescent cores of touching core-shell spheres. Most of them appear to be well separated except for a few aggregates and impurities.

Probe a sample deep inside

Conventional microscopy suffers from the multiple scattering problem which is caused by the scattered light from objects when imaging deep into a sample. However, a sample with the refractive index of objects (which are fluorescent labeled) matched to that of surrounding medium can solve this problem. Multiple scattering light is minimized and only the fluorescent light from the labeled objects will be collected. Besides, refractive index matching can also minimize the attractive dispersion force preventing unwanted sample aggregation.

In the following chapters, we will introduce our experimental preparation for colloidal study utilizing confocal microscopy, detailed procedures of experiments and finally the results and discussion.

Chapter 2

Experimental Preparation

This chapter describes the experimental tools required for the confocal microscopy research presented in this thesis, including:

- Section 2.1, fluorescent-nonfluorescent core-shell microspheres synthesis for confocal microscopy samples.
- Section 2.2, IDL programming for confocal image processing.
- Section 2.3, electric field construction for external field applied on our samples.

2.1 Synthesis Of Colloidal Silica Microspheres

This section describes the synthesis of core-shell spherical colloidal silica particles. The synthesis followed Stöber's method [26] and Giesche conditions [27, 28], and the experimental details also followed a recent M.Sc. thesis [29] and the work of van Blaaderen *et al.* [30].

This method is based on the hydrolysis of tetraethyl orthosilicate (TEOS) and subsequent condensation of silica in an alcoholic solution of water and ammonium hydroxide under certain reaction conditions. The silica condensation forms a porous network and grows isotropically from the nuclei and finally forms spherical particles. The core-shell particle synthesis consisted of two stages. The first stage was the synthesis of fluorescent-labeled silica seeds with a fluorescent dye for confocal imaging. In the second stage, a nonfluorescent shell was grown onto these cores. A two-stage synthesis has three advantages: the nonfluorescent shell can separate the fluorescent cores and give a better resolution for confocal microscopy; the shell will also protect the fluorescent core and suppress the bleaching of the dye while imaging; moreover, the growth of the shells on the fluorescent seeds can decrease the polydispersity of the seeds.

2.1.1 Nonfluorescent Silica Particles

Nonfluorescent silica particles (batches name NL1, NL2, NL7, where NL stands for Ning Li, and the numbers indicate synthesis sequence for different batches) were prepared from TEOS in a solution of ethanol, water and ammonium hydroxide. The reaction process is described by these two steps:

$$\mathrm{Si(OC_2H_5)_4 + 4H_2O \xrightarrow[\text{ethanol}]{NH_3} Si(OH)_4 + 4C_2H_5OH} \tag{2.1}$$

and

$$\mathrm{Si(OH)_4 \xrightarrow[\text{ethanol}]{NH_3} SiO_2 \downarrow + 2H_2O} \tag{2.2}$$

The silica condensate, which has a microscopic structure of disordered networks, was the spherical colloidal particles we produced.

Materials preparation

Anhydrous ethyl alcohol (Commercial Alcohols Inc., bp 78 ℃) was freshly distilled before use (the general rules for the chemistry experiments we did followed a chemistry laboratory manual [31]). We used an existing ethanol distillation setup courtesy of Professor Morrow (Figure 2.1 shows the setup). First some boiling stones were added to the two-neck round-bottom flask (2 Liter capacity), and then anhydrous alcohol was added to two thirds of the whole flask volume. One of the necks was closed after adding alcohol, the other one was connected to a water cooled distillation column, with a graded

capacity of 125 mL. All the joints of glassware were clamped to prevent unwanted falling or pop-up. The bottom of the two-neck flask was held by a heating mantle. A power setting of "35% " on the variac power display corresponded to the stable temperature for distilling alcohol (slightly higher than the bp of alcohol). Water cooling was turned on before heating started, and was carefully controlled not to be too strong or too weak during the whole distillation, by watching the oil pressure indicator connected to the inner environment of the distillation column. The inner pressure was slightly higher than 1 atm. When alcohol condensate started to form, it was kept refluxing back to the two-neck flask for about 15 minutes to suppress possible organic impurities. Collection of the alcohol condensate in the distillation column was then begun. As the capacity of the column was limited, the distilled alcohol was transferred to another container when the column was full (approximately 100 mL). In case there was any impurity in the distilled alcohol releasing path, the first 100 mL was discarded. When the alcohol left in the flask was less than approximately 100 mL, heating was stopped and water cooled for another 30 minutes.

TEOS (Fluka, purum, $\geq$ 98.0%, bp 168 ℃) was also freshly distilled before use. Three round-bottom flasks (500 mL, 24/40 joint) were washed with 95% alcohol and dried in the oven before use. One of the flasks was filled with some boiling stones at the bottom, and TEOS to two thirds of the flask volume. The schematic for this setup is shown in Figure 2.2. The flask with

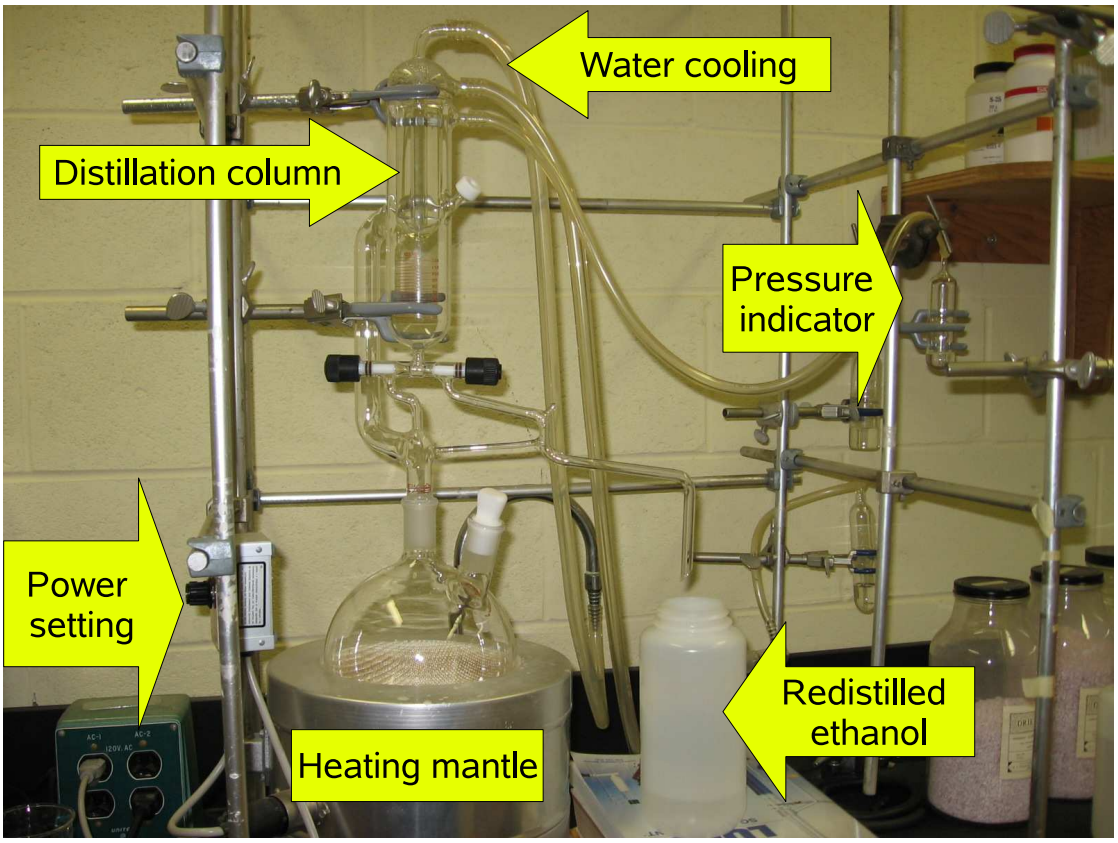

Figure 2.1: Ethanol distillation setup: in the photograph, the cylindrical heating mantle is holding the two-neck round-bottom flask. The distillation column with water cooled tubing is sitting on the straight neck of the flask, held by clamps. The distilled ethanol will come to the white plastic container when the right screw (black cap) of the distillation column is loosened.

boiling stones was held by a heating mantle and a metal lab jack. It was connected to a condenser (air cooled) by a three-way adapter, with the other end of the adapter closed by a stopper. The condenser was connected to a vacuum adapter, connected to another 500 mL round-bottom flask for collecting TEOS condensate, and also to a drying tube to prevent hydrolysis of TEOS. A variable transformer (Powerstat, 3PN116C) was used as power supply for the heating mantle, and "85" (out of "140") on power display gave a stable temperature for TEOS distillation (slightly higher than the bp of TEOS). The dropping rate of condensed TEOS was about 3 drops per second. To suppress the impurity of TEOS, the first 20 mL were discarded. All the joints of glassware were clamped. Heating was stopped when the original TEOS left in the first flask was less than approximately 30 mL.

The distillation of TEOS was necessary because the trial we attempted without distilling TEOS, named as NL0, had the result that the particles were not as spherical as NL1,2,7, which is clear from the comparison SEM images of NL0 colloids (Figure 2.3) and SEM images of NL1 and NL2 colloids (Figures 2.4a, 2.4c). This may be due to premature hydrolysis of TEOS in the undistilled TEOS, which can be excluded by distilling it.

Ammonium hydroxide (28% to 30%, Caledon) was of reagent grade. Sulfuric acid (95% to 98%, Caledon) and hydrogen peroxide (29% to 32%, ACP) were used for making "piranha" solution. Distilled water was taken from

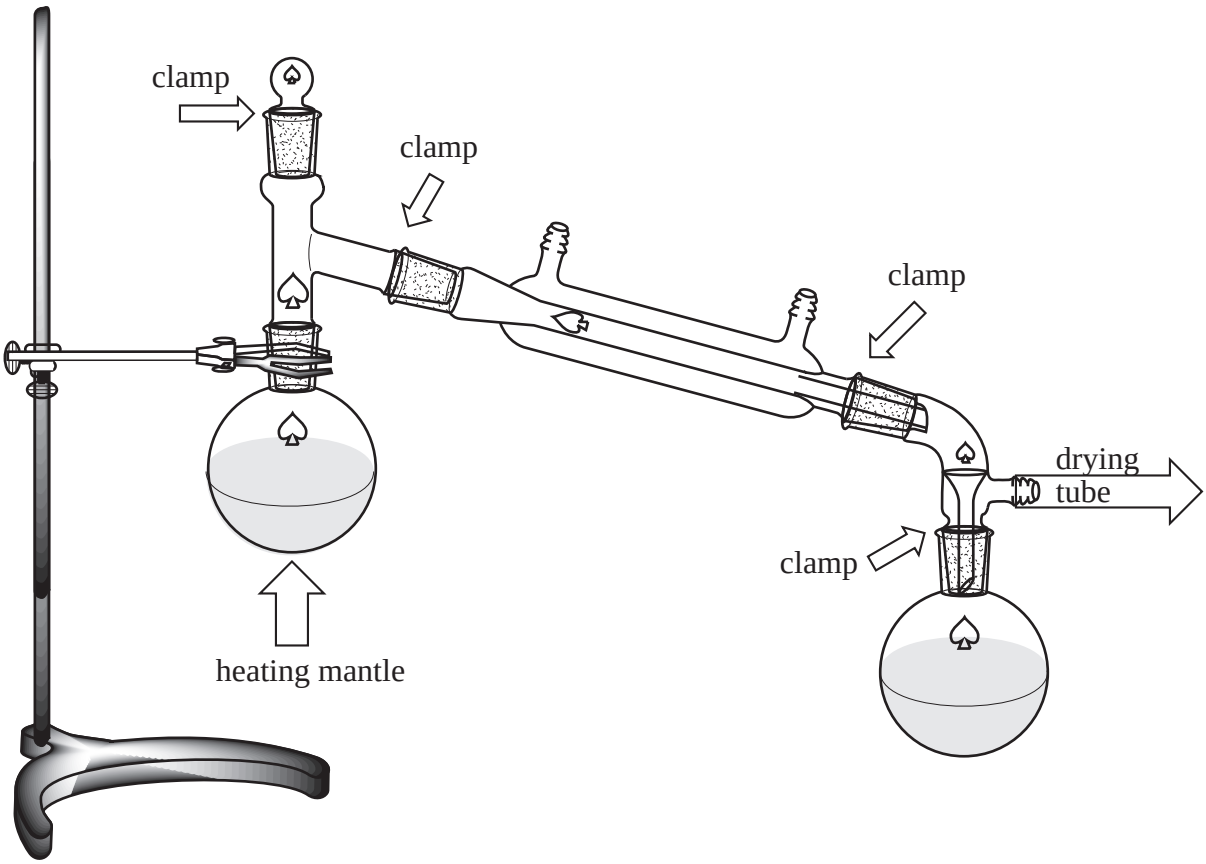

Figure 2.2: Schematic drawing of TEOS distillation setup

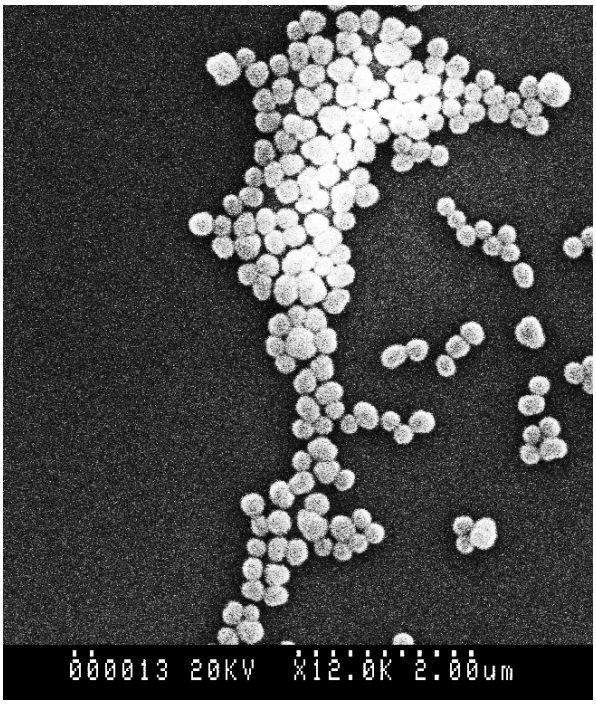

Figure 2.3: SEM image of nonfluorescent silica particles NL0

Barnstead Fi-Streem III GlassStill system (at the lab of Professor Poduska). 95% alcohol (Commercial Alcohols Inc.) was used for cleaning. An analytical balance (Mettler, AE260) was used for all mass measurements. A centrifuge (Sorvall, Legend Mach 1.6) was used after synthesis for separating the colloids from water and ammonium hydroxide. Fisherbrand 50 mL Falcon centrifuge tubes and 1.5 mL micro tubes (Sarstedt) were used for centrifugation. Colloids were redispersed after centrifugation by placing in an ultrasonic bath (Bransonic, model 8510R-DTH) for a few hours. Small amounts of liquid were taken by Fisherbrand disposable glass pipettes, and small amounts of powder were taken by Fisherbrand spatula. Measuring

small amounts of liquid was done by pipettors (Fisherbrand, finnpipette II) and tips of same brand, or by 5 mL syringes (HSW). A Fisher Isotemp 500 Series oven was used for the drying of glassware. A hot plate stirrer (Barnstead Thermolyne) and a stir bar (PTFE-coated, 1 in. $\times$ 1/3 in.) was used for stirring and heating the reaction vessel.

Equipment Preparation

A 1 L three-neck round-bottom flask, a 250 mL Erlenmeyer flask, as well as a 50 mL and a 100 mL measuring cylinder, were used in synthesis. All glassware (including the magnetic stir bar) was washed with piranha solution. Face shield and thick rubber gloves must be used for protection when using piranha solution, as it is a strong oxidizer. The piranha washing was done in a fume hood. A 2 L beaker filled with tap water was prepared next to the fume hood, in order to wash off any piranha solution on the gloves. To make piranha solution, 70 ml of sulfuric acid was first added into the 100 mL measuring cylinder, then 30 ml of hydrogen peroxide was added into the same cylinder. One should always add the peroxide into the acid, not the other way around. The mixing reaction of peroxide and acid is exothermic, so the mixture became very hot immediately after mixing. The hot piranha solution was carefully transferred into the round-bottom flask. Three glass stoppers (joint 24/40) were used to close all the openings of the flask and held tightly with hands in case of pop-ups. The flask was slowly rotated in ordered to wet the inside of the flask completely with piranha solution. The

solution was then transferred back to the 100 mL cylinder and kept in there for a few minutes before transferring back to the flask. This procedure was repeated three times to clean the 100 mL cylinder and 1 L flask. The same procedure was used to clean the 50 mL cylinder and the 250 mL Erlenmeyer flask. Once finished, the piranha solution was transferred to a glass bottle or a beaker and neutralized with soda ash before disposing into a sink. All glassware washed with piranha solution was rinsed with distilled water until the pH was 7 ("Accutint" pH indicator was used). They were then rinsed with 95% alcohol and dried in the oven.

Colloid Synthesis Setup and Procedure

The synthesis was done in the fume hood. The set up was as follows: the middle neck of the three-neck round-bottom flask was held on the frames in the fume hood; the stirrer was then placed under the flask. The height of the clamp was adjusted to ensure the bottom of the flask was close to the surface of the stirrer, so that the stir bar could smoothly stir.

Since the capacity of our reaction vessel was 1 L, the total amount of reagents should not exceed approximately 700 mL. Therefore, the amount of reagents were scaled down from the data in Dannis 't Hart's thesis [29]. 525 mL of distilled anhydrous alcohol, 52.5 mL of ammonium hydroxide and 21 mL of TEOS were used in this synthesis, having the total amount of 598.5 mL.

First, 250 mL Erlenmeyer was used to transfer 125 mL distilled alcohol into the round-bottom flask through the right hand side opening. 52.5 mL of ammonium hydroxide was then transferred to the flask through the same opening by the 100 mL cylinder. Another 200 mL of alcohol was then transferred through this opening in order to rinse the ammonium hydroxide on the wall of the flask, which otherwise may cause a high concentration of ammonium hydroxide in that area and affect the result. After adding alcohol and ammonium hydroxide, the stirrer was started to mix the ethanol and ammonium hydroxide. TEOS was then added through the left hand side opening by the 50 mL cylinder, under a vigorous stirring. This should be done as fast as possible to suppress the hydrolysis of TEOS in the air. The openings of the flask should be closed by the three glass stoppers during the whole synthesis.

The reaction start time was recorded. After one minute, the stirring speed was slowed down to a gentle stirring so that there was only a shallow vortex at the center of the surface of solution (approximately 200 rpm). After 10 minutes the solution turned slightly milky, indicating the silica started condensing. Within 60 minutes, the solution turned very milky, indicating most of the silica condensate already formed. The gentle stirring was continued for 5 hours. The colloidal suspension was then transferred to twelve 50 mL Falcon tubes.

Particle Transfer

The synthesized colloids were transferred as soon as possible to an ethanol medium for two reasons. A high ammonium hydroxide concentration, i.e. a high pH, gives a high ionic strength, which can decrease the thickness of the double layer (see 1.1.2 for more details) of the particles, destroy the charge stability and shorten the distances between particles. Although the increased pH here, which is above the isoelectric point of silica (about 3), may cause more surface group dissociation and finally increase the surface charge of silica microspheres, the decreasing of the electrostatic double layer still dominates and turns out to overcome the repulsive effect of the increased surface charge. The van der Waals force between these particles, however, is only very strong at short distances. So this force may cause irreversible aggregation to the particles approaching each other at short distances. Besides, the smell of ammonium hydroxide may cause inconvenience when working with these colloids. Therefore, the colloidal suspension was centrifuged to separate silica particles and the solution containing ammonium hydroxide.

An 800 rpm $\times$ 4 hours centrifugation was used for these nonfluorescent silica particles (NL1, NL2, NL7). After centrifugation, most of the particles sedimented to the bottom and the supernatant was clear. The Falcon tubes were then carefully taken out from the centrifuge, and kept vertical in case the sediments redisperse to the solution. The supernatant was then removed with glass pipettes. The tubes were then refilled with anhydrous ethanol (not

redistilled), and ultrasonicated in the ultrasonic bath for a few hours. Water cooling (via a lab-made copper tube coil in the ultrasonic bath) was used for long-time ultrasonication, as the ultrasonication heated the water in the bath. Redispersion of colloids is more efficient if accompanied by frequent vortexing. There is a trade off between centrifuge time and ultrasonication time. If one use high-speed centrifugation, shorter time is needed for colloids sedimentation, but longer time is required to redisperse by ultrasonication; on the other hand, lower speed of centrifugation need longer time to sediment the colloids, but shorter time is required for redispersion. The exact time and speed of centrifuge were different for different particles (see Table 2.2 for detailed centrifuge and ultrasonication time).

This centrifugation, decantation, adding fresh ethanol and redispersion procedure was repeated 3 times or more, until there was no ammonia smell in the colloids. One can also test the pH of the colloids to ensure there is no ammonium hydroxide left. The colloids were then transferred to a glass bottle, and labeled by the batch name.

Polydispersity Analysis

Particle size distribution and polydispersity was obtained using scanning electron microscope (SEM) images of silica particles dried on a glass substrate. The dried particles might appear slightly smaller on SEM than the size measured with light scattering techniques, which give the real hydrodynamic size

of particles. These images were analyzed using an image-processing software ImageJ (version 1.37v) and statistics done using a graphical analysis software Igor Pro (version 5.03). The procedure was as follows: a line was manually drawn across the center of each particle in the SEM image to get a diameter of each particle, with correct scale setting from the scale bar on the SEM image. The diameters were recorded in a graphical analysis software Igor Pro and the statistics were obtained. The average particle diameter of nonfluorescent silica colloids NL1 (Figure 2.4a) was 0.37 μm, with a polydispersity of 14.1% (Figure 2.4b), and NL2 (Figure 2.4c) was 0.34 μm, with a polydispersity of 9.4% (Figure 2.4d). The SEM images and particle size distribution of NL1 and NL2 are shown in Figure 2.4. We are not sure about why the polydispersity of NL2 was smaller than NL1, why the particle size distributed into two peaks and why the polydispersity was not as small as those in the Giesche conditions (see Table 1 in [27]) which was approximately 5 to 10%, and that in the work of van Blaaderen and Vrij (approximately 5%) [30]. The possible reason could be the variance in the room temperature for different batches of synthesis.

2.1.2 Fluorescent-Labeled Silica Particles

The purpose of fluorescent-labeling silica particles was to facilitate imaging of confocal microscopy. The synthesis of fluorescent-labeled silica colloids used a procedure from van Blaaderen and Vrij's article [30]. This procedure consisted of two steps: first, the dye was chemically bonded to a

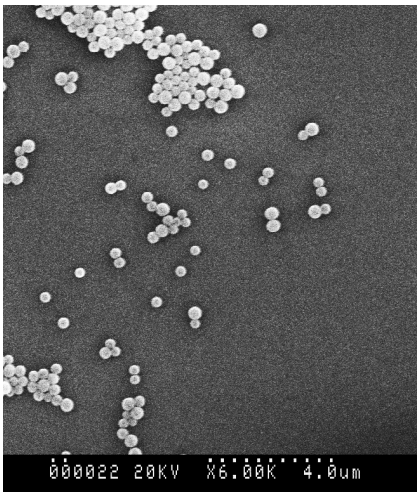

(a) SEM image of nonfluorescent silica particles NL1

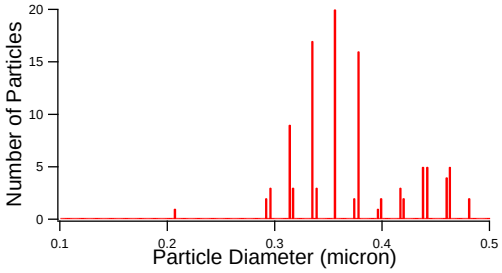

(b) Particle size distribution of NL1. Statistics obtained from 3 images containing 105 particles.

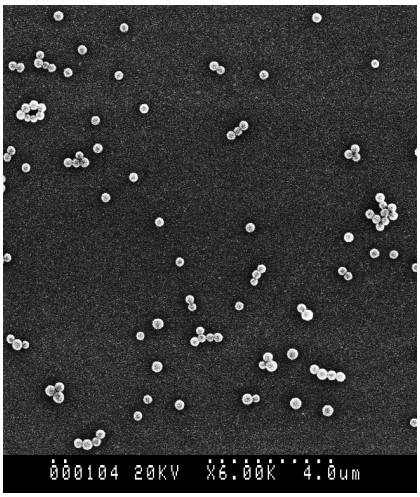

(c) SEM image of nonfluorescent silica particles NL2

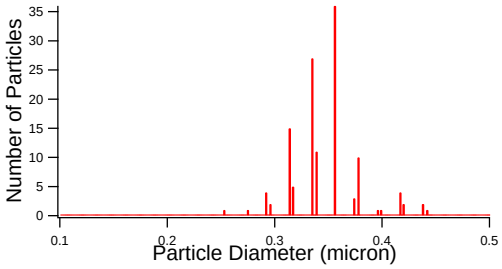

(d) Particle size distribution of NL2. Statistics obtained from 2 images containing 126 particles.

Figure 2.4: SEM image and size distribution of NL1 and NL2. The particles were actually well separated and the clusters were formed upon drying on the substrate (same for the following SEM images).

silane coupling agent; second, this coupling agent was used in the hydrolysis and condensation of TEOS, as described in section 2.1.1, which was based on the Stöber method [26]. The silane coupling agent used here was (3-Aminopropyl)triethoxysilane (APS) (Figure 2.5a). Only one of the four groups bonded on Si of APS is different from TEOS (Figure 2.5b), which make APS capable to bond with the dye, fluorescein isothiocyanate (FITC) (Figure 2.5c), and finally coat on silica spheres (Figure 2.5d [30]).

Materials Preparation and Synthesis Procedure

Distilled TEOS and anhydrous alcohol were made in the same way as before. The other chemicals were also the same as before except APS (Fluka, purum, $\geq$ 98.0%) and FITC (Fluka, $\geq$ 90%).

The amount of reagents was scaled down from the data in the thesis of Dannis 't Hart [29]: 0.0732 g of FITC, 0.426 g of APS, 3 g of ethanol, and same amount of chemicals (525 mL of ethanol, 52.5 mL of ammonium hydroxide and 21 mL of TEOS) as before in pure silica synthesis. The glassware washing and instruments setup were also the same as before.

First 525 mL of ethanol and 52.5 mL of ammonium hydroxide were added to the 1 L three-neck round-bottom flask and mixed, using the same procedure as before.

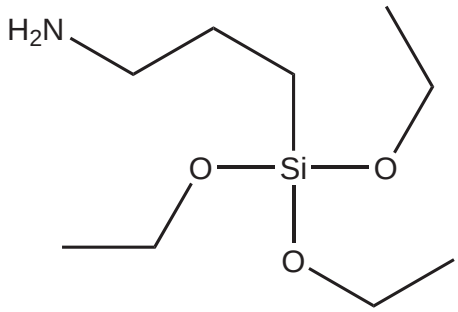

(a) (3-Aminopropyl)triethoxysilane (APS)

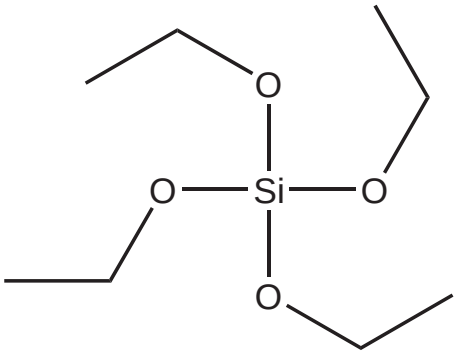

(b) tetraethyl orthosilicate (TEOS)

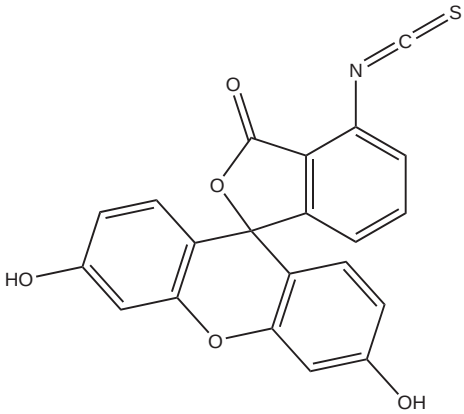

(c) fluorescein isothiocyanate (FITC)

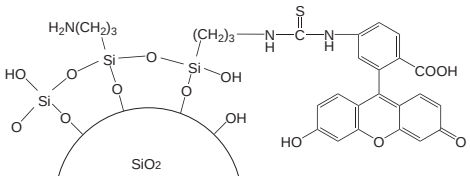

(d) FITC-APS coated on a silica sphere, from reference [30]

Figure 2.5: Sketches of chemicals

Then the balance and a 20 mL disposable scintillation vial and a small stir bar (both cleaned with distilled anhydrous ethanol and dried beforehand) were used to make the FITC-APS solution. The procedure was as follows. First, measure the mass of the glass bottle (with stir bar in it), rezero the balance after the display is stable. Second, take 450 μL of APS by using a pipettor (APS density 0.946 g/mL) and add it into the bottle. Measure the mass of the whole bottle and record the display on the balance. Since the balance was rezeroed after measuring the bottle and the stir bar, the display should be the mass of APS. Again rezero the balance after use. Third, add 3.8 mL distilled anhydrous ethanol (0.789 g/mL) into the bottle, measure the mass and rezero the balance. Finally, use a spatula to add 0.0732 g of FITC powder into the glass bottle and measure the mass. The actual masses measured for FITC powder could be slightly larger than expected, which could help to over fluorescent-label the particles and gave better image quality for confocal microscopy. It is important to make the FITC-APS solution as fast as possible to suppress the possible hydrolysis of APS and bleaching of FITC, especially the former.

Once the solution was made, the glass bottle was covered with aluminum foil and put on a stirrer for better mixing. After approximately 15 minutes, which was different from the stirring time in the work of van Blaaderen and Vrij (12 hours) [30], the solution was clear and showed a dark red color.

21 mL distilled TEOS was then added to the round-bottom flask under vigorous stirring. The FITC-APS mixture was then added from the other neck immediately. After one minute, the stirring speed was turned down to a gentle stirring (200 rpm). The sash (covered with aluminum foil beforehand) of the fume hood was lowered in order to suppress the bleaching of FITC.

The solution turned milky as before, but with an orange color instead of white. After 5 hours stirring, another 3 mL of distilled TEOS and 3 mL of distilled water were simultaneously added from two necks to coat the resulting particles with a thin pure silica layer, in order to protect the fluorescent dye of the particles.

The same procedure as NL1 and NL2 was used for particle transfer. The two batches of FITC silica seeds made by the same procedure were labeled as NL3 and NL5.

Polydispersity Analysis

Again the procedure of polydispersity analysis was the same as before. NL3 (Figure 2.6a) had a average diameter of 0.47 μm and a polydispersity of 6.9% (Figure 2.6b). The polydispersity of NL3 was smaller than NL1 and NL2, for as yet unknown reasons.

RBITC Labeled Silica Seeds

We also attempted to synthesize a batch (NL10) of Rhodamine B isothiocyanate (RBITC) labeled silica seeds [32]. RBITC has the similar structure (Figure 2.6d) as FITC but is less bleachable than FITC. The procedure used was all the same as the FITC seeds synthesis, except the mass of the fluorescent dye. The molecular weight is 389.38 for FITC, but 536.08 for RBITC (Sigma, mixed isomers). For the same moles of fluorescent dye, 100 mg RBITC (the total amount in a fresh bottle of RBITC) was used by putting APS and ethanol in the RBITC bottle. The resulting particles (Figure 2.6c) had the same diameter as FITC seeds, but were more likely to aggregate when centrifuged and therefore more difficult to redisperse afterward. This was possibly due to different surface groups of RBITC labeled silica particles, which could lead to different surface charges from FITC labeled silica particles.

2.1.3 Seeded Growth of Core-Shell particles

The second step of core-shell particle synthesis was seeded growth, based on the fluorescent-labeled seeds. A predetermined amount of TEOS/ethanol mixture and ammonium hydroxide/water/ethanol mixture were added dropwise (through a dual-channel peristaltic pump) into the previously prepared seed suspension, under gentle stirring. A nonfluorescent shell then grew on the fluorescent nuclei and finally formed core-shell silica particles.

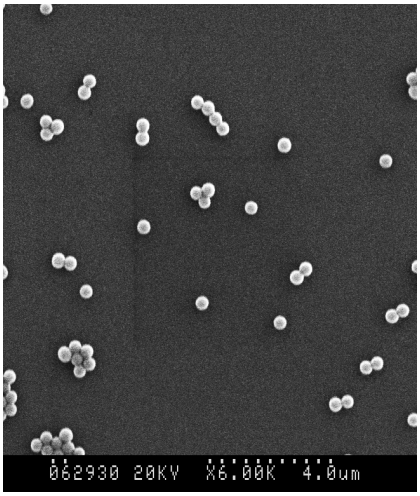

(a) SEM image of FITC labeled silica seeds NL3

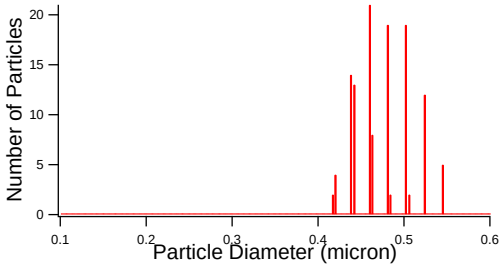

(b) Particle size distribution of NL3. Statistics obtained from 5 images containing 121 particles.

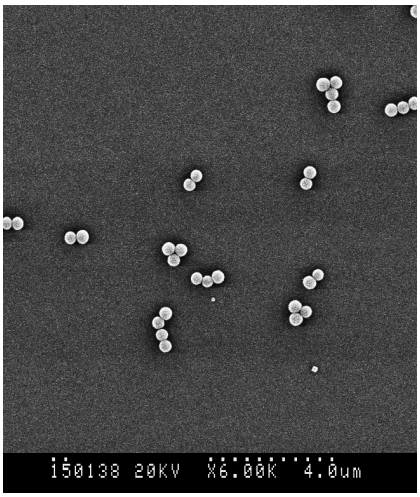

(c) SEM image of RBITC labeled silica seeds NL10

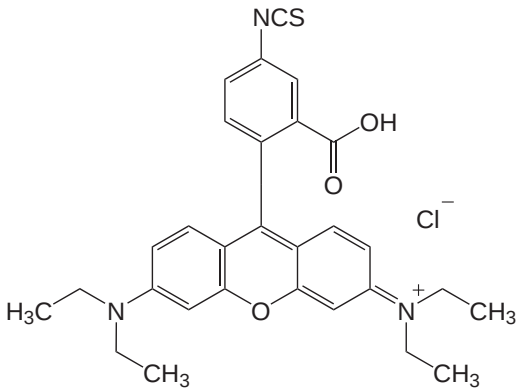

(d) Rhodamine B isothiocyanate (RBITC)

Figure 2.6: Fluorescent-labeled silica seeds

Care must be taken during the synthesis. Too low seed concentration in suspension gives a large diffusion distance of the hydrolyzed TEOS to the particles surface [28], which may induce premature hydrolysis and condensation of TEOS, and leads to the secondary nucleation, the formation of unwanted small silica nuclei in the seed suspension. On the other hand, too high a seed concentration increases particle clustering, leads to unwanted particle aggregates, which is difficult to separate from the monodisperse suspension by centrifugation.

Similarly, at too low concentration of ammonium hydroxide, the particle surface potential may be too low to stabilize the particles; however, too high pH may decrease the double layer thickness, the electrostatic repulsion barrier, and consequently reduces particle stability. So one must carefully control the concentration of the reagents.

Giesche [28] gives empirical guidelines for optimal results (a practical guide but not a strict limit):

- the concentration of SiO_2 in the seed suspension should be less than 1 M (i.e. 1 mol/L) and preferably between 0.5 and 0.8 M
- the ammonium hydroxide concentration between 0.5 and 0.7 M
- the water concentration about 8M

Materials preparation

Freshly distilled TEOS, anhydrous ethanol (not distilled, following [29]), ammonium hydroxide and distilled water were used as before.

The seed suspension consisted of 31 mL of concentrated FITC labeled seeds (80 g/L), 44mL ethanol, 11 mL water and 4 mL ammonium hydroxide. A high concentration of seeds in ethanol was obtained using the procedure as follows:

- Measure the concentration of the original seeds (using the oven), estimate the required amount.
- Centrifuge the seeds of required amount, remove the extra ethanol and redisperse them using ultrasonication.
- Measure the concentration of these concentrated seeds to see if more original seeds needed.
- Since there will be another 44 mL ethanol in the seed suspension, one only needs to concentrate the original seeds to a concentration of 33.07 g/L and take 75 mL of this.

When measuring the concentration, a small disposable glass vial (1 mL capacity) was first washed with 95% ethanol and dried in the oven. The mass of the dried bottle was then measured. 500 μL of seed suspension was then added in the bottle, dried and measured again. From the mass difference we

got the mass of silica per unit volume of suspension. To ensure the silica were completely dried in the oven, the drying and measuring procedure was repeated a few times more until there was no difference of the mass. To minimize the error, final data was taken from the average of three batches of measurements.

Equipment Preparation for Seeded Growth

A significant amount of equipment and optimization was required for the seeded growth set up, and is described here.

Two cylindrical separatory funnels (capacity 500 mL, Graduated, PTFE stopcock, 24/40 joint, Exeter), a three-neck round-bottom flask (500 mL or 1 L, depends on the final volume of all reagents of use, 24/40 joints), and all other glassware was washed with piranha solution using the same procedure as before.

A dual-channel peristaltic pump (Gilson, minipuls3, Mandel) was used for dropwise addition of the reagents at the same rate through two channels. The tubing system for this pump was made following the principle that tubing diameter should never be increased downstream. For each channel, 3 pieces of tygon tubing (1/4 inch internal diameter (ID), 1/16 inch wall thickness; 1/8 inch ID, 1/16 wall thickness; and 1/16 inch ID, 1/32 inch wall thickness, respectively) were used to assemble a long tubing whose bigger end

was connected to the end of one separatory funnel and the smaller end was connected to the calibrated PVC tubing (Gilson, 0.38 mm ID, color coding orange/green, GF-F117933). The 1/4 inch ID tubing was directly assembled onto the end of the separatory funnel and sealed with parafilm (Figure 2.7 a); the 1/8 inch ID tubing was connected to the 1/4 inch ID tubing with a plastic connector and sealed with parafilm (Figure 2.7 b); the 1/16 inch ID tubing was jointed to the 1/8 inch ID tubing with super glue and sealed with Teflon (PTFE) tape (Figure 2.7 c); and the input end of the calibrated PVC tubing was jointed to the 1/16 inch ID tubing with super glue (Figure 2.7 d). The calibrated PVC tubing was the most important part of the whole tubing system, going through one of the two channels of the pump and directly affecting the flow rate. The flow rate and the pump rotating speed have a linear relation and the ratio for the tubing we used (0.38 mm ID) equals to 0.073 mL/min per 5 rpm (see Table 2.1 [33]). The output end of the calibrated tubing, coming out of the pump, was connected to a long extension tubing (same internal diameter, GF-F117953) with a metal sleeve (GF-F117985) (Figure 2.7 e). The other end of the extension tubing was assembled to a glass inlet tube (bleed type, 6mm, joint size 24/40, Kontes) and sealed with parafilm in order to suppress the reagent-air contact (Figure 2.7 f). This inlet tube helped to assemble the tubing onto the reaction vessel and form droplets into the seed suspension. The total length for the tubing was long enough to connect the separatory funnel and the round-bottom flask.

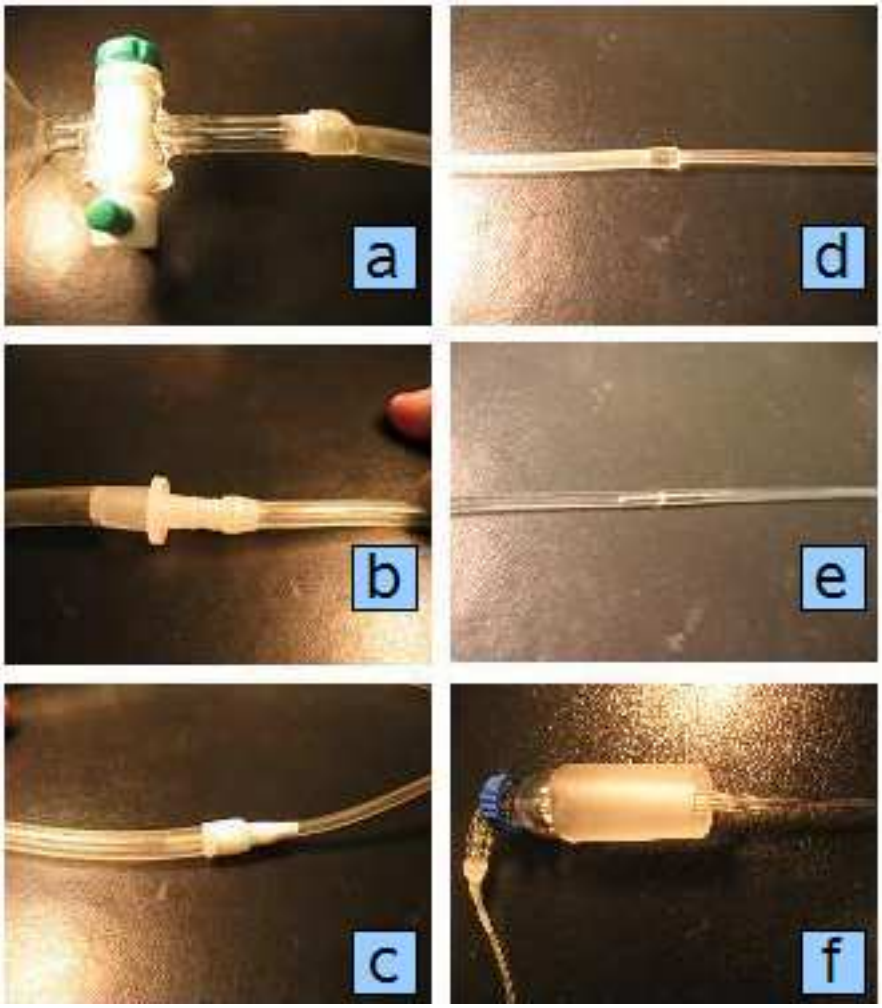

Figure 2.7: Tubing setup for seeded growth: (a) 1/4 inch ID tubing was directly assembled onto the end of the separatory funnel; (b) 1/8 inch ID tubing was connected to the 1/4 inch tubing by a plastic connector and sealed by parafilm; (c) 1/16 inch ID tubing was jointed to the 1/8 inch ID tubing by super glue and sealed by Teflon tape; (d) the input end of the calibrated PVC tubing was jointed to the 1/16 inch ID tubing by super glue; (e) the output end of the calibrated tubing was connected to a long extension tubing by a metal sleeve; (f) the other end of the extension tubing was assembled to a glass inlet tube and sealed by parafilm.

ID (mm)	Flow rate (mL/min)			
	5 rpm	15 rpm	30 rpm	48 rpm
0.38	0.073	0.219	0.436	0.695

Table 2.1: Diameters and flow rates of peristaltic tubing. The flow rate necessary for this synthesis was 5.1 mL/h, which equals to 0.085mL/min, corresponded to a pump rotation rate of 5.82 rpm.

Seeded Growth Setup

The synthesis was carried out in the fume hood. Reagents were added as follows:

- First transfer the 90 mL of seed suspension (75 mL of seeds and ethanol, 11 mL water, 4 mL ammonium hydroxide) to the round-bottom flask.
- Put the flask in a water bath (filled with tap water) on a magnetic stirrer, and fix the flask onto the frames.
- Adjust the height of the flask to get a smooth gentle stirring (approximately 200 rpm).
- Fix the separatory funnels onto the frames at a proper height and position in order to leave enough space for the tubing and flask.
- Connect the tubing system to the separatory funnels, install the calibrated part onto the pump, and fix the two inlet tube onto the two side necks of the flask (as they have the same size of joints).
- Use a three-way adapter to gently blow nitrogen into the flask and keep

the whole reaction under a nitrogen environment, in order to suppress the reaction between TEOS and the water vapor in the vessel.

A schematic drawing of this setup is shown as Figure 2.8. The stopper on the center neck three-way adapter was loosened a little because of gentle flowing of nitrogen.

Seeded Growth Procedure

Reagents were added into the separatory funnels after the seeded growth system was installed. Aiming at a final particle size of approximately 1 μm, the amount of TEOS needed was 159 mL following [27] and [29]. The maximum TEOS addition rate was 2.3 mL/h according to Giesche conditions. Therefore, a 2 M of TEOS solution was prepared by adding 190 mL of TEOS and 236 mL of ethanol in one separatory funnel (funnel A). A superfluous amount of solution was added in order to leave sufficient liquid in the funnel to keep the pump working properly during the whole seeded growth. A solution of 15.4 M water and 1.35 M NH_3 in ethanol was prepared by adding 100 mL of distilled water, 310 mL of ethanol and 38 mL ammonium hydroxide in another separatory funnel (funnel B). The molar concentration of our ammonium hydroxide (12.5 M), determined by titration, did not agree with 28% to 30% weight percentage (0.9 kg/L, approximately 15 M) labeled on the bottle. So the actual molar concentration of NH_3 in funnel B was 1.06 M (not 1.35 M as in [29]). This could be the possible reason that our results did not agree with the work in [29].

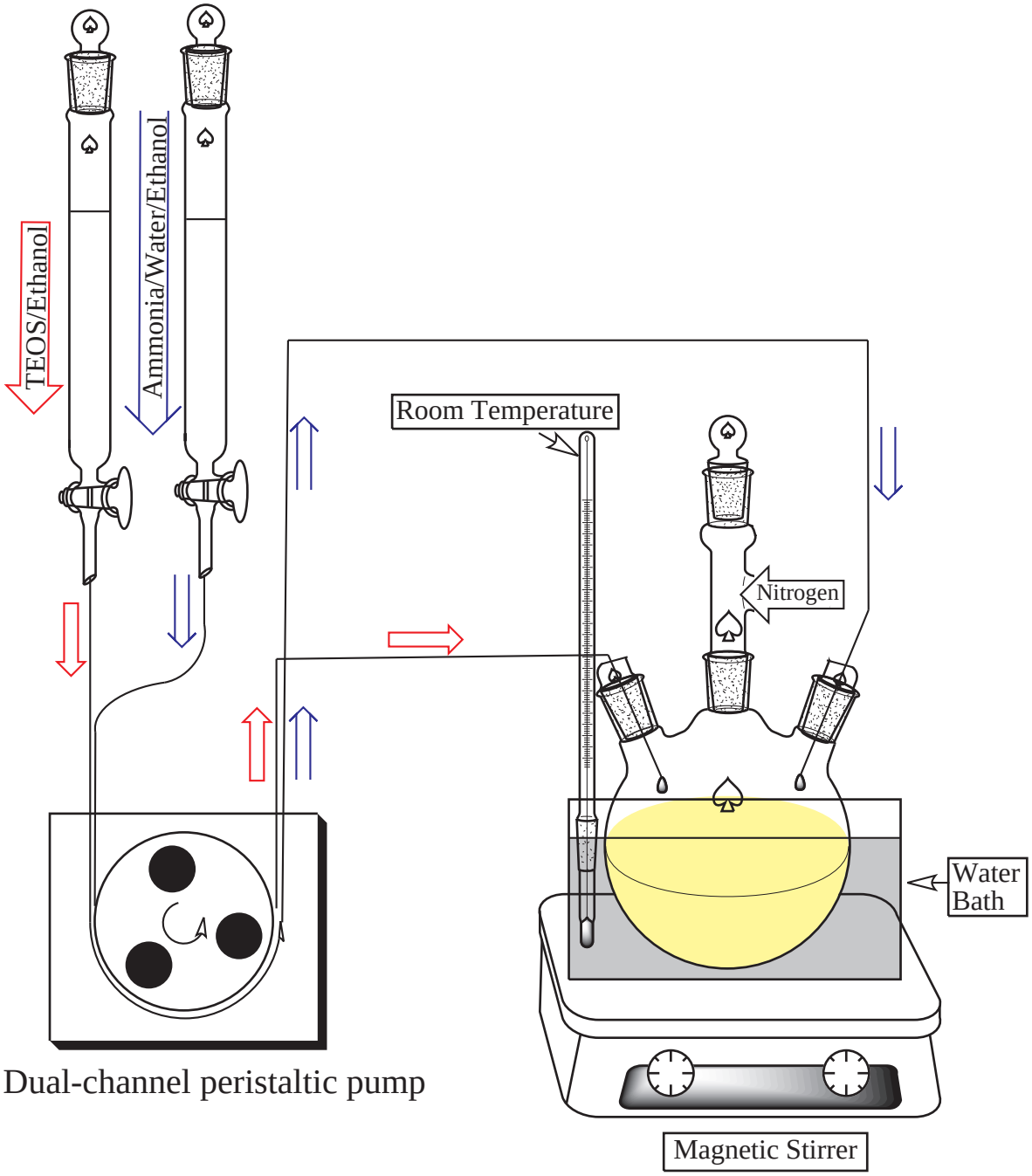

Figure 2.8: Schematic drawing of seeded growth setup

After filling with reagents, the funnels were filled with nitrogen and closed with stoppers, in order to protect the reagents with a nitrogen environment. The stopcocks of the two funnels were then opened and the liquid in the tubing could pass through. It is sometimes necessary to squeeze the tubing in order to exclude the air in it. Once the liquid passed through the pump (the calibrated part of tubing), the calibrated tubings were tightened by closing the compression cams and tightening the adjustment screws.

The cam pressure on the tubing was adjusted (by the adjustment screw) to the minimum necessary to ensure pumping of the liquid [34]. One should slowly tighten the screw until the pump starts pumping liquid inside the tubing (the front of the liquid starts to flow peristaltically), and then tighten again approximately 1/8 turn. Care must be taken not to over-tighten the screws in order to minimize wear on the calibrated tubing.

In order to get a 2.3 mL/h TEOS adding rate, 5.1 mL/h (equals 0.085mL/min) flow rate for TEOS solution in funnel A was used (same flow rate for funnel B). Therefore a pump head rotating speed of 5.82 rpm was used for this pump and this size of calibrated tubing (see Table 2.1). Since the rotating speed was the same for the two channels, the flow rates for these two tubing should be ideally the same. The hardening (by TEOS) of the calibrated tubing, however, leaded to a different amount of flattening and stretching

of the calibrated tubing by the pump, thus the actual flow rates were not the same for the two channels during the seeded growth. The longer time the seeded growth took, the worse this problem was. Careful adjustment of the screws was carried out after approximately 12 hours to decrease the difference of flow rate. The flow rate difference was controlled to be within 2 mL/h during the whole seeded growth (approximately 70 hours). This is an important area of possible improvement of particle monodispersity. Instead of PVC calibrated tubing, one can use other more durable calibrated tubing such as viton tubing.

The TEOS solution and ammonium hydroxide were slowly pumped through the two channels of tubing and finally dropped into the seed suspension through the glass tips of the inlet tube. It was important to ensure the droplets of reagent fall in the suspension directly (especially the TEOS solution) rather than fall on the wall of the vessel first. This was to avoid locally nonuniform concentration of reagent or any hydrolysis of TEOS before it reached the seed suspension, which could cause unwanted effects like secondary nucleation or aggregation.

Nitrogen gas was blown gently through the middle neck, preventing premature contact of the two reagent drips and unwanted hydrolysis of TEOS with the ambient atmosphere, should be very gentle that the stopper on the adapter can only be very slightly loosened because of the nitrogen blowing

out. The two separatory funnels were refilled with nitrogen approximately every 10 hours, in order to keep the pressure balance between the inside of outside of the funnels so that the pump can work properly.

The room temperature (outside the fume hood but in the lab), during the whole seeded growth, was 23 ℃; while the water bath temperatures were 21.5 ℃ for two batches NL6 and NL8 and 19 ℃ for NL9, without any noticeable fluctuation. The reason for the temperature difference between the room and water bath could be that the temperature inside the fume hood was actually lower than outside; and the reason for the water bath temperature difference between NL6/NL8 and NL9 may be different sizes of reaction vessels used for these batches (NL6/NL8 1 L, NL9 500 mL).

Particle Transfer and Polydispersity Analysis

The result particle transfer procedure was similar as before, using a lower centrifuge speed of approximately 500 rpm for 4 hours. The four batches of all seeded growth are NL4 (NL3S1, means first seeded growth of NL3 FITC seeds), NL6 (NL3S2), NL8 (NL5S1) and NL9 (NL5S2), as shown in Figures 2.9a, 2.9b, 2.9c, and 2.9d.

The polydispersity analysis was done in the same procedure as before. Table 2.2 summarizes the centrifuge speed and ultrasonication time used for differ-

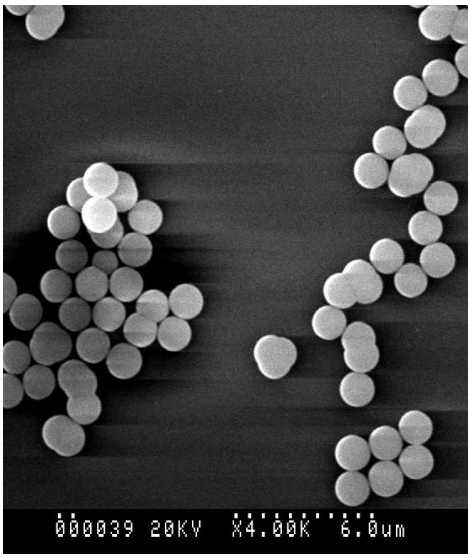

(a) SEM image of NL4. Lots of non-spherical aggregates.

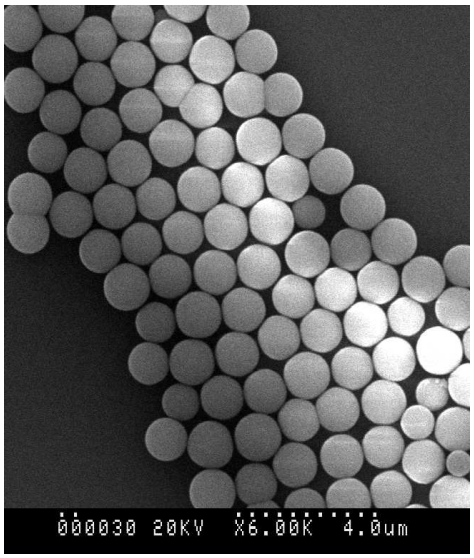

(b) SEM image of NL6. 1.27 μm diameter (4.1% polydispersity).

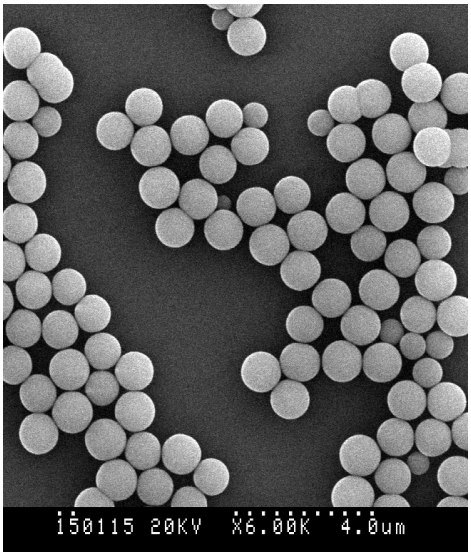

(c) SEM image of NL8. 1.14 μm diameter (3.4% polydispersity).

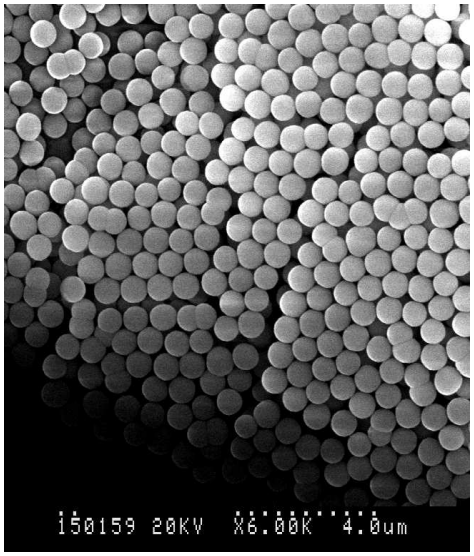

(d) SEM image of NL9. 0.77 μm diameter (3.8% polydispersity).

Figure 2.9: SEM images of core-shell silica particles.

ent batches.

Batch #	⌀ (μm)	Centrifugation (rpm × hours)	Ultrasonication (hours)
NL1	0.37	1150 × 3	2
NL2	0.34	1150 × 3	2
NL3	0.47	700 × 4	6
NL6	1.27	500 × 3	2
NL8	1.14	500 × 3	2
NL9	0.77	550 × 3	2

Table 2.2: Summary of centrifuge and ultrasonication conditions for different particle sizes. NL1,2,3 were centrifuged and ultrasonicated using different centrifuge (Sorvall) (thanks to Dr. Merschrod) and ultrasonic bath (NEY, 100 Ultrasonik).

The details of the three batches of seeded growth are summarized in table 2.3. The column "funnel A" and "funnel B" refer to the amounts of TEOS solution and ammonium hydroxide used in funnel A and B by the three batches (keeping the same ratio of 190 mL TEOS, 236 mL ethanol for TEOS solution and 38 mL ammonium hydroxide, 100 mL water and 310 mL ethanol for ammonium hydroxide). The columns "NH_3 (M)" / "H_2O (M)" show the start and end NH_3 / H_2O molar concentration in the reaction vessel. Taking NL6 as an example: we started with the 90 mL seed suspension, containing 4 mL of ammonium hydroxide (this was the same for all three batches), from which we can calculate that the beginning NH_3 concentration in the vessel was 0.56 M (using the titration result, i.e. 12.5 M NH_3 in ammonium hydroxide); after the synthesis was finished, 346 mL of TEOS solution and 376 mL of ammonium hydroxide had been added to the reaction vessel, from

Batch	funnel A	funnel B	NH_3 (M)		H_2O (M)		$\varnothing(\mu m)$	PD (%)
			Begin	End	Begin	End		
NL6	346 mL	376 mL	0.56	0.55	8.5	8.2	1.27	4.1
NL8	207 mL	248 mL	0.56	0.57	8.5	8.6	1.14	3.4
NL9	86 mL	84 mL	0.56	0.53	8.5	8.0	0.77	3.8

Table 2.3: Summary of seeded growth: "funnel A" and "funnel B" refer to the amounts of TEOS solution and ammonium hydroxide solution used in funnel A and B; "NH_3 (M)" / "H_2O (M)" show the start and end NH_3 / H_2O molar concentration in the reaction vessel; and the last two columns show the average particle diameter ($\varnothing$) and polydispersity (PD).

which we can calculate that the end NH_3 concentration was 0.55 M. Similarly we can calculate the beginning and end concentration of H_2O (8.5 M and 8.2 M) in the reaction vessel (there is 39.1 M water in our ammonium hydroxide). It is clear that the NH_3 concentration was between 0.5 and 0.7 M as Giesche's guideline, and the water concentration was approximately 8 M. The column "$\varnothing(\mu m)$" shows the average diameter of result particles, and "PD (%)" shows the polydispersity. Our seed suspension SiO_2 concentration was 0.46 M, slightly less than 0.5 M. This was fine because, as we mentioned before, Giesche's guideline is not a strict limit. The SiO_2 concentration (not listed in 2.3) was the same for all three batches (31 mL 80 g/L silica in ethanol, 44 mL ethanol, 11 mL water and 4 mL ammonium hydroxide).

The polydispersity of NL8 (NL5S1) is smaller than NL9 (NL5S2), because of the following reason: providing the same amount of hydrolyzed TEOS condensate, namely the same volume of silica shell grown on the silica sur-

face, the diameter increases slower as the diameter gets bigger (see Equation 2.3 [28], where $\varnothing$= diameter, M = mass). Therefore the polydispersity, the relative diameter difference between particles, becomes smaller as the particle diameter becomes bigger.

$$\left(\frac{\varnothing_{seed}}{\varnothing_{new}}\right)^3 = \frac{M_{TEOS,seed}}{M_{TEOS,total}} \tag{2.3}$$

However, the polydispersity of the largest particles NL6 (NL3S2), was bigger than that of the particles NL8 and NL9. This was probably due to the irreversible flattening of the calibrated tubing, which made the control of flow rate more and more difficult during the synthesis (especially after day 1), and finally created a lot of second nucleation at day 3 of NL6 seeded growth.

2.2 Image Processing of Confocal Images Using IDL

We use the confocal microscope to obtain gray scale intensity images (256 gray levels for 8 bit image) such as the one shown in Figure 2.10. We need

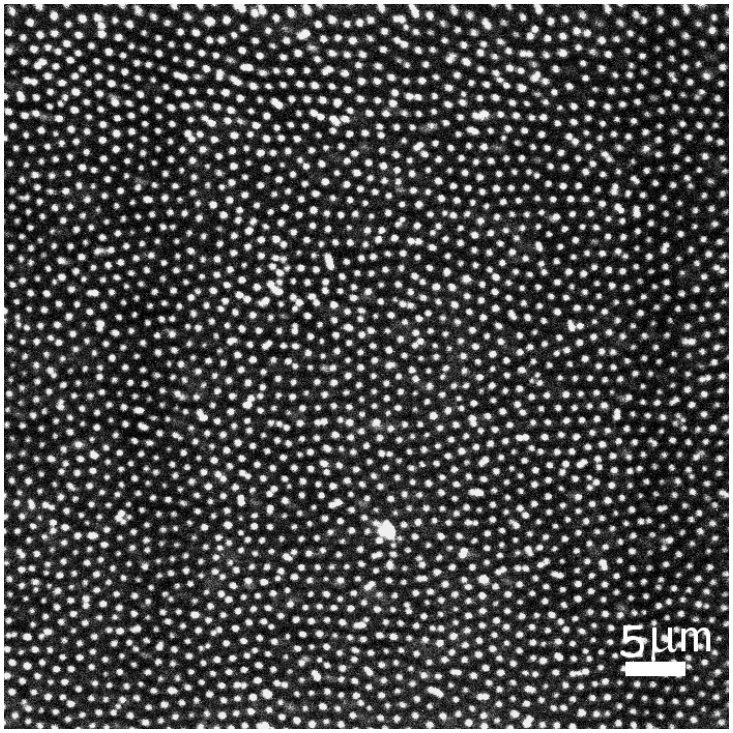

Figure 2.10: A frame from confocal image of core-shell silica particle: 1.14 μm NL6 silica colloids observed by confocal microscope (100× objective). The bright dots in the image are the fluorescent labeled cores. The particles are actually touching each other, but the cores are separated by the none-fluorescent labeled shells. Note that there are some cores touching each other forming doublets or triplets. They are just "impurities" formed *via* seeded growth on an two-particle or three-particle aggregates of seeds.

to convert this two-dimensional matrix of spacial intensity information (nor-

mally a tagged image file format, known as a "tiff" image) into information about colloidal particles such as positions of particles. This conversion procedure for our confocal microscopy images of colloidal dispersions was done using IDL, the Interactive Data Language. In this section, we will discuss the methods of particle tracking and particular IDL procedures for different purposes such as calculating pair correlation function, volume fraction of silica microspheres in colloids, and order parameters of double-particle bonds.

2.2.1 General Method for Particle Tracking

The general methods of tracking bright dots on a dark background, described in Crocker and Grier's article [35] and the website of Eric Weeks at Emory University [36], is suitable for our confocal images. This method normally contains three steps: first identify particles, then get data for all the particles you want, and finally link particles to form trajectories.

Identify Particles

IDL procedure "pretrack_thresholds.pro", based upon procedures available at Eric Weeks' website [36], with modifications written by Hugh Newman, was the particle identifying procedure we used. The purpose of this procedure is to determine the parameters we will use in particle tracking. The algorithm of this procedure is as follows (see IDL codes in appendix A):

- First, read the tiff stack image (a multi-frame tiff image) we have with readtiffstack.pro (a function to read in a tiff stack into a single variable, written by Eric Corwin), show one frame in the original image as a reference (see Figure 2.11 a).

- Then use "bpass.pro" [35], a spatial bandpass filter, to smooth the image and suppress the background noise, in order to make the image "Gaussian-like" white spots on a black background (see Figure 2.11 b).

- The function "feature.pro" then is used to analyze the filtered data and select the needed spherical features (particles) with the given parameters such as feature "diameter" (a little greater than apparent particle diameter in pixels, but smaller than separation, defined as "d" for short), "separation" (specifies the minimum allowable separation between feature centers, defined as "s"), "masscut" (minimum allowable brightness). The way "feature.pro" locates particles is as follows [35]:

  - First, identify the positions of all the local brightness maxima in the image, which are defined in a circular neighborhood with diameter equal to "d".

  - Around each of these maxima, place a circular mask of diameter "d", and calculate the x and y centroids, the total of all the pixel values (i.e. total brightness), the "radius of gyration" (simulates radius of gyration in the moment of inertia for an object with brightness instead of mass), and the "eccentricity" (0 for circles

and 1 for lines) of the pixel values within that mask.

  - The resulting x and y values will have errors of order 0.1 pixel for reasonably noise free images of features which are larger than about 5 pixels across. The error is smaller than 0.5 pixel (which corresponds to the location of a single pixel signal with 1 pixel resolution) because the location of the center of a spherical feature can get information from all pixels in this feature, which increases the accuracy location of the center than a single pixel signal.

  Feature.pro produces 5 columns of data from the image: (1) x-centroid (2) y-centroid (3) total brightness (4) radius of gyration and (5) "eccentricity". The plot of "radius of gyration" vs. "total brightness" in Figure 2.11 c help us to decide the brightness cutoff.

- Finally, we use "fover2d.pro" to compare our original image with the particles identified as wanted features. We can modify the parameters till we are satisfied that features found agrees with the particles we want (see Figure 2.11 d). This judgment, which depends on our particular needs while processing the images, could be made more objective using systematic methods with the help of analytical software (Igor Pro). We will discuss this in more detail in Chapter 3.

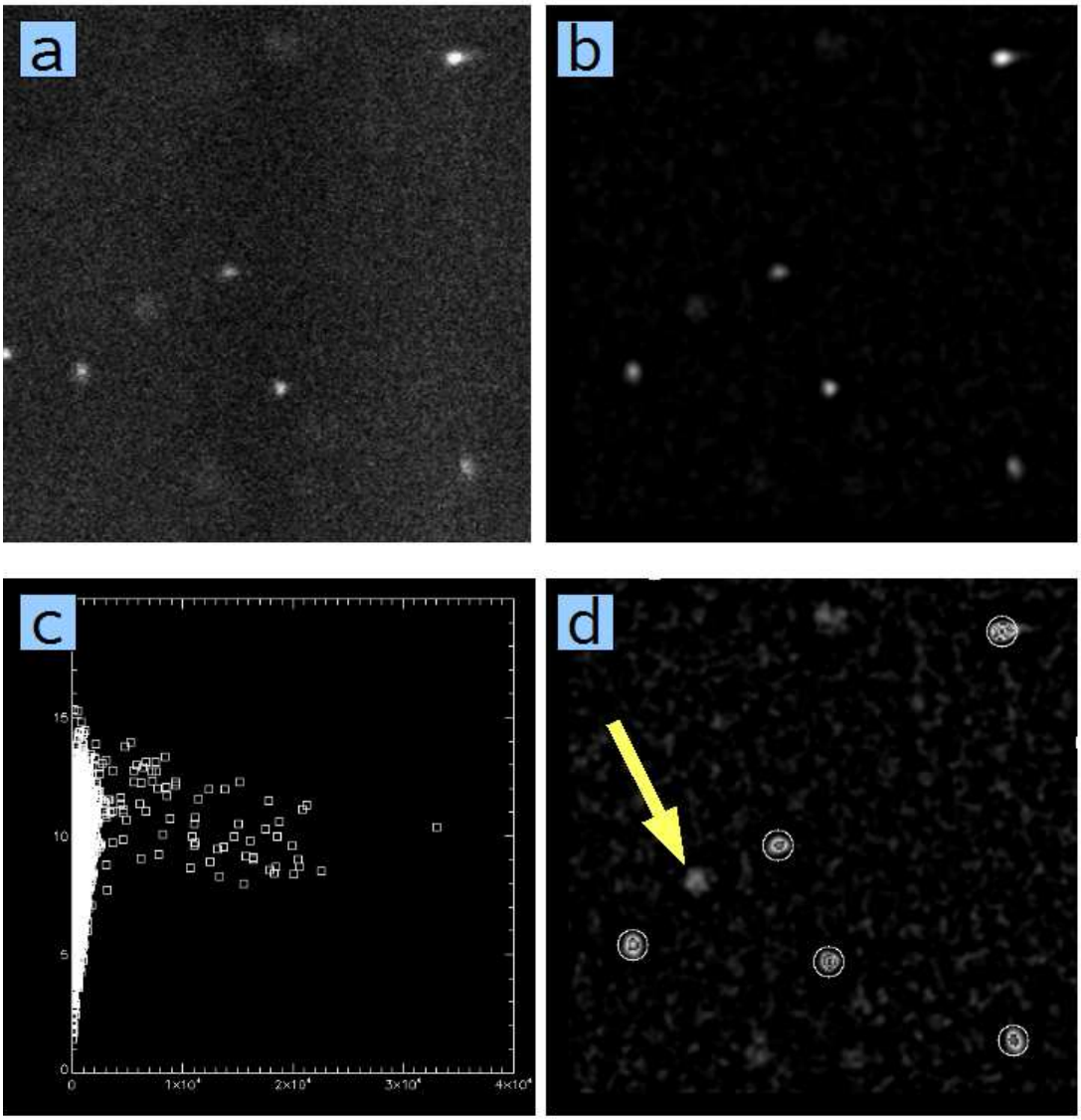

Figure 2.11: Identify Particles with IDL: (a) show one frame in the original image as a reference (only a part of the original frame is zoomed and shown in this picture); (b) use bpass.pro to smooth the image and suppress the background noise; (c) plot of "radius of gyration" (y axis) vs. "total brightness" (x axis); (d) use fover2d.pro to show (circle) the features we want. The dim spot (pointed by the arrow), corresponding to an out-of-focus particle, is not identified as a particle as its brightness is lower than the given value.

Two-dimensional Particle Tracking

After identifying particles from a test frame, we know the parameters to find particles in our image. We then apply these parameters to all the frames of our stack tiff image to get the data. The procedure used here is "hpretrack-.pro" (modified from Eric Weeks's procedure "epretrack.pro" by Hugh Newman with some obsolete options about Noran image format removed), which applies the parameters to the stack tiff image and produces a gdf file (a binary file format) containing 6 columns of data. The first 5 columns are the same as before, i.e. x and y position coordinates, brightness, etc. The 6th column contains the uniformly gridded time "t" that the position was determined (i.e. frame number). All data in the gdf file are sorted by the frame number so that the 6th column is monotonically increasing.

We can use the gdf file as the input of the procedure "track.pro" [35] to produce a 7-column data list. The additional 7th column is a unique "Particle ID number" series appended to the original 6-column input data structure for each identified particle trajectory. The result array is sorted so the rows with corresponding ID numbers are in contiguous blocks, with the time variable monotonically increasing inside each block. The parameters for "track.pro" includes "maxdisp" (an estimate of the maximum pixels distance that a particle would move in a single time interval), "memory" (the maximum number of time steps that a particle can be "lost" and then recovered again), and "goodenough" (to eliminate all trajectories with fewer than goodenough valid

positions. This is useful for eliminating very short, mostly "lost" trajectories due to blinking "noise" particles in the data stream.), etc.

Three-dimensional Particle Tracking

Particle identification and tracking in three dimensions (3D) is very similar to two dimensions (2D) [36]. There are differences in the tools used in the 3D procedures, for example, "bpass3d.pro" [35] is used instead of "bpass.pro", "feature3d.pro" [35] instead of "feature.pro" (instead of using one number for "diameter" in 2D, we use an array containing diameter in x, y and z directions as the "diameter" in 3D), "fover3d.pro" [35] [36] instead of "fover2d.pro", and "ept3d.pro" [36] instead of "hpretrack.pro". The 3D procedure "nl_3dpreview" (nl prefix refers to Ning Li, which means written by Ning Li) was used to identify particles in 3D image (z-stack confocal image), similar as "pretrack_thresholds.pro" in 2D. However, "nl_3dpreview" is able to measure the dimensions of particles in three dimensions. 3D tracking gives x, y, and z coordinates of all particles, which can be used to study the density distribution of silica particles in the colloidal system along z direction.

2.2.2 Structural Analysis of Colloidal System

Once we have obtained the positions of all colloidal particles in a reference 2D plane or a 3D volume, we can investigate structural information about the colloidal system. We created IDL procedures to calculate structural quantities of interest, such as the pair correlation function, the vertical particle

density profile, as well as two order parameters based on the bond density and bond angle. These IDL procedures contain two parts. The first part, discussed above, is the general method of getting the positions of all the particles we want. The second part then uses the particle positions to do our research. We will introduce the image calibration method and algorithms of these procedures in this subsection.

Image Calibration

Our calibration sample is a dip-coated, dried core-shell silica sample (NL9), which has a uniform layer of 0.77 μm (about 4% uncertainty, see Table 2.3) particles close packed. Because we can find large single domains in the dip-coated, dried sample, we can measure the center-to-center distance along a line of some 10 particles (thus reducing uncertainties by the same factor). We measured the diameter in pixels of the confocal image of this sample (8.96 pixels, 2% uncertainty) so that we know it is 11.64 pixels per micron (6% uncertainty) for a 700×700 confocal image (100× objective), corresponding to 0.086 micron per pixel.

Pair Correlation Function

The pair correlation function g(r) calculates the probability of finding the center of a particle a given distance from the center of another particle [36].

The 2D pair correlation function g(r) is defined as

$$g(r) = \frac{\rho(r)}{\rho_0} \tag{2.4}$$

where

$$\rho(r) = \frac{n(r)}{2\pi r \cdot \Delta r} \tag{2.5}$$

and

$$\rho_0 = \frac{N}{A} \ . \tag{2.6}$$

$n(r)$is the number of particles whose centers fall within the range of r to $r + \Delta r$; Δr is a small increase in r; N is the total particle number; A is the total area. The calculation of g(r) follows these steps:

- Consider each particle in the image in turn. In the 3D case the range is a spherical shell with thickness of Δr, and in 2D this is an annulus with width of Δr. We calculate the particle number density within this range and loop over all values of r with step size of Δr to get the density distribution along r. The 2D case is, for example, expressed in equation 2.5.

- Calculate the average particle number density of the whole sample, which is the total particle number N divided by the total volume (3D) or area (2D).

- Get g(r) by dividing the particle number density within r to $r + \Delta r$ by the average particle number density, to ensure that $g(r) = 1$ for structureless data (see equation 2.4).

The IDL procedure calculating 2D g(r) is "nl_ericgr2d.pro" (Ning Li), applying Eric Weeks's IDL routine "ericgr2d.pro" as part of this procedure. The algorithm of this procedure is as follows:

- Obtain 2D particle coordinates. Use the general method for 2D particle tracking (described in 2.2.1) to get the data for all particles from a time series of images at fixed z position.
- Apply Eric Weeks's IDL routine "ericgr2d.pro" to calculate g(r) of the particles.
  - Create 2 column matrices of identical dimensions M_0 and M_N, one (M_0) where each row containing x and y coordinates of one reference particle (x_0, y_0), the other (M_N) where each row contain x and y coordinates of all the particles (N particles, for example) in each frame of image. Subtracting M_N from M_0 gives all distances (of each particle in the frame) from the reference particle, as shown

in Equation 2.7.

$$\begin{pmatrix} x_0 & y_0 \\ x_0 & y_0 \\ . & . \\ . & . \\ . & . \\ x_0 & y_0 \end{pmatrix} - \begin{pmatrix} x_1 & y_1 \\ x_2 & y_2 \\ . & . \\ . & . \\ . & . \\ x_N & y_N \end{pmatrix} = \begin{pmatrix} x_0 - x_1 & y_0 - y_1 \\ x_0 - x_2 & y_0 - y_2 \\ . & . \\ . & . \\ . & . \\ x_0 - x_N & y_0 - y_N \end{pmatrix} \quad (2.7)$$

- Compute the density function of all distances from the reference point using "histogram" function. We decide upon the value of the bin size of r (Δr), which is the uniform grid length of r, based on a noise criterion. Δr is normally much less than the particle diameter.
- In order to get an accurate particle count using a sequence of circular annuli of increasing radius, within a rectangular image, we used a subroutine "checkquadrant", which can determine how much angular extent of the circle lies within the image when the circle of radius r extends outside of the image.
- Divide the array of "histogram" and the array of annulus area with radii of various r (monotonically increasing from minimum r to maximum r by the step size of Δr), we get the g(r) array for this reference particle.

- Run this procedure by treating each the particle in the frame as the reference in turn and loop over all frames, accumulate all the g(r) and finally normalize it by particle number, frame number, and average particle number density, we get the final g(r) result for this image.

- Print the result of "ericgr2d.pro", which contains the whole range r and corresponding g(r), into a data file readable by the graphical analysis program Igor Pro.

Silica Colloids Vertical Density Distribution

The procedure "nl_3dhisto.pro" calculates the vertical profile of particle number density, hence we can get the vertical volume fraction distribution as a reference parameter while doing electric field experiments.

The confocal image used for this procedure is a z-stack series (tiff file), which is an image series taken at continuously shifting z (vertical) positions step by step through the whole thickness of colloidal particles. The z step number is the frame number of the z-stack series image. Along with the tiff image stack, there is a "csv" file (text file) recording the actual z position of each z step (i.e. each frame). The algorithm of this procedure is as follows:

- Obtain 3D particle coordinates using the general method for 3D particle tracking. As the z step number in a 3D image is simply the frame

number, the z positions of particle centers then is expressed by a number between the minimum and maximum frame number (for example, 0 to 99 for a 100 frame z-stack image).

- Obtain vertical density profile. Histogram the z positions of particle centers to compute the particle number density distribution along z. We wish to obtain local volume fraction as a function of z. In order to do this, the reference volume should have thickness comparable to the particle diameter. Therefore, the number of frames contained in each bin of the "histogram" (defined as "binsize") times the actual shifted depth in each frame (defined as "stepsize"), which is the real bin width in microns, should be slightly larger than the particle diameter (expressed in Equation 2.8).

$$binsize \times stepsize \geq diameter \tag{2.8}$$

  That is, the "slice" has full x and y extent, and is thick enough to include one layer of particles. We histogram the full range of z where particles are found.

- To calculate the volume fraction, multiply the volume of one particle with the particle number in each bin, and divide by the actual volume of that bin slice. The actual z position is from the "csv" file. The actual x and y value is from the difference of the maximum and minimum x and y data out of the whole image (which is very close to the full x

and y dimension of the image due to the densely packed particles in the bottom frame of the image), and multiplied by 0.086 micron per pixel, obtained from calibration.

- Print output data. The output data is printed to a "dat" file, containing one column of the z position and another column of the corresponding number density distribution.

- Moving average. Sometimes the stepsize is much smaller than particle diameter, hence the binsize is big due to Equation 2.8. If we still need to move in z by small steps in order to take more volume fraction data (the reason for this is explained in the next chapter), we can simply add another histogram of z which is shifted by a small number of frames ("snf" for short, this number should be smaller than the binsize of the first one), but still using the same binsize and the same maximum of z. Then we get another set of histogram whose z position is shifted by "snf". By rearranging the z position in the output data, we have a list of volume fraction with more details in terms of z position. For example, if we set "snf" to be half of the binsize, we will then get a series of volume fraction in the step of half bin, but with each bin width still thick enough for the particle size.

For example, a z-stack confocal image of naturally sedimented 0.77 μm silica particles (NL9) gives a x-z profile of the 3D cube (see Figure 2.12a), which

is produced using the routine "yslice.pro" [36] in procedure "nl_3dpreview", with x:z ratio of 2:1 for a more spherical appearance of particles. The procedure "nl_3dhisto.pro" will give the particle number density distribution along the z direction (see Figure 2.12b). The structure of this profile is explained in more detail in next chapter.

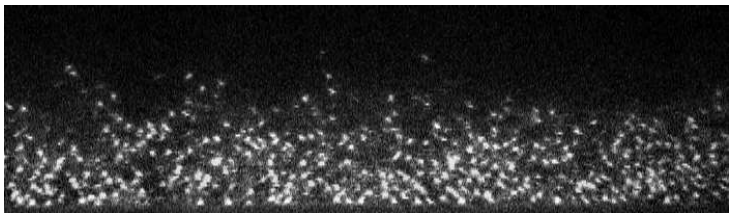

(a) A x-z view of naturally sedimented silica particles in water/DMSO mixture.

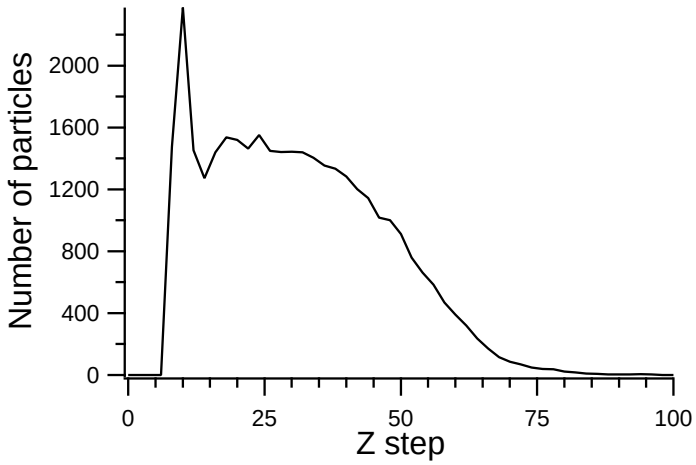

(b) Particle number density distribution along Z. Y axis of the plot is number of particle centers. X axis of the plot is z steps starting from the bottom of sediment.

Figure 2.12: Example of the particle number density distribution from a three-dimensional image stack.

Particle Bond Density Calculation

We define a "bond" to exist in our image when two particles are close enough that the distance of the centers of them is shorter than the bond length we set. Note that this bond is not a real chemical bond but simply a criterion for describing proximity between two particles. The bond density, by our definition, is the ratio of the number of bonded particles to the total particle number. The procedure "nl_bondensity" calculates the bond density of a time series confocal image of our core-shell silica spheres under an external electric field, to see how the field affects the bond density. The algorithm of this procedure is as follows:

- Obtain 2D particle coordinates.
- Count number of particles in each frame. In each frame of the image, we take the x and y coordinates of particle centers, and calculate number of particles in the frame (represented by N). Then make a one-column array (for the next step) with the number of rows same as the particle number in the frame.
- As the x y coordinates consist of two columns of data with the row number equal to the number of particles found in the frame, we can get all the possible distances (D) between each particle in the frame by subtracting from the original coordinates a set of coordinates which are shifted in rows by the amount of 1 to the maximum particle number in this frame. Comparing the distances with the bond length (L), we

know which particles in the frame are bonded. Force the same places where particles are bonded in the array we created in last step to be "1", and therefore the sum of all elements in this array is simply the number of "bonded particles" (N_b) in this frame. Divide this number by the total particle number in this frame (N), we will get the bond density in this frame ($\rho_b(Z)$). We summarize the calculation in one frame in these equations:

$$N_b = \sum_{\text{all particles}} Count(D < L) \tag{2.9}$$

$$\rho_b(Z) = \frac{N_b}{N} \tag{2.10}$$

where *Count* means the number of cases satisfying D < L.

- Loop over all frames in the time series and we get the average bond density for the whole image. If N_f is the number of frames in the image stack, we can express the final bond density ρ_b as:

$$\rho_b = \frac{\sum_{Z=1}^{N_f} \rho_b(Z)}{N_f} \tag{2.11}$$

Average Particle Bond Direction

We also want to investigate how the external electric field affects the direction of the bonds. The procedure "nl_bondtheta", whose purpose is to calculate $\langle \cos^2 \theta \rangle$ and $\langle \sin^2 \theta \rangle$, where θ is the angle between the line joining the centers

of two bonded particles and the external field direction along y axis, follows this algorithm:

- Obtain 2D particle coordinates.
- In each frame of the image, we take the x y coordinates of particle centers, and calculate number of particles in the frame.
- Similar to the procedure for bond density ("nl_bondensity"), we calculate all the possible distances (D) between each particle in the frame by shifting the coordinates in rows. Here the distances in separated x and y direction (X and Y) are recorded as well as the total distances between the bonded pair particles. It is actually the square of the distances that are calculated in the procedure. To calculate $\cos^2\theta$ and $\sin^2\theta$ we can simply divide the y and x distances by the total distances.
- Loop over all particles in each frame and all frame of the image, we get final $\langle\cos^2\theta\rangle$ and $\langle\sin^2\theta\rangle$. We summarize the calculation for the complete image stack in these equations:

$$\langle\cos^2\theta\rangle = \sum_{\text{bonded particles}} \frac{Y^2/D^2}{N_b \times N_f} \tag{2.12}$$

$$\langle\sin^2\theta\rangle = \sum_{\text{bonded particles}} \frac{X^2/D^2}{N_b \times N_f} \tag{2.13}$$

where N_f is the number of frames in the image stack.

2.3 Electric Field Simulation and Construction

The external electric field sample cells used for our colloidal systems was designed and constructed in cooperation with Mr. Joseph Fitzgerald and Dr. Amit Agarwal. First, we used a simulation package "Poisson Superfish" (Los Alamos National Laboratory) to visualize and quantify the electric field created between thin gold-film-electrodes coated on glass microscope slides and cover slips. The purpose of the simulation was to analyze the feasibility of using thin gold-film-electrodes on glass substrates to create a uniform linear/rotating electric field in the plane of colloidal sample between glass slides. Then, we used the results of the simulation to design appropriate geometries for uniform linear and rotating fields. Finally, we constructed electric field cells as shown in Figure 2.13.

2.3.1 Simulation of Electric Field

Simulation of Linear Field

We simulated the linear field between two pairs of thin gold-film-electrodes on glass substrates, with solvent of various dielectric constants filling in between. Figure 2.14 shows the center part of the side-view sketch of linear field electrodes coated on glass substrates: parts A are glass substrates (upper A is a cover slip, 0.17 mm thick, and bottom A is a microscope slide, 1

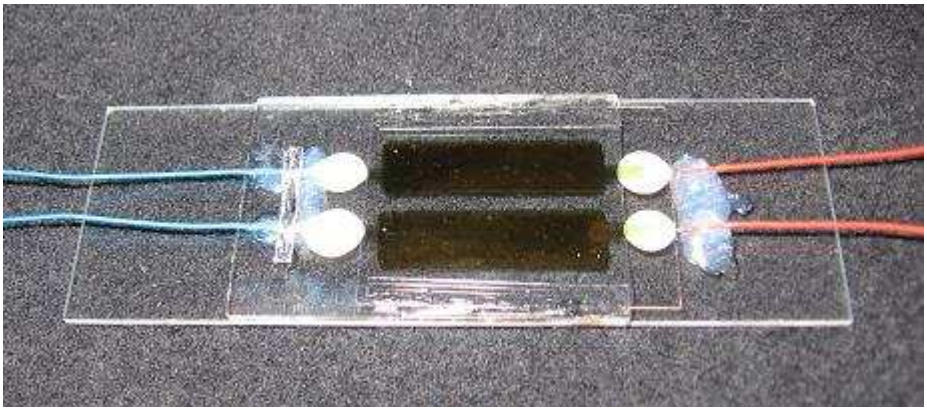

(a) Completed two-electrode linear field cell.

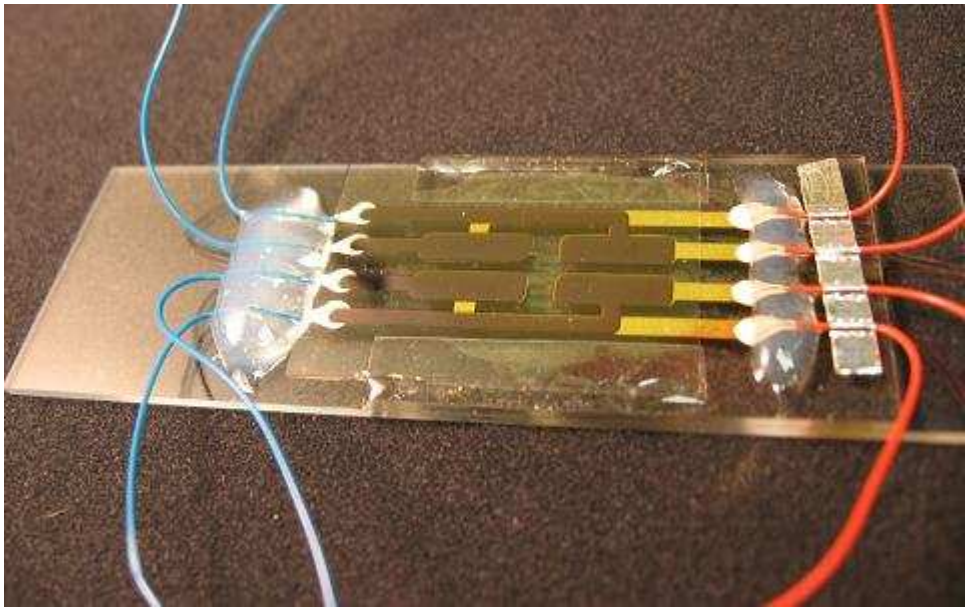

(b) Completed four-electrode rotating field cell.

Figure 2.13: Completed electric field cells. The silver colored strips are aluminum foil tapes used in cell making. See 2.3.2 for details.

mm thick); parts B are the colloidal sample we want to study, which should be one continuous part but was most simply put into the program as three piecewise sections; the geometric center of the part B in the middle is designed to be at the center of the graph, i.e. x=0, y=0; and the two pairs of white bars above and under the two parts B on the left and right side represent the thin gold-film-electrodes coated on glass substrates, 0.025 mm thick. The other unmarked parts are vacuum. The geometry of the whole electric field was first designed, an electric potential was then applied on the thin gold-film-electrodes in the simulation (for example, the left pair was given a potential of 200 V and the right pair was given -200 V), and the electric field and potential in this geometry were calculated automatically (only for the points from the intersections of the tiny triangular grid of lines in the background, known as "mesh" in Poisson Superfish, which should be small enough, 0.025 mm in our case, for Poisson Superfish to calculate the potential and field correctly). Different materials were represented in the simulation by different dielectric constants in the editable input file: 4 for glass, 80 for water, etc.

Figure 2.15 shows the calculated electric potential and field directions of linear field geometry. The small arrows show the direction of local electric field, and the pine lines are equal potential lines. When moving the mouse cursor on this graph, local position, electric field and potential are automatically shown by the software.

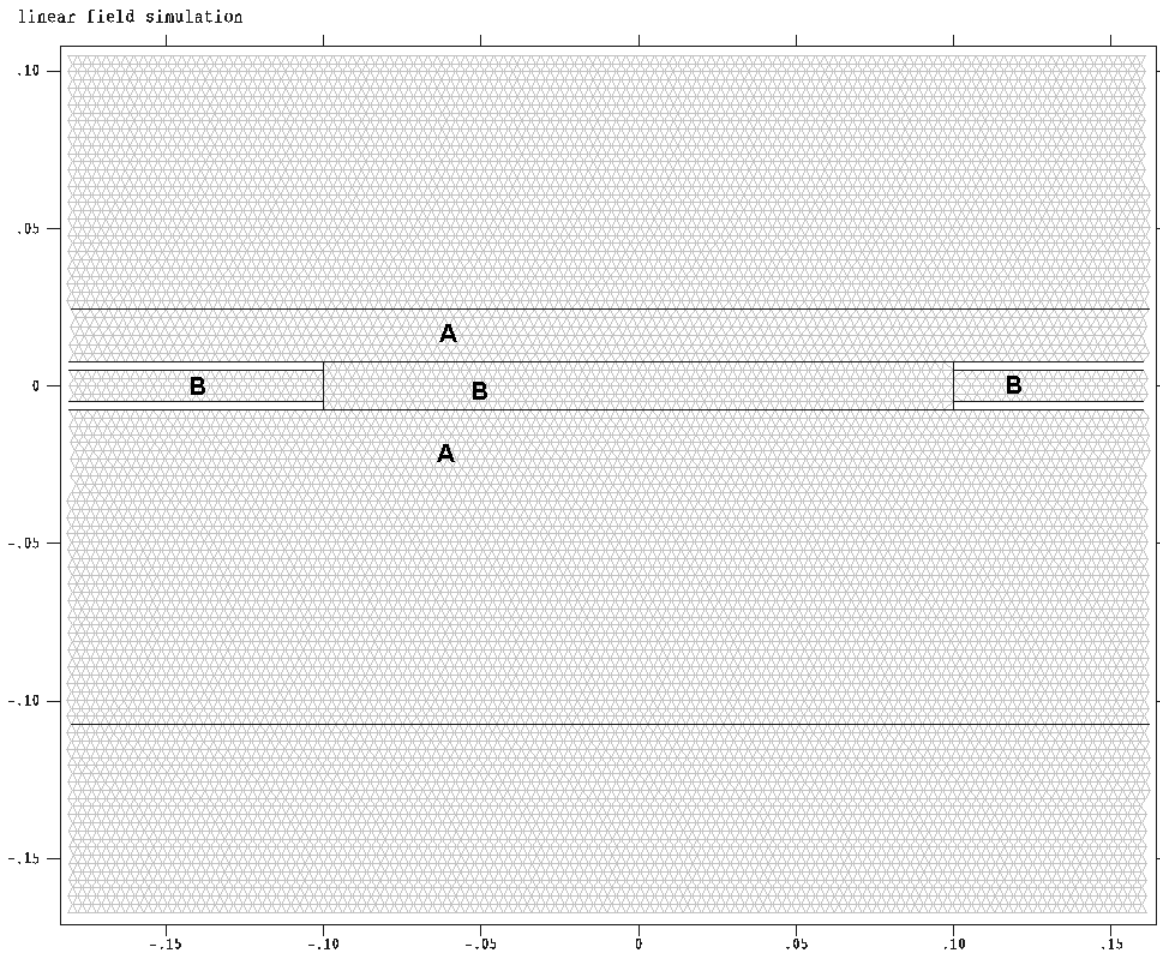

Figure 2.14: Side-view sketch of linear field electrodes: parts A are glass substrates (upper A is a cover slip, 0.17 mm thick, and bottom A is a microscope slide, 1 mm thick); parts B are the colloidal sample we want to study, which should be one continuous part but actually separated into three while using the software; and the two pairs of white bars above and under the two parts B on left and right side are the thin gold-film-electrodes coated on glass substrates, 0.025 mm thick. The other empty parts are vacuum. Different materials were represented in the simulation by different dielectric constants in the editable input file: 4 for glass, 80 for water, etc.

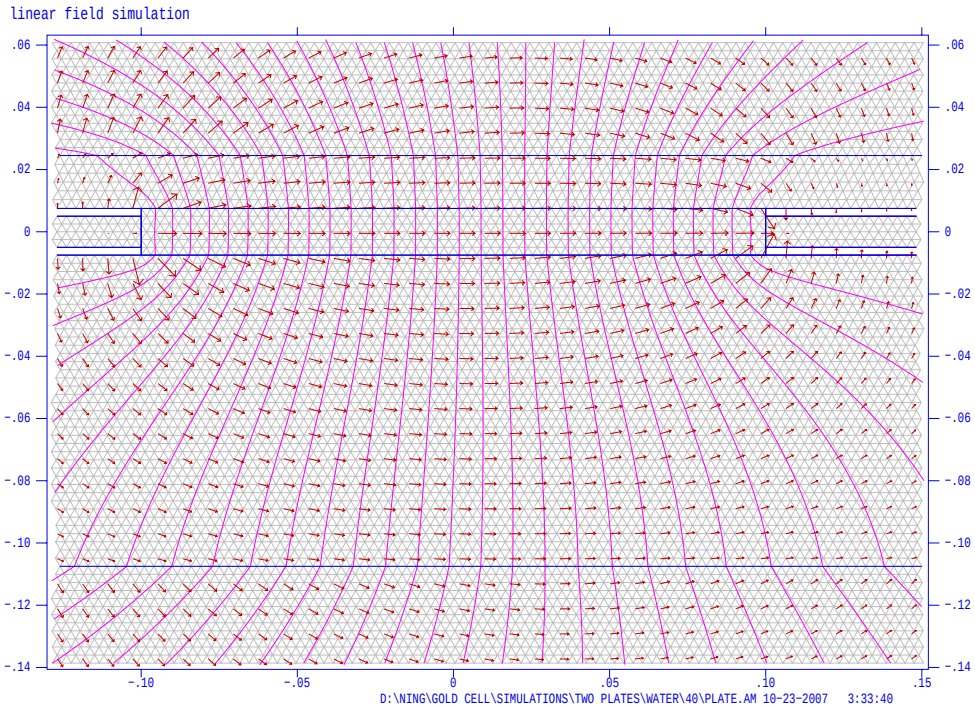

Figure 2.15: Simulation result of linear field geometry (zoomed in at the geometrical center): the small arrows show the direction of local electric field, and the pine lines are equal potential lines. The y axis of the graph corresponds to vertical direction in real space, and the x axis corresponds to horizontal direction, the numbers are in centimeters. The white bars represent gold films applied with same potential for each pair (200 V for left pair and -200 V for right pair); therefore, no electric field lines exist between each pair of white bars.

To determine a range of the system in which the field is sufficiently uniform to conduct our physical observations, we developed a quantifying criterion. We defined the following method for extracting the range in the side-view sketch:

- Move the mouse cursor to the central point (0,0) and record the electric field magnitude $|E_0|$. Calculate (50/1172)*$|E_0|$ (approximately 4% of this value, picked as our desired field uniformity), call this value ΔE. Record $E_x(0)$ (the x component of the electric field at (0,0)).

- Traverse the positive x (horizontal) axis and observe the point at which $|E_x(0) - E_x| = \Delta E$, where E_x is the x component of the electric field at some point on the x axis. Record the x position of this point.

- Repeat the previous step, but instead traverse the negative x axis. Record this x position.

The positions recorded from the positive and negative sides were symmetric, provided that the external field is linear. Therefore, we used a single value for the width as $\pm\Delta x$ ($\Delta x \approx 0.3mm$). It was also observed that the non-uniformity in the y component of the electric field was much smaller than that in the x component. In fact, E_y remained acceptably uniform everywhere between the glass regions along the lines of acceptable E_x. This indicated that as far as we observe on the center line between the two pairs of electrodes (which are at the left and right side in Figure 2.14), the electric field should be sufficiently uniform. Figure 2.16 shows an example image of an acceptable range. $\pm\Delta x$ is represented by the horizontal red bar. Δy is considered to span the entire range between glass slides, as shown by the vertical red bar. Shaded gray area represents the entire region of acceptable uniformity (x and y components vary less than 4.27% in this region). Black axes and gray box

are superimposed for clarity (the area is approximately 600 nm × 300 nm).

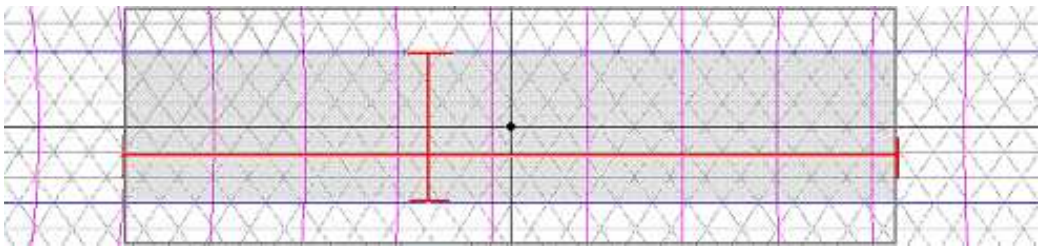

Figure 2.16: Example image of an acceptable range in side-view linear field simulation: $\pm\Delta x$ is represented by the horizontal red bar. Δy is considered to span the entire range between glass slides, as shown by the vertical red bar. Shaded gray area represents the entire region of acceptable uniformity (x and y components vary less than 4.27% in this region). Black axes and gray box are superimposed for clarity.

The acceptable range along each pair of electrodes, which is the direction perpendicular to the paper plane in Figure 2.14, was almost the whole length of the electrode along that direction. This indicates that along the central line between two pairs of electrodes, there is a large range we can use for observation.

Simulation of Rotating Field

It was also necessary to develop a criterion for the acceptable range in the top-view geometry for rotating field. Figure 2.17 shows the top-view of the center of the rotating field electrode structure. In this figure, the white parts "1A", "1B", "2A", "2B" represent four pairs of thin gold-film-electrodes. The two electrode up and down in each pair (we cannot see them both because this is

the top view) were given the same electric potential in the simulation, similar as the linear field. The rest of the figure represents the colloidal sample we want to observe. A rotating field can be obtained like this: connect 1A and 1B to positive and negative output of a sine wave AC power supply "channel 1"; similarly connect 2A and 2B to positive and negative output of another sine wave AC power supply "channel 2"; channel 1 and channel 2 have the same frequency, but 90° phase difference. Hence there will be a electric field with constant strength and rotating direction produced in the center of the four electrode pair (which is also made to be the geometric center (0,0) in simulation). A similar technique was used to determine the acceptable range of field uniformity. We defined the following method for extracting the range from top-view geometries:

- Move the mouse cursor to the central point (0,0) and record the electric field magnitude $|E_0|$. Calculate (50/1172)*$|E_0|$ (approximately 4% of this value), call this value ΔE. Record $E_x(0)$ and $E_y(0)$ (the x and y component of E_0).

- Traverse the positive and negative x (horizontal) axes and observe the two points at which $|E_x(0) - E_x(x)| = \Delta E$, where $E_x(x)$ is the x component of the electric field at some point on the x axis. Record the x positions of these two points, for example, Δx_x = -0.53 mm, 0.44 mm. Note these values are generally not symmetric.

- Traverse the positive and negative y (vertical) axes and observe the two

points where $|E_x(0) - E_x(y)| = \Delta E$, $E_x(y)$ is the x component of the electric field at some point on the y axis. Record the y position of these points, for example, Δy_x = -0.44 mm, 0.54 mm. (It was observed that the y component of electric field E_y was always satisfying the criteria within Δy_x, i.e. $\Delta y_y > \Delta y_x$.)

- These four values define a rectangle (the big blue rectangle in Figure 2.17). Traverse the top and bottom edges of this rectangle, and record the x positions of the four points where $|E_y(0) - E_y(x)| = \Delta E$, $E_y(x)$ is the y component of the electric field along the top and bottom edges of this rectangle. In our simulations, these four points were symmetric about y axis, so we recorded our data in the form $\pm\Delta x_y = 0.26$ mm.

- The acceptable range is now considered to be the smaller rectangular region (gray shaded region in Figure 2.17) in which both the Δy_x, and Δx_y criteria are satisfied. Observation in this region has the uniformity of electric field guaranteed.

2.3.2 Design and Construction of Electric Field Cells

Design of Linear Field

Using the electric-field simulation package Poisson Superfish, we demonstrated the feasibility of creating a uniform linear/rotating electric field with thin gold-film-electrodes coated on glass substrates. Then we designed two

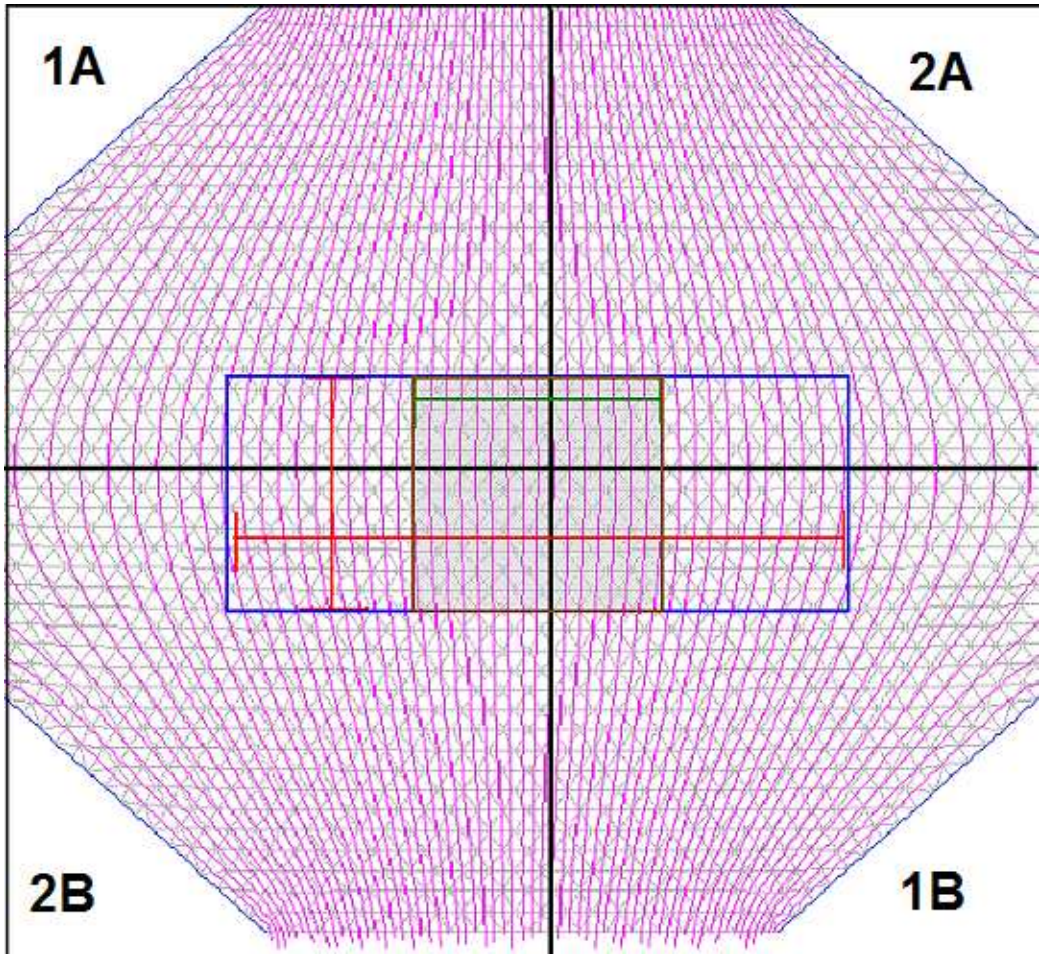

Figure 2.17: Example image of an acceptable range in top-view rotating field simulation: Δx_x, and Δy_x are represented by the horizontal and vertical red bars. The blue rectangle surrounds the area in which E_x varies less than 4.27%. Δx_y is shown by the horizontal green bar. The overall acceptable range lies in the overlap and is indicated by the gray shaded region.

types of masks for gold coating in order to make the gold-film-electrodes on microscope slides and cover slips. The cells used for electric field studies on colloids were made by two pieces of glass substrates coated with exactly the same structure of electrodes, having each pair of electrodes facing each other and the potential difference between different pairs of electrode creating the horizontal linear/rotating field.

The masks were made of brass (thanks to Mr. Whalen), with a size same as number 1 micro cover slips, i.e. 30×22 mm. The designing sketch of the brass mask for linear field is shown in Figure 2.18: The black parts are the empty area on the mask where gold can be coated through, and the white area is brass where gold vapor is blocked during gold coating. Each electrode (the black part) is formed by a main rectangular electrode and a short "wire" on which we can make contact. The dimension of each rectangular electrode, as shown in the figure, is 22×6 mm. They are 2 mm apart from each other, 4 mm from the top and bottom boundary of the mask, 2 mm from the right boundary, and 6 mm from the left boundary. The short "wire" connected to each electrode is 1 mm wide and 5 mm long. The end of each line then is 1 mm from the left boundary of the mask. The photo of the actual linear field mask is shown in Figure 2.19. Note that all the right angles were rounded for technical reasons (the smallest milling machine bit available was approximately 1 mm in diameter).

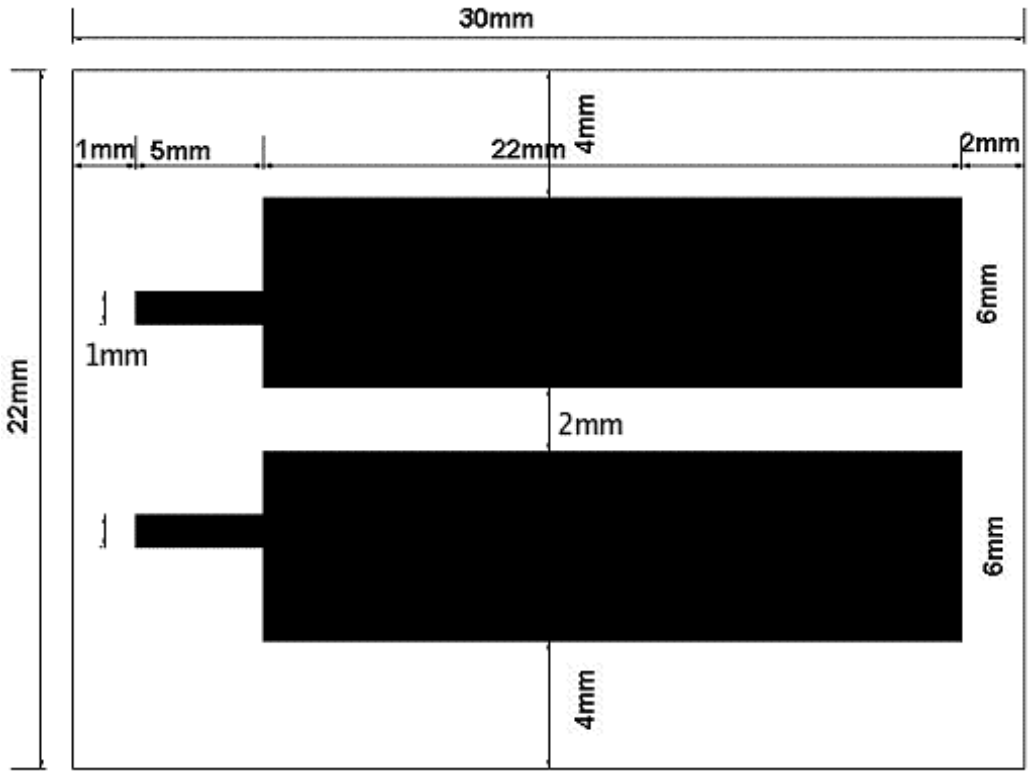

Figure 2.18: The design of the linear field mask: Each electrode (the black part) is formed by a main rectangular electrode and a short "wire" on which we can make conduction. The dimension of each rectangular electrode, as shown in the figure, is 22×6 mm. They are 2 mm apart from each other, 4 mm from the top and bottom boundary of the mask, 2 mm from the right boundary, and 6 mm from the left boundary. The short "wire" connected to each electrode is 1 mm wide and 5 mm long. The end of each line then is 1 mm from the left boundary of the mask.

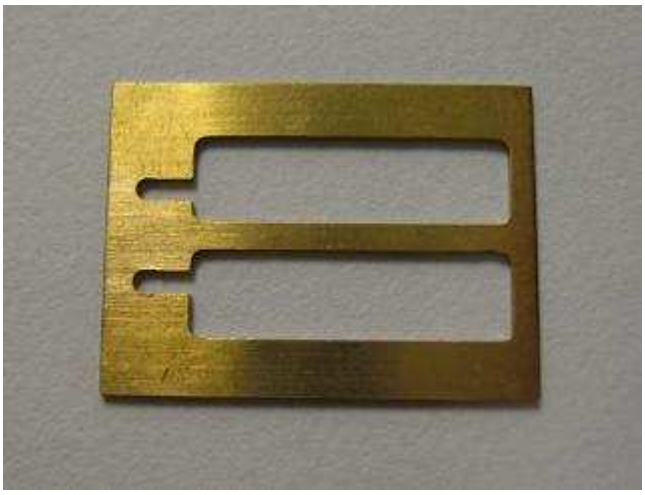

Figure 2.19: Brass mask for linear field.

Design of Rotating Field

Similar as the linear field mask, the rotating field mask was also made of brass and had boundary dimensions of 30×22 mm. The sketch of rotating field mask is shown in Figure 2.20: Same as the linear field mask, the black parts are the actual structure of gold-film-electrodes, and the other white area is brass where gold vapor is blocked during gold coating. The four electrodes (9×3 mm) are all rectangular flattened at the near-center angle by a small 0.5×0.5 mm right angle triangular, in order to agree with the electrode structure in former simulation (see Figure 2.17). But actually the near-center angles were rounded due to technical reason, instead of flattened (see Figure 2.21). The four electrodes were designed to be separated from each other by 2 mm, but actually they were made to be separated by 2 mm horizontally and 1 mm vertically in brass masks (due to technical reason).

The electrodes are 2 mm from the right boundary of the mask, and 8 mm from the left boundary. They were designed to be 7 mm from the top and the bottom boundary of the mask, but were actually 7.5 mm as the vertical distance between electrodes was shrunk by 1 mm. The "wires" on the electrodes were designed to avoid overlapping of conduction joints with real wires when making the cell. The "wires" are 1 mm wide and 2 mm away from the left boundary of the mask. The photo of actual rotating field mask is shown in Figure 2.21. Again all sharp corners were rounded.

Construction of Electric Field

The construction of linear and rotating electric field microscope sample cells followed these steps:

- Use the brass masks for linear and rotating field for gold coating on micro glass slides and cover slips.
  - Cut each microscope slide (VWR, 75×25 mm, 1.0 mm thick, plain) into two identical pieces (37.5×25 mm). Prepare 8 pieces of them and 8 micro cover slips (VWR, 30×22 mm, 0.17 mm thick) as we have 8 linear field masks and 8 rotating field masks.
  - Ultrasonicate these glass slides in soap water for approximately 30 minutes. Then clean them with tap water and distilled water. Once there is a thin non-dewetting water layer on the glass slides, they should be clean enough. The washed slides are then naturally

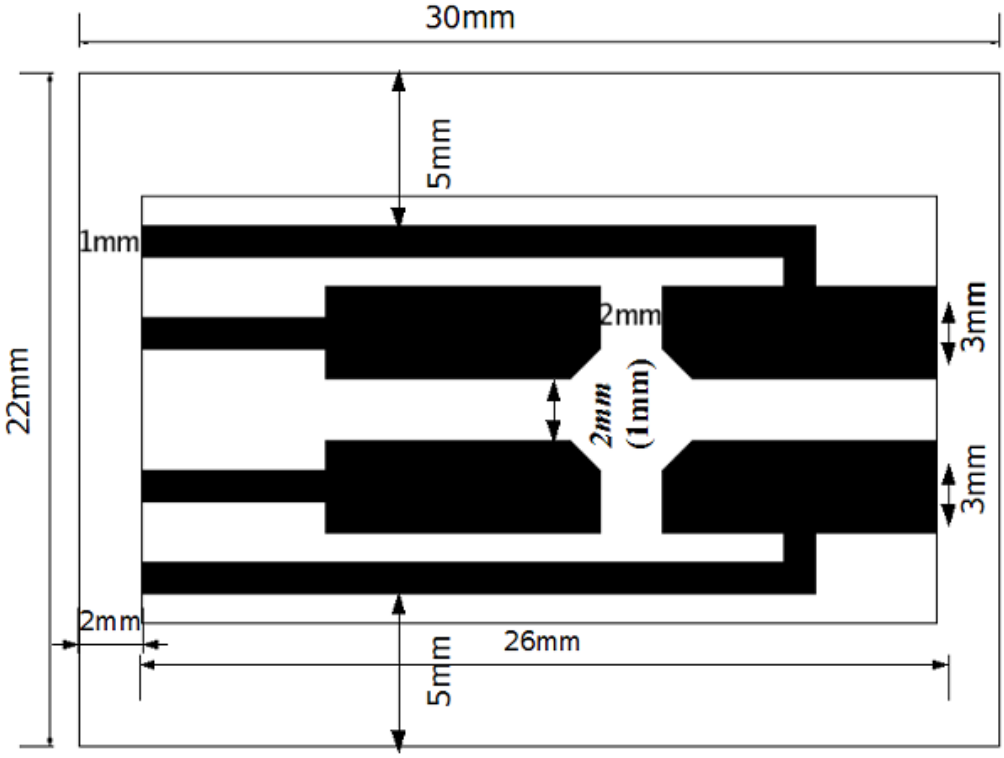

Figure 2.20: The designing sketch of the rotating field mask: The four electrodes (9×3 mm) are all rectangular flattened at the near-center angle by a small $0.5 times 0.5$ mm right angle triangular. The four electrodes were designed to be separated from each other by 2 mm, but actually they were made to be separated by 2 mm horizontally and 1 mm vertically in brass masks. The electrodes are 2 mm from the right boundary of the mask, and 8 mm from the left boundary. They were designed to be 7 mm from the top and the bottom boundary of the mask, but actually 7.5 mm as the vertical distance between electrodes was shrink by 1 mm. The "wires" are 1 mm wide and 2 mm away from the left boundary of the mask.

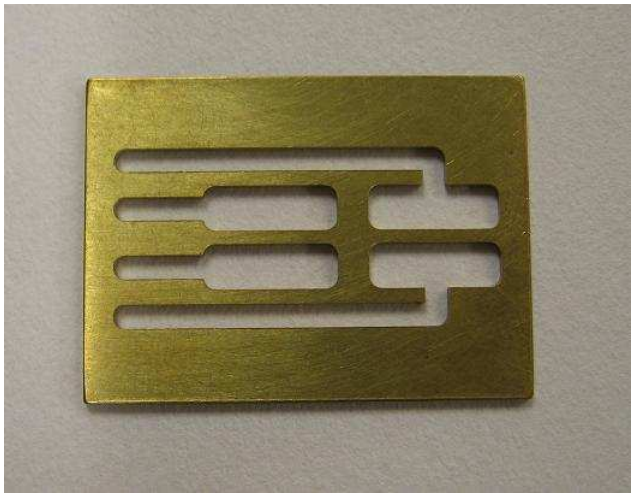

Figure 2.21: Brass mask for rotating field.

dried at room temperature (25 ℃).

– Use the masks for gold coating on the cleaned microscope slides and cover slips. The "Edwards" coating units we used for gold coating were mainly consisted of a high vacuum system (including a vacuum pump, a glass bell jar chamber and necessary valves and gauges) and a tungsten basket heater inside the chamber. Basically, we were creating a huge light bulb, putting a small piece of gold wire (99.99%) on the tungsten light bulb filament, and heating it to the point where the gold actually evaporated, and then condensed on our relatively cold sample surface (masked). This process happened in the chamber where a high vacuum environment was required (10^{-4} torr or less). The gold-film-electrodes coated on glass are shown in Figures 2.22 and 2.23.

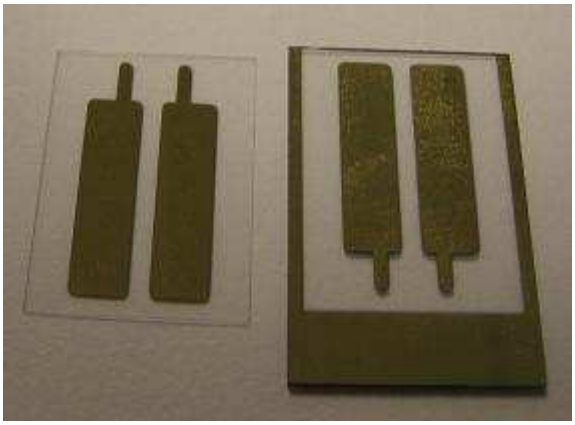

Figure 2.22: The gold-film-electrodes coated on glass slides for two-electrode linear field cell.

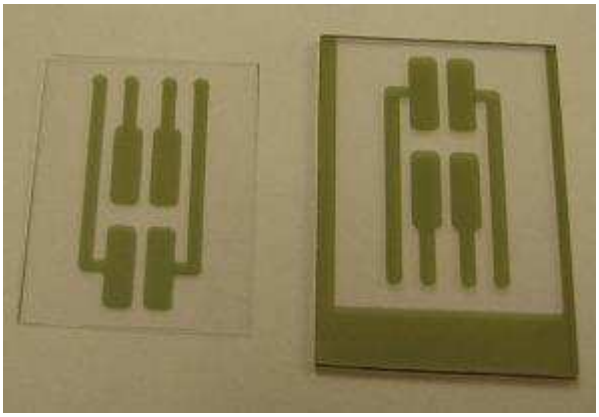

Figure 2.23: The gold-film-electrodes coated on glass slides for four-electrode rotating field cell.

- We also used chromium-gold coating, i.e. chromium (99.998% pure, Kurt J. Lesker) coated first on glass and then gold coated on chromium, for a better electrode adherence to glass.

- Make contacts with thin electric wires (AWG, mm) on the gold coated glass slides.

  - Clean the extra gold on the glass slides in case of any unwanted shorting when turning voltage on. The gold does not stick to glass well, so it is very easy to clean the extra gold with wipes (Kimwipes). On the other hand, we need to be extremely careful not to scratch the gold electrode by any chance. The chromium-gold coated electrodes stick strongly to glass and are difficult to scratch. However we need to use 20% hydrochloric acid to clean the extra gold on these slides.

  - Cut a piece of electric wire (approximately 20 cm) for each electrode. Use wire stripper to strip the insulation from electric wires at both ends, 2 mm for one end and 1 cm for the other.

  - Each cell is made of one thin cover slip and one thick slide, with the same type of gold coating facing each other and "wires" left at opposite sides. So we put one gold coated cover slip and another same-type-coated micro glass slide on a aluminum board (for the later heating). Carefully put the stripped 2 mm end of each wire on each gold "wire" of the gold electrode. Use a a small piece of

aluminum foil tape to stick the insulation part of the wires, for the cover slip, onto the aluminum board. The aluminum foil tape can endure a high temperature when we cure the conductive glue. Similarly use this tape to stick the wires onto the microscope slide as there is more extra space on the slide than the slip (see the aluminum foil tape stripes in Figure 2.13, for example). We stick the wires with the aluminum foil tape in order to hold them close to the gold electrode "wires", which helps keep the wires in close contact with the gold substrate (important to minimize the joint resistance).

– Put a small drop of conductive glue (Norland conductive adhesive 130) with a bamboo stick on each of the joints of the 2 mm stripped section of the electric wire and the gold electrode "wire". Put the aluminum plate (with one cover slip, one slide and the wires on it) into a pre-heated oven (approximately 140 ℃). The glue will be precured in 5 minutes. Take out the aluminum plate to check if the wires come off or moved, and add a little more conductive glue if necessary. Be careful not to put too much conductive glue that shorts the nearby electrode. The cure of the conductive glue takes 1 hour or even more, depends on the temperature. Once the wires and gold electrodes are checked to be conducting (using a multimeter), we can turn the oven off.

- Use the microscope slide and cover slip with electric wires to make an electric field cell.
  - We use 0.075 mm thick polyethylene terephthalate film (Goodfellow) as the spacer between the two pieces of micro glass. Cut two spacers (25×3 mm) from the film, wash them with 95% alcohol, and wipe them with wipers.
  - Put the spacers on sides of the glass slide where no gold were coated on. Then put the cover slip on the slide with gold electrodes facing inside. Carefully align the electrode pattern of the bottom slide and the top cover slip. Put a weight or bamboo stick to press the cover slip on the bottom slide which are separated by the 0.075 mm spacer.
  - Use bamboo stick to put little drops of No. 61 UV (ultraviolet) glue (Norland optical adhesive 61) on side of the spacers. The glue will go in slowly and join the top cover slip and the bottom slide due to the capillary effect. Put this cell under a high-intensity UV lamp (Spectroline, 365 nm wavelength) within a short distance (approximately 10 cm) for faster cure. The precure for No. 61 uv glue needs a few seconds, and the complete cure needs approximately 15 minutes.
  - For a more convenient mounting of the cell on the confocal microscope, join another full length plain micro glass slide (simply

washed with alcohol) at the bottom of the half-size glass slide (using the same No. 61 UV epoxy).

- In order to strengthen the wires of the cell, use a much thicker UV glue (Norland UV sealant 91) to joint the wires of the top cover slip onto the bottom slide. Examples of completed linear and rotating field cell are shown in Figure 2.24 and 2.25.
- There is a large vertical electric field produced at the overlap of the "wire" part of the four-electrode cell when turning on a rotating field (the circled parts pointed by arrows in Figure 2.26). This problem can be avoided by redesigning the rotating field mask in the future. Therefore we use wider spacers (25×6 mm) so that the extended spacers can separate the overlapped "wires". This is the reason for chromium-gold coating, which gives durable electrodes that cannot be scratched by the extended spacers.

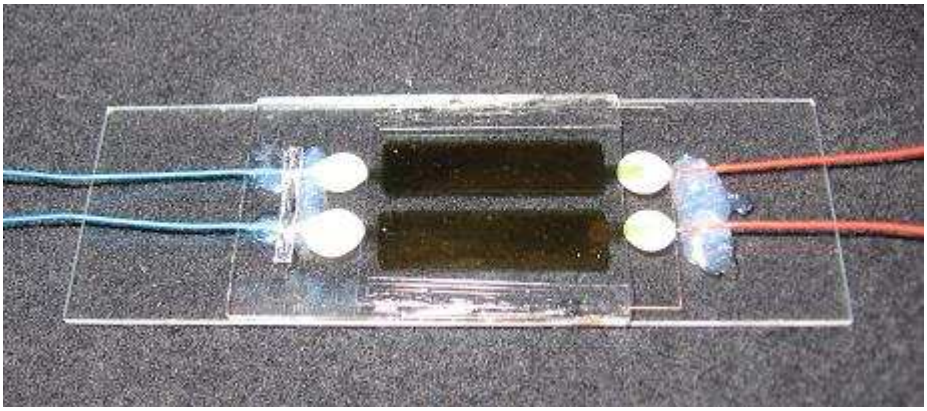

Figure 2.24: Completed two-electrode linear field cell.

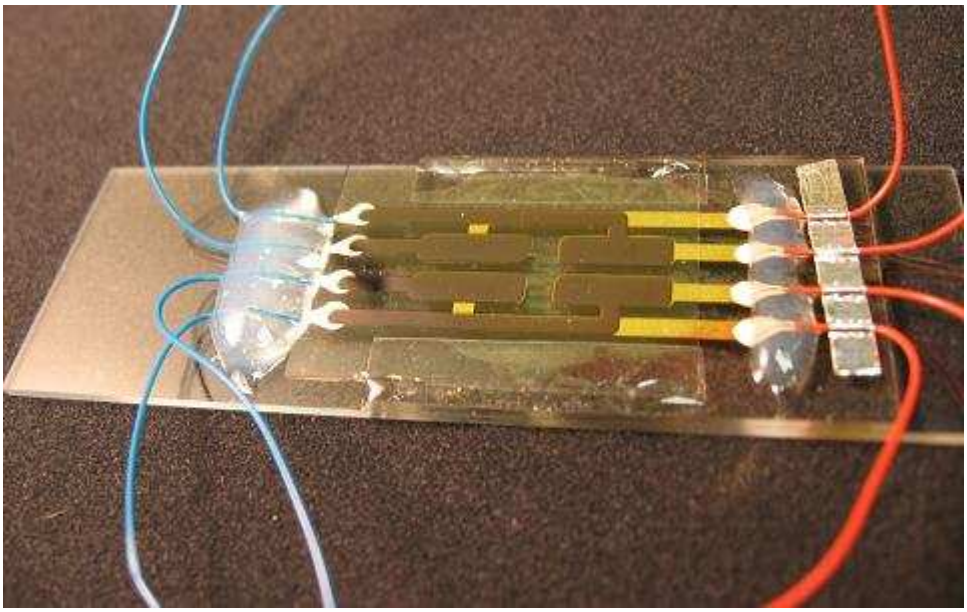

Figure 2.25: Completed four-electrode rotating field cell.

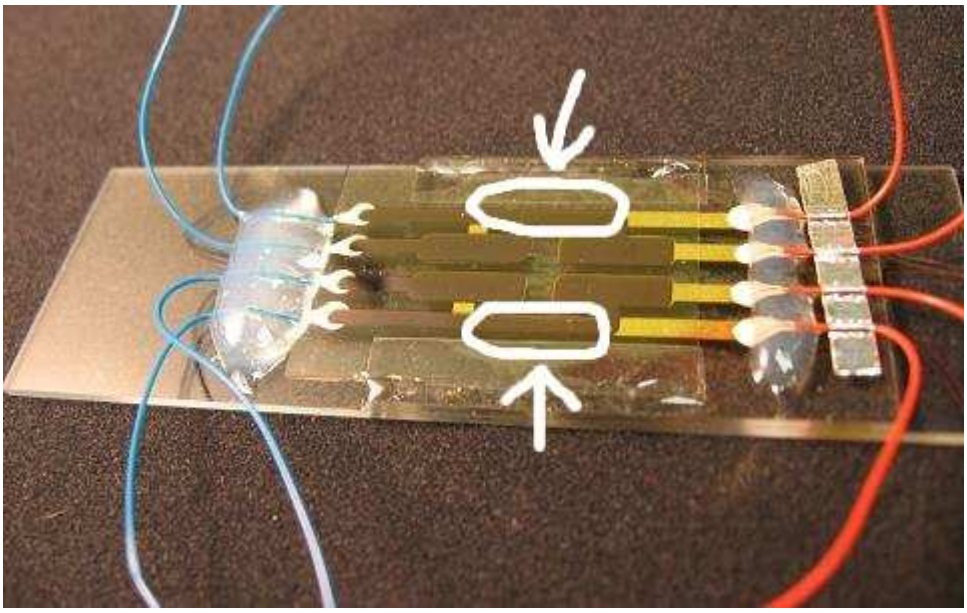

Figure 2.26: Highlighted area at the overlap of the "wire" part of the four-electrode cell where large vertical electric field were produced as a side effect of rotating field

Chapter 3

Experiments, Data Analysis and Results

This chapter describes the detailed procedure for our electric field experiments in sedimented colloidal suspensions, the acquisition and analysis of quantitative data, and finally the discussion of results.

3.1 Experimental Procedures

This section describes general procedures for electric field experiments. Using the confocal microscope, we studied the synthesized silica colloids under external electric fields. The confocal images were then analyzed using image-processing programs written in the IDL programming language, the raw data was analyzed to calculate different order parameters, and the output order parameters were further analyzed using graphical analyzing program Igor Pro.

3.1.1 Sample Preparation

We used synthesized silica core-shell particles (0.77μm NL9 and 1.14μm NL8, see 2.1 for synthesis details) to prepare samples for confocal microscopy (see 2.3.2 for more details about the cell). The colloids were refractive index matched for confocal imaging, and salt added to make the silica spheres behave like hard spheres. The colloids were then filled in the cells made for electric field experiments.

Refractive Index Matching

The less the mismatch between the refractive index of silica particles n_p and of the surrounding fluid n_f, the better the confocal image quality of fluorescent cores will be. This is because multiple scattering of light degrades image quality. We did not know the exact n_p of our porous silica particles, but we

knew $n_p \approx 1.46$. Therefore we used dimethyl sulfoxide (abbreviated DMSO, ACP Chemicals Inc., $n_D = 1.479$, 20 ℃) and distilled water ($n_W = 1.333$, 20 ℃) mixture to make a fluid whose n_f equals n_p. A mixture of water:DMSO with volume fraction ratio of 15:85 gave a relatively good result. Thus we found that $n_p \approx 1.46$. The original silica suspension stored in ethanol was very milky and almost opaque. After transfer to the water:DMSO mixture, where the same centrifuge technique was used as before, the suspension contained in a 2 mL cylindrical glass vial was clear enough to easily look through.

To minimize the refractive index mismatch, we used the technique of heating or cooling the suspensions to decide whether more DMSO or water was needed. Because the refractive index of water:DMSO mixture decreases while the mixture is heated and increases when cooled (the temperature dependence of refractive index for typical solvent is approximately 0.001 per Kelvin), we can tell whether n_f in the suspension is higher or lower than n_p and adjust it as follows:

- If the suspension (in a glass container) looks clearer when cooled with cold tap water, or it looks more milky when heated with hot tap water, then n_f at room temperature is actually lower than n_p. We can add a few drops of DMSO in the suspension to make it look clearer.

- If the suspension looks clearer when heated, or it looks more milky when cooled, then n_f at room temperature is actually higher than n_p.

We can add a few drops of distilled water in the suspension to make it look clearer.

- If both heating and cooling make the suspension look worse, n_f equal n_p and the refractive index mismatch is minimized. The suspension should appear very clear and transparent.

Control of Ionic Strength

To make the colloidal silica spheres behave like hard spheres, we needed to decrease the Debye screening length down to one tenth of the particle diameter, which was approximately 50 nm for 0.5 - 1 μm. The Debye screening length κ^{-1} is related to the electrolyte ionic strength and dielectric constant, as well as the absolute temperature, by [37]:

$$\kappa^2 = e^2 \ \frac{2C_0 N_A}{\varepsilon_0 \varepsilon_r k_B T} \tag{3.1}$$

where κ is inversed Debye screening length, e is the elementary charge, C_0 is the ionic strength of the electrolyte and is in mol/m^3 as κ is in SI units, N_A is Avogadro's number, ε_0 is the permittivity of free space, ε_r is the dielectric constant, k_B is the Boltzmann's constant, and T is the absolute temperature in kelvin. A more commonly used formula to calculate κ^{-1} is:

$$\kappa^{-1} = 0.034\sqrt{\frac{\varepsilon_r}{C_0}} \ (nm) \tag{3.2}$$

which can be easily derived from Equation 3.1, and C_0 here is in mol/L. From Equation 3.2, we can get the relation between κ^{-1} and C_0. Using:

$$C_0 = \frac{\sigma}{\Lambda_0(\eta_w/\eta_{wd})} \tag{3.3}$$

which describes the relation of C_0 and specific conductivity σ of an electrolytic solution, we can tell if the ionic strength of the suspension is strong enough to have a small enough κ^{-1} by measuring the conductivity using a conductivity meter (Amber Science Inc). Λ_0 here is the molar conductivity of electrolytes, which is 141.3 S cm^2 mol^{-1} at 0.01 mol dm^{-3} [37]. η_w and η_{wd} are viscosities of water (1.002 cP at 20 ℃) and water:DMSO mixture (1.847 cP at 20 ℃ for 15:85 volume ratio). Due to Walden's rule [37], the product of molar conductivity and viscosity of one electrolyte should be constant.

We made 1.94 g/L KCl water solution, and added to water:DMSO mixture for making hard sphere like colloidal suspensions. For $\kappa^{-1} = 50$ nm , the calculated result of needed C_0 was 2.45×10^{-5} M, corresponded to a σ of 1.87 μS/cm. After adding 394 μL KCl solution to 225 mL water:DMSO mixture, we got a σ of actually 1.96 μS/cm, corresponding to a C_0 of 2.57×10^{-5} M, and the actual $\kappa^{-1} = 48.8$ nm.

Control of Sample Concentration and Sample Filling

The volume fraction of our colloidal samples was measured using the same oven-drying method as described in last chapter, assuming the density of porous silica sphere was 2 g/mL. Volume fractions for the samples we used were as follows:

- 3.1% 0.77 μm core-shell silica colloids (NL9B1), salted (i.e. KCl added), used for Experiment S1 (described in next section).
- 3.8% 1.14 μm core-shell silica colloids (NL8B), salted, used for Experiment L1.
- 3.1% 0.77 μm core-shell silica colloids (NL9B2), unsalted (i.e. water and DMSO only), used for Experiment S2.

After making the samples, we stored each of them separately in 2 mL black cap glass vials. Before experiments, we stirred the sample using a vortexer (Vortex Genie 2, Scientific Industries) and ultrasonicated it for approximately 30 minutes to make the volume fraction uniform. Then a disposable Pasteur pipette ($5\frac{3}{4}$ inches, Fisherbrand) was used to take the sample, by dipping the tip of the pipette in the sample. The capillary action drove the sample into the pipette, although only a small amount. The sample was then transferred to the electric field cell we made by touching the pipette tip to the edge of the cell, again due to the capillary action. This was repeated a few times

until the cell was fully filled. We tried to avoid creating any air bubbles while filling the cell, which otherwise can affect the uniformity of the electric field.

3.1.2 Experimental Setup

Here we introduce the experimental setup, including setup for electric field instruments and configurations for our confocal microscope.

Electric Field Setup

The instruments we used to generate electric fields were a dual-channel function generator (0-25 MHz, Tektronix, AFG3022) and two wide-band amplifiers (DC/0-1 MHz, Krohn-Hite, 7602M), and a two-channel digital storage oscilloscope (0-10 MHz, Tektronix, TDS1002) for monitoring AC voltages.

For the two-electrode linear field cell (described in 2.3.2), only one channel of the function generator and one amplifier was used. One pair of vertically overlapped electrodes was connected to the positive output *via* wires, the other pair was grounded. We used the function generator to generate a 1 MHz, sinusoidally alternating signal, and used the amplifier to generate different amplitudes of potentials. The signal amplitude from the function generator was 1 V (peak-to-peak potential, same for follows). Both the amplitudes generated from generator and the amplifier can be gradually varied to change the output. The amplitude control in the generator was especially useful as the amplitude control in the amplifier gave too large fluctuation in

output. The amplifier can be easily turned on and off to achieve fast switching between field on and field off in the sample.

For the four-electrode linear/rotating cell, both channels of the generator (Channel 1 and Channel 2) were used, and both amplifiers were used respectively for the two channels. Again each pair of vertically overlapped electrodes were connected to one output. Four pairs of electrodes corresponded to four outputs from the two amplifiers, as shown in Figure 3.1: if

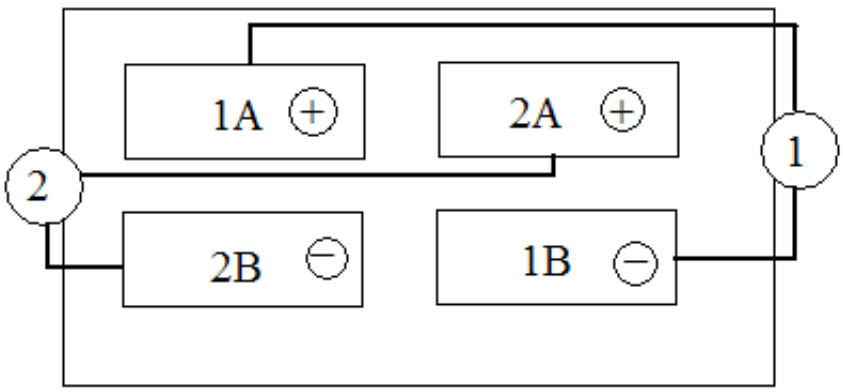

Figure 3.1: Sketch for four-electrode cell electric set up: the top left (1A) and bottom right (1B) pairs were respectively connected to positive and negative output of one amplifier (Amplifier 1) which amplified Channel 1; the top right (2A) and bottom left (2B) pairs were respectively connected to positive and negative output of the other amplifier (Amplifier 2) which amplified Channel 2.

viewed from the top of the cell, the top left (1A) and bottom right (1B) pairs were respectively connected to positive and negative output of one amplifier

(Amplifier 1) which amplified Channel 1; the top right (2A) and bottom left (2B) pairs were respectively connected to positive and negative output of the other amplifier (Amplifier 2) which amplified Channel 2. Note that Channel 1/2 and Amplifier 1/2 were arbitrarily chosen, and should not affect the result if 1 and 2 were completely switched. We used negative output instead of ground in order to achieve symmetric rotating field. The detector of the oscilloscope, however, can only measure the potential to ground because one of the two connections on the detector was designed to be grounded through the oscilloscope. Therefore we had to use the other connection of the detector connecting only the positive output of the amplifier, knowing the actual potential was twice as high as shown on the oscilloscope. We again used 1 MHz sinusoidally alternating signal, but for rotating field there was a 90° phase shift from channel 2 to channel 1, while for linear field there was no phase difference between the two channels. The amplitudes of potentials from the two amplifiers were always kept the same for either rotating field or linear field, in order to have a spatially uniform field near the center of the four electrodes.

Microscope Configuration

The confocal microscope we used consists of a Nikon fluorescent inverted microscope, a VisiTech confocal scanning unit equipped with a 491 nm laser. The configurations in the confocal microscope and the confocal controlling software "VoxCell" were as follows:

- 100×/1.40 Oil objective
- 50 μm aperture
- 700 × 700 pixels
- 29 frames per second (fps) scan speed
- 8 bit data (for output images)
- 1× amplification

To optimize the quality of the confocal images, one needs to adjust laser power and photomultiplier tubes (PMT) gain using the VoxCell software for the 491 nm laser we used.

3.1.3 Experiment Procedure

The operational procedure of the three electric field experiments is described here, including linear field experiment for NL9B1 0.77 μm silica particles (Experiment S1, as it is the first experiment using relatively small size silica colloids) and NL8B 1.14 μm particles (Experiment L1, as it is the first experiment using relatively large size silica colloids), and rotating/linear field experiment for NL9B2 0.77 μm particles (Experiment S2, as it is the second experiment using relatively small size silica colloids).

Experiment S1

This experiment, using 0.77 μm diameter silica colloids (NL9B1, salted, $\kappa a = 7.9$ where a is particle radius) under linear fields created by a two-electrode cell (2 mm between the two electrodes, see 2.3.2), was completed in a procedure as follows:

- Sedimentation profile.
  - A confocal z-scan was carried out for the full range of sedimented silica particles. Analyze the data with IDL procedure nl_3dhisto-.pro and obtain a profile of particle number distribution along sedimenting direction, i.e. z direction.
  - Load the IDL data to Igor Pro, calculate the volume fraction (ϕ) distribution along z steps (Z, integers start from 0). The step-size along z of the confocal image acquisition (stored in the variable "*stepsize*") was chosen to be roughly half of the particle diameter (i.e. 0.4 μm). Data from a number (stored in the variable "*binsize*") of consecutive steps were binned together. Typically, the variable *binsize* and *stepsize* were chosen such that *binsize* $\times$ *stepsize* $\approx$ *particle diameter* (see Figure 3.2). In order to calculate local volume fraction in one bin we can simply multiply the particle numbers found by a constant (C_ϕ):

$$C_\phi = \frac{V_p}{V_{bin}} \tag{3.4}$$

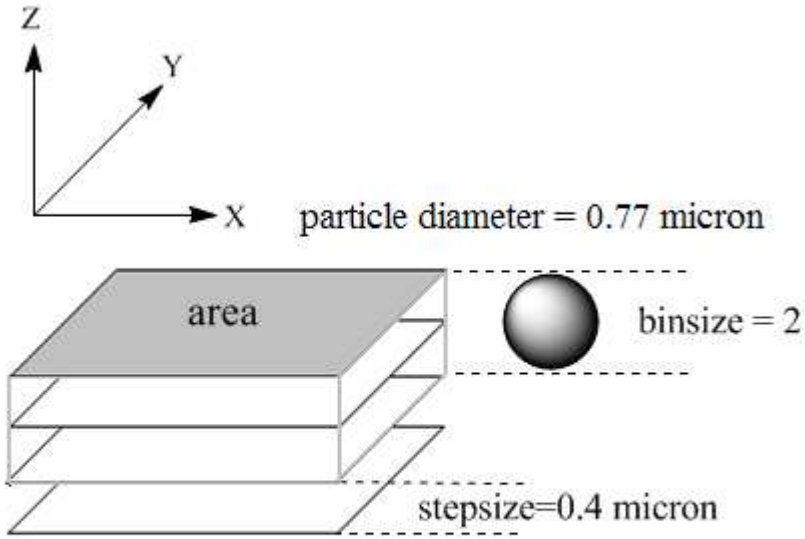

Figure 3.2: Z steps and bin of histogram: Uniformly distributed four steps in z direction showed as a model for z-scan. The stepsize showed in the figure is 0.4 μm; if our particle diameter is 0.77 μm, then we choose a binsize of 2. The volume of one bin (highlighted by gray lines) then can be calculated from binsize, stepsize, and the dimensions in x and y.

where V_p is the single particle volume, and V_{bin} is the bin volume:

$$V_{bin} = binsize \times stepsize \times area \tag{3.5}$$

For example, the stepsize showed in the figure is 0.4 μm; if our particle diameter is 0.77 μm, then we choose a binsize of 2. The volume of one bin (highlighted by gray lines in the figure) then can be calculated from binsize, stepsize, and the dimensions in x and y (700 pixels $\approx$ 60 μm for both x and y in our case). Therefore, V_{bin} in the figure equals 2880 $(\mu\text{m})^3$, and the corresponding C_ϕ equals 8.3×10^{-5}.

- Using Igor, we can also easily get the real z position from the IDL result. We used 100 steps for z-scan, correspond to 0 to 42.3 μm. So each z step number (Z) multiplying stepsize 0.423 μm gives z position (Z_p).
- From the analysis in Igor, locate the Z range containing 10 points for needed volume fraction, see Figure 3.3. As we were interested in low ϕ case, the range we selected for this experiment was approximately from 10% to 0.2%.

- Time Series at different depth. With the 10 points of Z_p, we know where in depth to take confocal time series image for bond parameter and other analysis. Start from the deepest position point among the ten, take 400-frame time series (29 fps), and move up to the next position

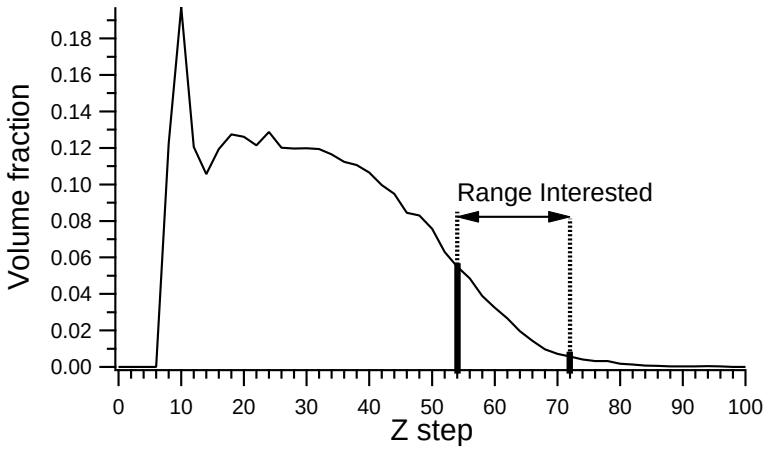

Figure 3.3: Example of sedimentation profile. The "Range Interested" in the figure shows the general Z range of interest for confocal time series experiments.

to take another 400-frame time series.

- Vary fields. We started from no field, and repeated the whole procedure at different values of linear field. We took 11 values between 0 V and 300 V, and the values were almost equally distributed (in volt): 0, 50, 100, 120, 150, 180, 200, 220, 250, 280, 300. Note the corresponding fields here were just these potentials divided by 2 mm.

- Analyze these time series using IDL procedures nl_bondensity.pro, nl_bondtheta.pro and nl_ericgr2d.pro, etc to get bond order parameters and pair correlation functions.

- Load all these data to Igor Pro for analysis.

Experiment L1

This experiment, using 1.14 μm diameter salted silica colloids (NL8B, $\kappa a =$ 11.7 where a is particle radius) under linear fields created by a two-electrode cell (2 mm between), was completed in a procedure similar to Experiment S1.

We used the moving average method for z profile as mentioned in 2.2.2, due to the relatively large particle diameter. We did 100 z steps through 30 μm, therefore the stepsize is 0.3 μm and binsize is 4, leading to a 1.2 μm thick bin slide. However, we shifted every 2 frames (i.e. 0.6 μm) in z-stack to get more finely-spaced data.

We took 11 equally (every 20 V) separated values from 0 to 200 V as the potentials across the 2 mm electrode gap, corresponding to 11 fields from 0 to 1000 V/cm.

Experiment S2

This experiment, using 0.77 μm unsalted silica colloids (NL9B2) under linear/rotating fields created by a four-electrode cell (see 2.3.2 for details), was again completed in a similar procedure.

The reason we used unsalted colloids for this experiments is that the vertical field created at the overlaps of the electrode "wires", as we mentioned in 2.3.2. When a rotating field was applied on the four-electrode cell, a poten-

tial difference between the top and bottom electrodes created a high vertical electric field at the overlap parts of the "wires". Sample with higher ionic strength would produce more heat, dangerous for the 100× objective which was closely touching the cell. Therefore, we switched to a unsalted 0.77 μm sample with same concentration.

We took 11 values from 0 V to 240 V, for both linear and rotating fields. From the simulation results we had an estimate for the actual fields at the center of the four electrodes where we observed the colloids through the microscope. These fields were not the same for the linear field and rotating field, and different from the two-electrode case. This was simply due to different electrode geometries. For example, a 200 V potential corresponded to a 1000 V/cm linear field in the two-electrode cell. But for four-electrode cell, the linear field produced by 200 V was 820 V/cm, and the rotating field produced by the same potential was 580 V/cm ($1/\sqrt{2}$ of linear field).

When doing the experiment, we switched between linear and rotating field (i.e. switched the phase difference between Channel 1 and Channel 2 between 0°and 90°) at all the ten places in depth and also at all 11 potential values, in order to obtain the sedimentation profile and time series images for these two types of field. To assure the colloids were at equilibrium state, the switching of the field type was not faster than once per minute. The advantage of this method was having the linear/rotating phase transition observed at the same

place in the plane. Even if there was any vertical shift (there actually was a little as we will show later), we would not lose any information in local volume fraction, since we had the sedimentation profile separately taken for each type of field.

3.2 Data Acquisition, Analysis and Results

In this section, we will present the detailed methods of data acquisition and analysis, as mentioned in 3.1.3 at the last step of the experiment procedure.

3.2.1 Data Acquisition

From all the confocal images taken in each experiment, we used IDL to calculate bond parameters. We also used Igor Pro to help determine the proper parameters of IDL procedures described in 2.2.

Data Naming Convention

In one experiment, for each value of potential we had ten time series with different local volume fractions. Normally a 400-frame time series was exported with a name containing information of both potential and volume fraction. Since the sedimented silica colloids showed a decreasing local volume fraction upon decreasing depth and we started from the lowest point, normally the first time series was the most dense one. For example, the first time series taken at 20 V, which had the highest local volume fraction, would be named

as “020v_ts1”; and the last one with the lowest volume fraction would be “020v_ts10”.

Systematic Method For Setting Brightness Thresholds

Identifying features *via* image processing is an imperfect science, with a delicate balance between cutoffs which allow no spurious particles and cutoffs that do not miss any real particles. When acquiring z-stacks, it is possible by correlating particles in adjacent frames to obtain a very reliable measure of particle. When obtaining time series, the results were more sensitive to the value of the brightness parameter (i.e. the brightness threshold) used. We devised (and describe here) a self-consistent procedure to treat all time series images in the same way.

The brightness threshold turned out to be an important parameter in the IDL procedures (i.e. “nl_bondensity.pro”, “nl_bondtheta.pro” and “nl_ericgr2d-.pro”) for calculating the colloidal order parameter, because the number of identified particles within an image was sensitive to the brightness used. Too low a brightness threshold allows the identification of noise as spurious particles. Increasing the brightness threshold progressively decreased the number of real particles that are found. To minimize the instability and subjectivity of human judgment, we plotted the calculated bond densities of the time series image at maximum volume fraction (ts1) as a function of the brightness threshold used. An example from Experiment S1 was shown in Figure 3.4.

At very high values of the brightness threshold, the bond density saturates

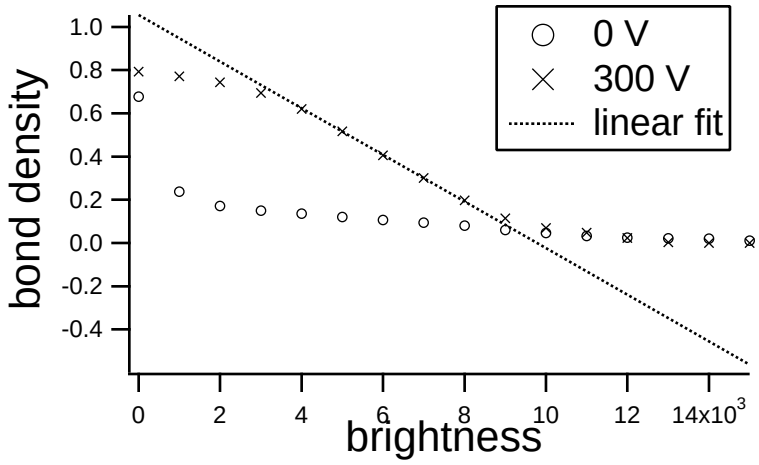

Figure 3.4: Bond density vs brightness from Experiment S1 (0.77 μm): If we curve fit the linear part of 300 V data, the point where the original data and the linear curve fit start to meet, i.e. 4000 in brightness axis, is a good value of brightness cutoff for our image.

at a value close to zero. On lowering brightness threshold (below 9000 in Figure 3.4), there is a linear increase in bond density. At very low brightness (below 4000), artifacts are allowed and there is again nonlinear behavior. When we curve fit the linear part of 300 V data, the point where the original data and the linear curve fit start to meet, i.e. 4000 in brightness axis, was seen to give a good value of brightness cutoff for the corresponding confocal time-series image. We used this brightness threshold for the ts1 images at the highest potentials, and got the statistics of features found (average number of identified particles in each frame) for different volume fractions. The maximum ϕ for different potentials were normally different, and only these data for maximum ϕ showed a obvious nonlinearity. An example for Experiment

S1 is shown in Figure 3.5. Features found (N_f) in image were proportional

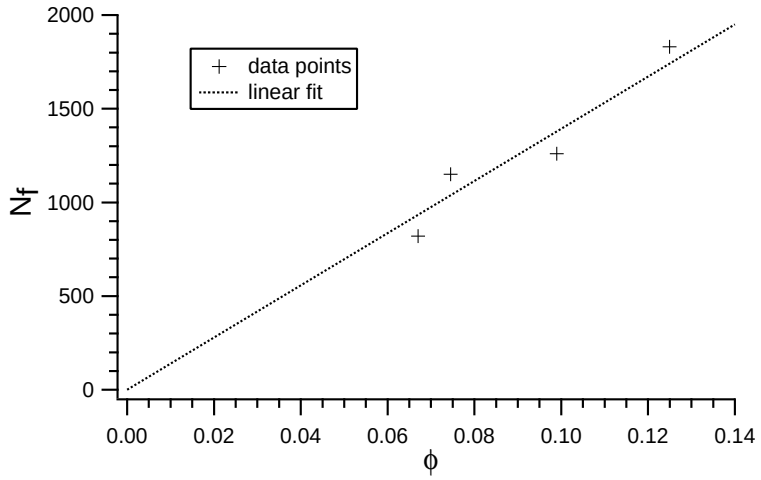

Figure 3.5: Features found vs volume fraction for Experiment S1: Features found in image were proportional to the local volume fraction ϕ, therefore, the four data point taken from different potential and ϕ should fall on one line passing through zero point. The four points (from low ϕ to high ϕ) correspond to high potentials of 250V, 220V, 280V and 300V.

to local volume fraction (ϕ), therefore, the four data points (N_f and corresponding ϕ) taken from different potentials at the maximum ϕ should fall on one line passing through zero point. Actually they did fall on one line and the error of the linear curve fit was 4.8%. Using the relation between N_f and ϕ, we optimized the values of brightness threshold cutoff for all ϕ and all potentials in one experiment so that the IDL generated N_f was very close to this expected value, within 5% error.

Separation Threshold

The diameter and separation setting in IDL procedures were determined using the line tool in ImageJ and the actual diameters of particles. For example, a diameter of 9 pixels and a separation of 9 pixels were used for 0.77 μm particle, 11 pixels and 13 pixels for 1.14 μm particle. The bond length used for IDL procedures were 11 pixels (i.e. 0.95 μm) for 0.77 μm particle, and 16 pixels (1.37 μm) for 1.14 μm particle.

Dipolar Energy

We calculated the bond density B and the angular order parameter $\langle \cos^2 \theta \rangle$ from the particle coordinates obtained from our confocal images. We then used simple do-loop procedures (these "macros" were written in the graphical analysis program, Igor Pro) to analyze all these data (Igor Pro procedures used are included in appendix B). The procedures consisted of operations on data for each value of electric fields with loops running through the analysis for data at all values of fields (see next subsection for detailed results).

This was a convenient way to study the physical parameters of interest of colloidal suspensions upon increasing electric field energy $\langle E^2 \rangle$, where $\langle E^2 \rangle = \langle \vec{E} \cdot \vec{E} \rangle$, and $\vec{E}$ is the center rms (root mean square) electric field. In all the linear field experiments the $\langle E^2 \rangle$ is simply half of the square of E_0 for Experiment S1 and Experiment L1 (where E_0 is the center field amplitude

of field), because:

$$\langle \vec{E} \cdot \vec{E} \rangle = \frac{E_0^2}{2\pi} \int_0^{2\pi} \cos^2\theta \, \mathrm{d}\theta = E_0^2/2 \ . \tag{3.6}$$

Although the center field amplitude E_0 was different for rotating field and linear field in Experiment S2, as we mentioned in 3.1.3, $\langle E^2 \rangle$ was the same for them because:

$$\langle \vec{E}^{rot} \cdot \vec{E}^{rot} \rangle = (E_0^{rot})^2 \cos^2\theta + (E_0^{rot})^2 \sin^2\theta = (E_0^{rot})^2 \ . \tag{3.7}$$

Given the same potential, the center linear field amplitude E_0^{lin} is $\sqrt{2}$ times larger than the center rotating field amplitude E_0^{rot} as:

$$(E_0^{rot})^2 = \left(\frac{E_0^{lin}}{\sqrt{2}} \right)^2 = (E_0^{lin})^2/2 = \langle \vec{E}^{lin} \cdot \vec{E}^{lin} \rangle \ . \tag{3.8}$$

So we have

$$\langle (E^{rot})^2 \rangle = \langle (E^{lin})^2 \rangle = E_0^2/2 \ , \tag{3.9}$$

where

$$E_0 = \frac{V_{pk}}{2d} \ . \tag{3.10}$$

V_{pk} here is the peak-to-peak potential, d is the distance between two linear electrodes. As we have seen in Equation 1.4, lambda parameter Λ is a good parameter representing dipolar energy, which is proportional to the field strength as shown in Equation 1.3. We plotted E_0 vs Λ for both sizes

of particles in Figure 3.6 for convenience of looking up corresponding field strength of Λ.

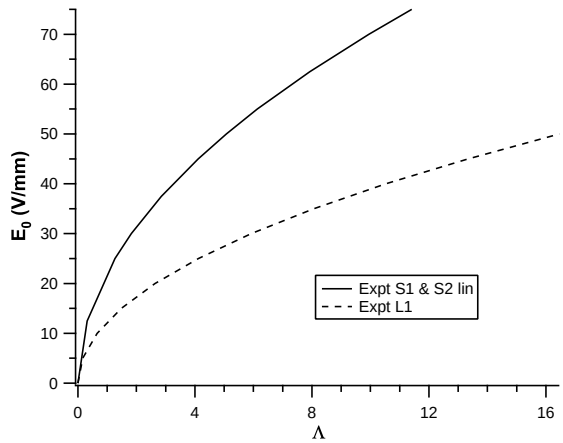

Figure 3.6: E_0 vs Λ: Experiment S1 and S2 was using 0.77 μm particles, and Experiment L1 was using 1.14 μm particles.

3.2.2 Order Parameter Analysis and Results

Here we present detailed analysis and results of our order parameters.

Bond Density

The bond density vs volume fraction ϕ for Experiment S1 is shown in Figure 3.7. For each value of potential in this experiment, bond density basically

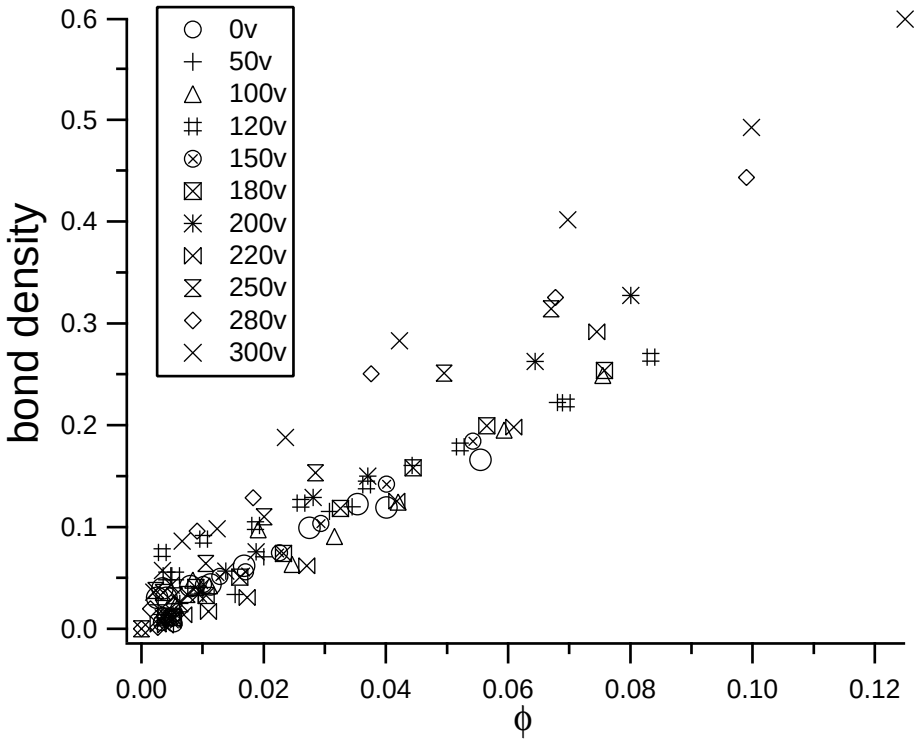

Figure 3.7: Experiment S1: Bond density vs ϕ profile. For each value of peak-to-peak potential in Experiment S1, bond density basically increased linearly with volume fraction, which was due to the decreasing distances between each pair of particles. For different potentials, it appeared that higher potential corresponded to a higher slope of the linear increase of bond density upon ϕ.

increased almost linearly with ϕ. Such an increase in bond density was indeed expected due to the decreasing distances between each pair of particles as the increasing potential caused increasing inter-particle attraction. For different potentials, it appeared that higher potential corresponded to a higher slope of the linear increase of bond density with ϕ. We expected the bond density (B) to have a ϕ dependence of the form $B = \beta_1\phi + \beta_2\phi^2$. The reason for this is as follows: When we use IDL to analyze a confocal image of colloids to calculate the bond density in this image, we define a bond length (L) as the standard of bonds (see 2.2.2 for details). In general, L is chosen to be slightly larger than actual bond length in real-space, as we do not want to miss any bonds due to too small a value of L. Therefore, if the actual diameter of the monodispersed particles is σ, then L chosen is slightly larger than σ. Then the actual volume of a particle (v) is slightly smaller than the volume it appears (v_e where the subscript "e" means extended volume), as shown in Figure 3.8. If we call the bond density B and the unbonded density U, then we always have $B + U = 1$. The B at zero field can be expressed as

$$B = \frac{Nv_e}{V} = N\frac{v_e}{v}\frac{v}{V} = \frac{v_e}{v}\phi \ , \tag{3.11}$$

where N is the number of bonded particles and V is the total volume of all particles. Moreover, as we define that when the distance between two particles (R) is smaller than L, i.e. when $R < L$, we say this two particles are "bonded". So there will be volume overlap of v_e when the distance of two

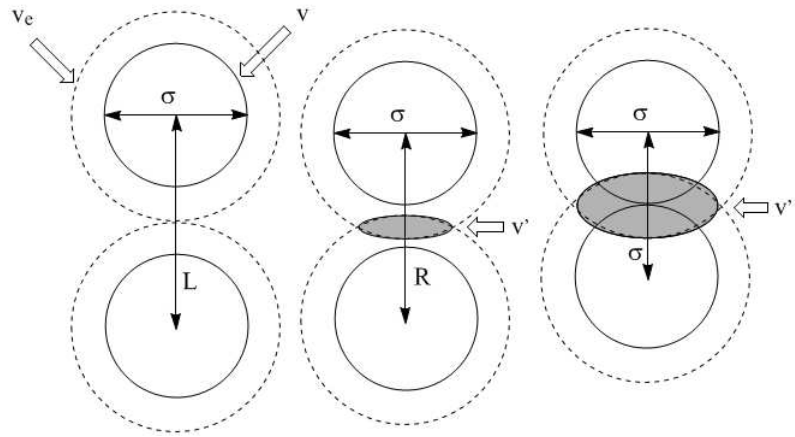

Figure 3.8: Two bonded particles. Define L as bond length, so long as particle separation R satisfy that $\sigma < R < L$, where σ is actual particle diameter, we say the two particles are bonded. v' is overlapped volume of v_e.

bonded particles satisfy $\sigma < R < L$, and we call this volume overlap v'. So the unbonded and bonded density considering overlap of extended volume can be expressed as

$$U' = 1 - \frac{v_e}{v}\phi + \frac{N}{2}\frac{v'}{V}B \tag{3.12}$$

and

$$\begin{aligned} B' &= 1 - U' \\ &= \frac{v_e}{v}\phi - \frac{N}{2}\frac{v'}{V}B \\ &= \frac{v_e}{v}\phi - \frac{1}{2}\frac{v'v_e}{v^2}\phi^2 \\ &= \beta_1\phi + \beta_2\phi^2 \ . \end{aligned}$$

Therefore, we used polynomial fitting $B = \beta_0 + \beta_1\phi + \beta_2\phi^2$ for our bond density profiles (such as Figures 3.7 and 3.9), constraining $\beta_0 = 0$, $\beta_1 > 0$, and $\beta_2 < 0$. In the presence of an external field the actual B will be higher than that at zero field, so an increasing β_1 with increasing field was expected.

The polynomial fit of bond density vs ϕ profile showed its advantage especially at Experiment L1 (as shown in Figure 3.9) where a nonlinearity rose up at high field: At high enough ϕ ($\phi \gtrsim 20\%$) particles in a confocal image appear close to each other and bond density B will reach its maximum at this point, after where increasing ϕ will only decrease B. For high fields, not only the high ϕ points behave nonlinearly, the points at low ϕ ($\phi \lesssim 2\%$) also increase nonlinearly with ϕ. The reason for this was due to the stronger dipolar interaction between particles (for 1.14 μm particles) for high field cases in Experiment L1, as the strength of the interaction was proportional to the cube of particle diameter. Therefore, very few particles at low ϕ situation could still form bonds and led to a high bond density at high enough fields.

In Figure 3.10, we present all the results of β_1 vs lambda parameter Λ (described in Equation 1.3) from the three experiments to see how β_1 behaves in different fields and if there is any threshold-like behavior. Since each particle should has the same weight in the curve fitting of bond density profiles, we used $C\sqrt{N}$ (where N was the local particle number and C was a constant) as the weight for the polynomial fit function, producing the same error of

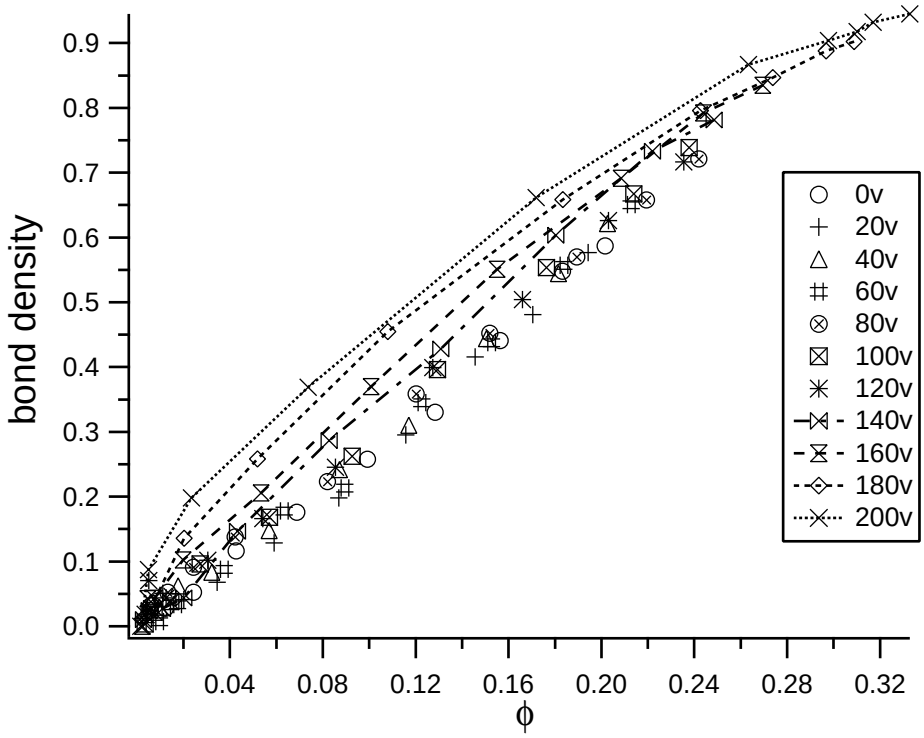

Figure 3.9: Experiment L1: Bond density vs volume fraction profile. Here we can see the nonlinear effect at high fields.

β_1 (the error bars shown in Figure 3.10) as that produced without weighting with a proper C.

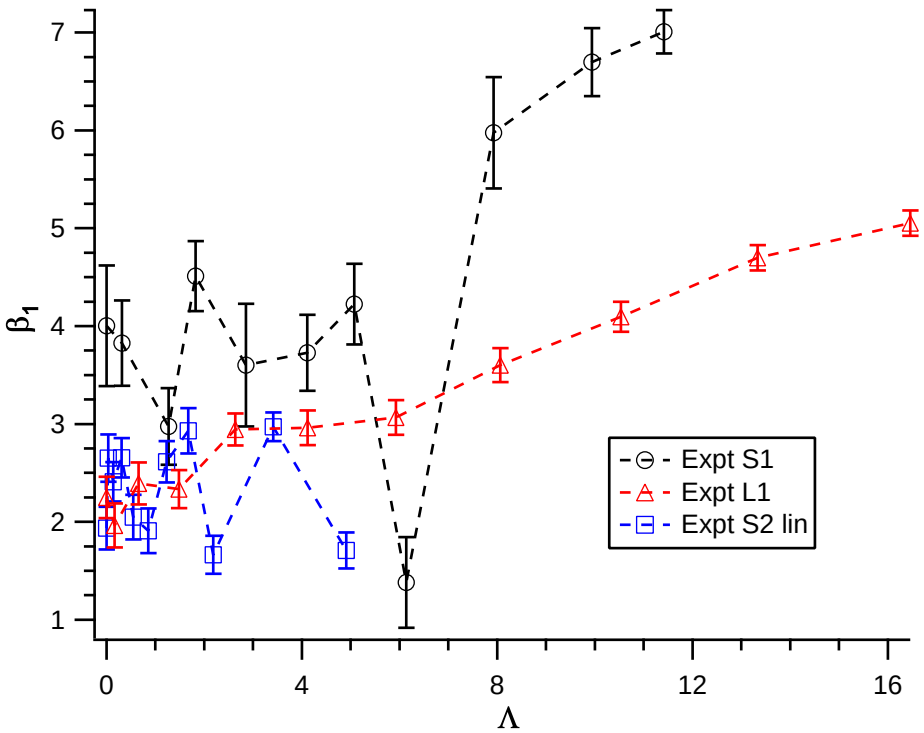

Figure 3.10: β_1 vs Λ. Particle sizes: 0.77 μm for Experiment S1 and S2, 1.14 μm for L1. Fields applied were linear for Experiments S1 and L1. For Experiment 2 "lin" means linear field.

From Figure 3.10 we can see that β_1 increases with dipolar interaction energy to a value 150% of the zero field value when $\Lambda > 6$, except Experiment S2 in which the field could not be increased too much because of the heating problem we mentioned in 2.3.2. At low Λ ($\Lambda < 6$), β_1 stays steady at approximately 2 - 4 for 0.77 μm particles. But this steady stage of β_1 is not clear

for 1.14 μm particles. Although we expected the result from Experiment S2 would collapse on that of Experiment S1 as they were using the same size particles, actually there is an obvious difference in β_1 vs Λ diagram for S1 and S2. The difference between S1 and L1 in β_1 is understandable because β_1 is sensitive to v_e chosen for IDL calculation and the actual v of particles.

Bond Angular Order Parameter

Bond angular order parameter $\langle \cos^2 \theta \rangle$ was obtained for both 0.77 μm and 1.14 μm particles as a function of local volume fraction ϕ. The $\langle \cos^2 \theta \rangle$ vs ϕ profile for Experiment S1 is presented in Figure 3.11. For each value of

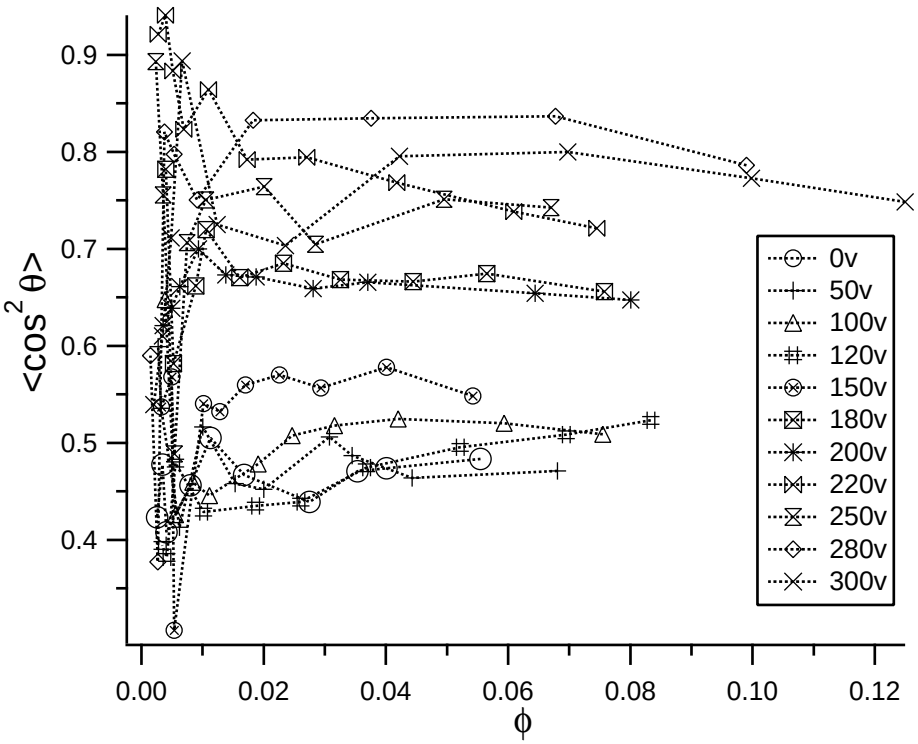

Figure 3.11: Experiment S1: $\langle \cos^2 \theta \rangle$ vs ϕ profile. For each value of potential in Experiment S1, the angular order parameter $\langle \cos^2 \theta \rangle$ was basically constant for different ϕ, except at the low ϕ ($\phi < 0.02$) where the small number of bonds resulted in poor statistics. Higher potential corresponded to a higher average value of $\langle \cos^2 \theta \rangle$.

potential, $\langle \cos^2 \theta \rangle$ was roughly constant for different ϕ, except at the low ϕ ($\phi < 0.02$) part where the small number of bonds resulted in poor statistics.

For different potentials, it appeared that higher potential corresponded to a higher average value of $\langle \cos^2 \theta \rangle$, which can be understood because particles were more likely to form chains parallel to the field direction at higher fields ($\langle \cos^2 \theta \rangle = 1$ for a perfect particle chain, along y axis and parallel to the linear field).

For larger particles (Figure 3.12), a significant decrease (roughly linear) in $\langle \cos^2 \theta \rangle$ is seen at high fields. The reason was closely related to that for the

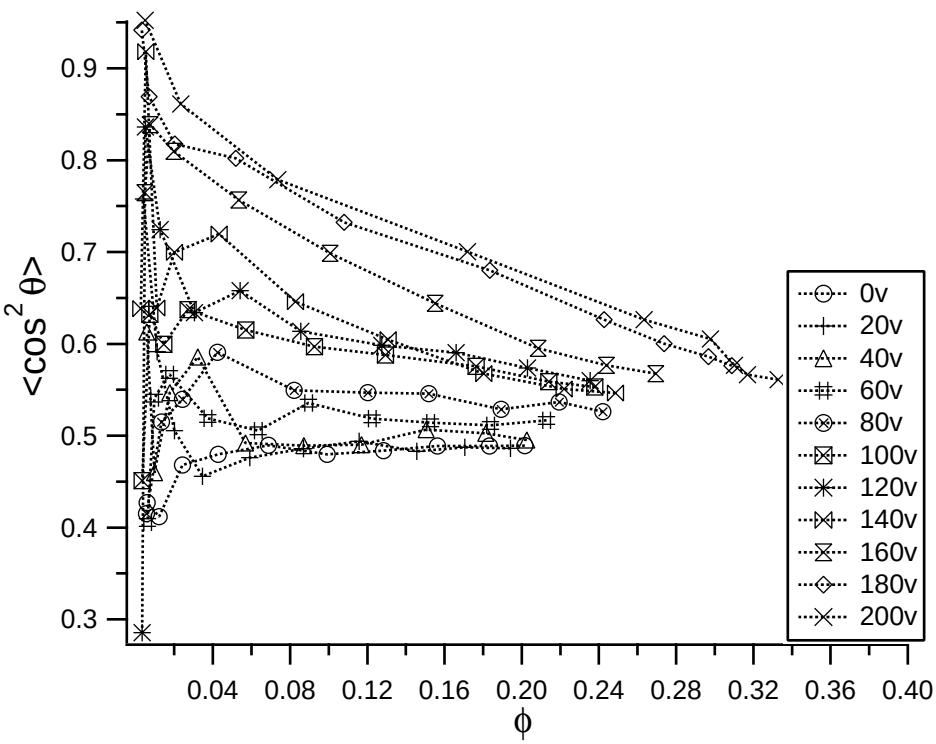

Figure 3.12: Bond angle parameter vs volume fraction profile for Experiment L1 (1.14 μm): here we can see even at high volume fraction, $\langle \cos^2 \theta \rangle$ still behaves linearly even the line starts to be tilted at high volume fraction and field.

nonlinearity of bond density profile in Experiment L1:

- At high ϕ, there is a systematic effect on both bond density profile and $\langle \cos^2 \theta \rangle$ profile.
  - First, for large ϕ ($\phi > 20\%$ in Experiment L1), there is a nonlinearity in bond density that arises from the onset of saturation of bonds (Figure 3.9).
  - As this happens, the system also evolves toward close-packing where $\langle \cos^2 \theta \rangle = 0.5$ for both random orientations as well as a hexagonal close packed structure. Thus at high ϕ there is a systematic decrease in $\langle \cos^2 \theta \rangle$.
- At high fields, the nonlinearity becomes more obvious in Experiment L1 because larger particles experience stronger attraction induced by external field. Therefore even at low ϕ we can see the nonlinearity of bond density profile in Figure 3.9 and the dramatically high $\langle \cos^2 \theta \rangle$ in Figure 3.12, providing the field is high enough.

Because $\langle \cos^2 \theta \rangle$ vs ϕ profiles were generally linear for all experiments, we took the intercept of linear fit, α_0, as a representative value of $\langle \cos^2 \theta \rangle$ ($\alpha_0 = \langle \cos^2 \theta \rangle|_{\phi=0}$). α_0 is plotted vs Λ in Figure 3.13 for all experiments. The theoretical zero field value of α_0 should be 0.5 because in 2 dimensions

$$\frac{\int_0^{2\pi} \cos^2 \theta \, d\theta}{2\pi} = 0.5 \tag{3.13}$$

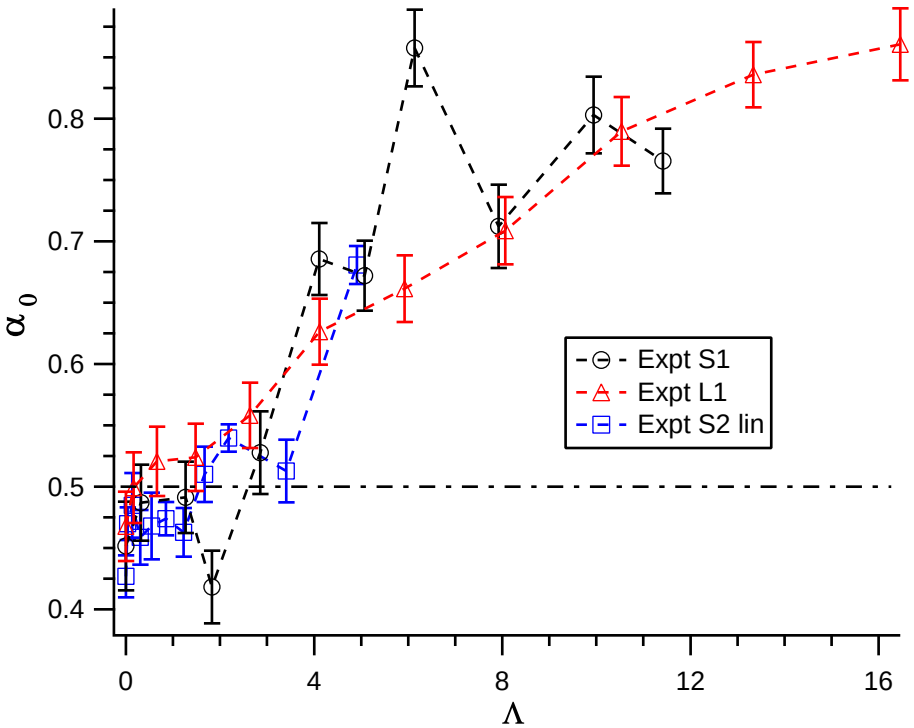

Figure 3.13: α_0 vs Λ: The data from three experiments basically fell on one curve, which might indicate the dipolar interaction are still applicable in our study.

However, our starting value was always slightly smaller than 0.5 in all 3 experiments, which we do not understand yet.

If the dipolar interaction was applicable in our case, we would expect α_0 plotted against the dipolar strength Λ to be independent of particle size, i.e. the increase of α_0 upon Λ from all three linear experiments shall collapse onto one master curve. Because the orientations of bonds were more parallel to the field direction as the dipolar energy became stronger. In fact, the data in Figure 3.13 from linear field experiments of different particle sizes do collapse onto one curve. This suggests that the point-dipolar approximation in Equation 1.2 is applicable for the colloids in our study.

For rotating field in Experiment S2, α_0 stayed almost steady over the whole range of applied field energy. This is expected because no direction in the x-y plane is preferred in a rotating field. There was a slight decrease with increasing field energy, which is expected because the four electrodes creating the rotating field were not perfectly symmetric about the center (see 2.3.2) but wider separated in the direction perpendicular to the reference of θ (i.e. the averaged field direction actually slightly preferred x direction than y direction). To show the difference between linear and rotating fields in Experiment S2, we plotted α_0 vs $\langle E^2 \rangle$ for this experiment and show it in Figure 3.14.

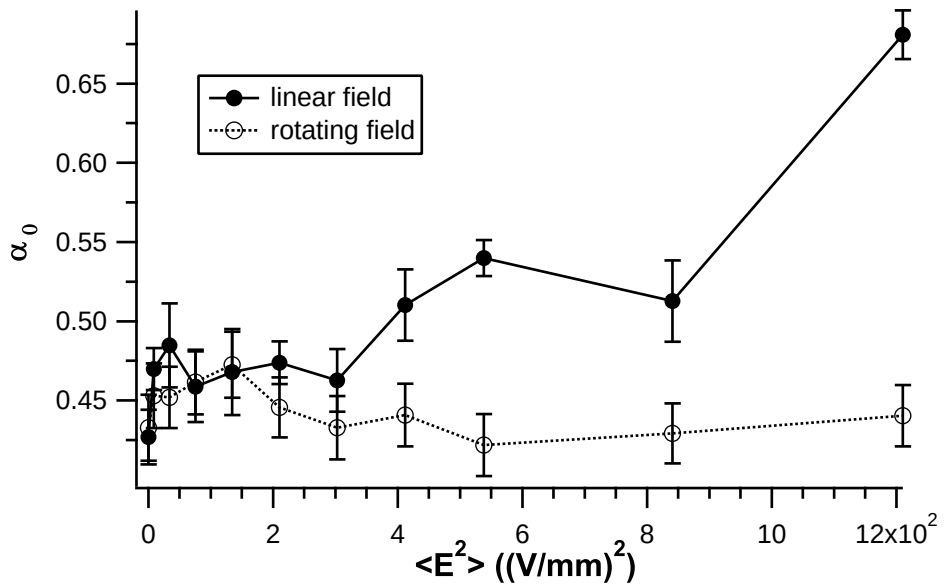

Figure 3.14: Experiment S2 (0.77 μm): α_0 vs $\langle E^2 \rangle$. The linear α_0 stays constant and starts to increase linearly from approximately 350 (V/mm)^2, which can be considered as a threshold. The rotating α_0 is roughly constant as expected. Here the maximum $\langle E^2 \rangle$, approximately 1200 (V/mm)^2, corresponds to $\Lambda \approx 5$.

Pair Correlation Function

We calculated the pair correlation in the three experiments according to the following procedure:

- Pair correlation calculation. Use the same diameter and separation settings of IDL procedure as mentioned in 3.2.1, calculate g(r) with 1 pixel resolution (i.e. Δr = 1 pixel, see 2.2.2 for more details). We calculated the data for $\phi_0 = 5\%$ for 0.77 μm particles (Experiments 1 and 3) and $\phi_0 = 11\%$ for 1.14 μm particles (Experiment L1), which both corresponded to approximately 600 particles in each frame of image. Since we obtained data at discrete values of ϕ, we picked two ϕ values ϕ_a and ϕ_b enclosing ϕ_0 (i.e. $\phi_0 \in (\phi_a, \phi_b)$) for each value of field to calculate g(r) at ϕ_0 by interpolation.

- Load data into Igor Pro. Two columns of data, r (possible distance between particles) and g(r), were produced from IDL calculation. They were named in sequence of field strength for the convenience of Igor Pro macros when looping over field energy.

- First peak of g(r). We were interested in the value of the pair correlation function at the first peak ($g(r_f)$) and the corresponding position (r_f), which indicated the most probable distance between particles. We used macros to interpolate and smooth g(r), and found the r_f and $g(r_f)$. By running the analysis in a loop for all the field values we applied, we obtained the relation of r_f and $g(r_f)$ versus Λ for ϕ_a and ϕ_b. We then

linearly fitted these data for ϕ_a and ϕ_b, then interpolate in order to obtain the value for ϕ_0.

Results for Experiment S1 are shown in Figures 3.15 and 3.17. As we increased the field, r_f deceased, and $g(r_f)$ increased. This is because the interparticle attraction becomes stronger, and the particles come closer to each other when the field energy becomes stronger. The first peak at zero field, as shown in Figure 3.15, was not sharp, which led to a large and inaccurate r_f. As the field energy was increased, r_f was relatively constant at r/$\sigma \approx 1.6$; it began to decrease toward 1 above $\Lambda \approx 6$. On the other hand, $g(r_f)$ stayed constant at approximately 1.05 - 1.10 and increased to approximately 1.35 at higher fields.

Results for Experiment L1 are shown in Figures 3.16 and 3.17. As we increased the field, r_f deceased gradually instead of having a steady range as Experiment S1, and $g(r_f)$ increased after a short steady range at the beginning Λ.

We plot r_f and $g(r_f)$ vs Λ for all linear experiments in Figures 3.17a and 3.17b. By doing this, we can obtain the general information for all experiments regardless of the different particle size used. There is no other similarity of r_f for Experiments S1 and L1 except both r_f collapse to 1 at

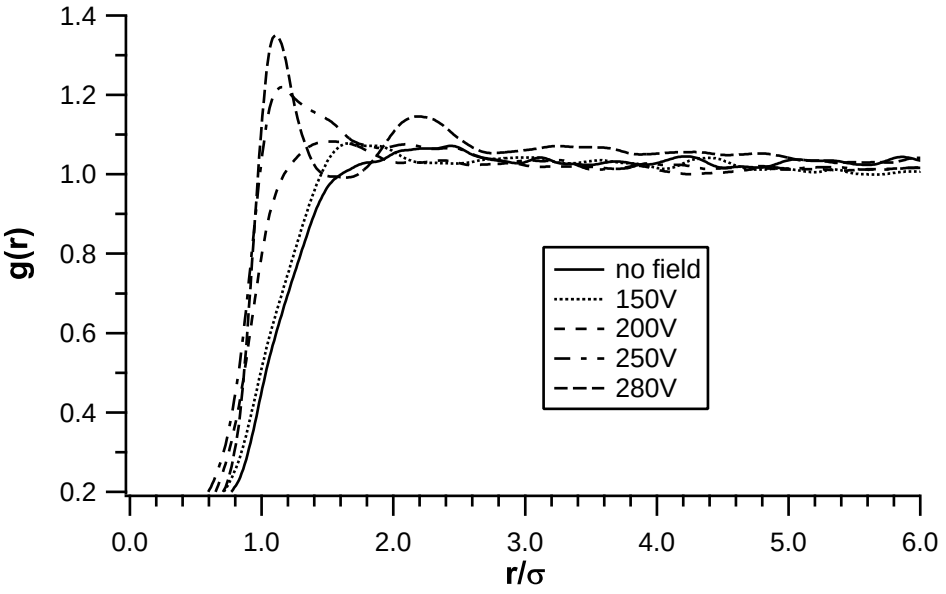

Figure 3.15: g(r) vs r/σ in Experiment S1. σ here is particle diameter, 0.77 μm. As we increased the field, r_f deceased, and $g(r_f)$ increased. Because when field energy became stronger, the attraction between particles became stronger and came closer to each other.

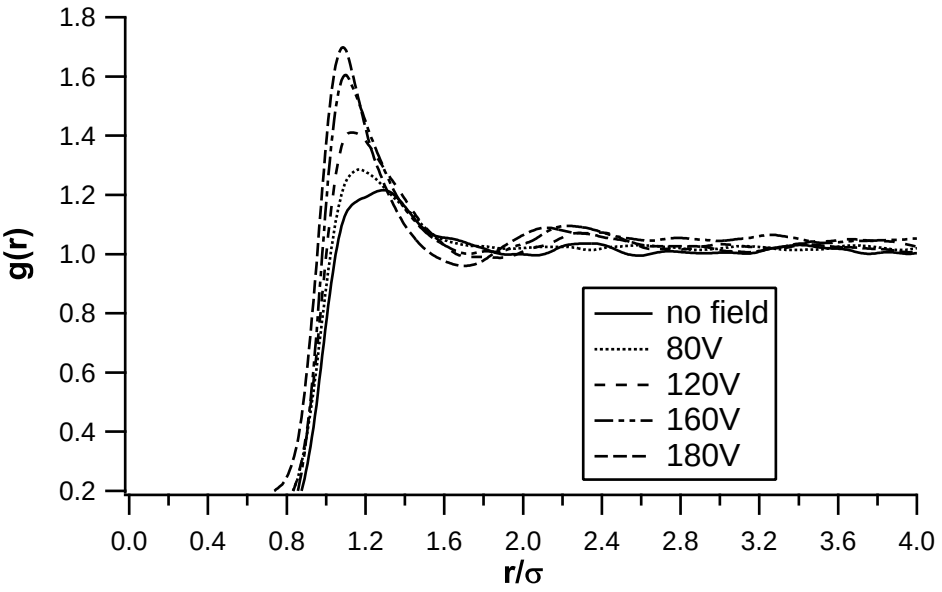

Figure 3.16: g(r) vs r/σ in Experiment L1. $\sigma = 1.14\mu$m.

high enough dipolar energy. The $g(r_f)$ for these two experiments increase similarly toward a liquid-like state with increasing dipolar energy. There is a systematic shift in $g(r_f)$ due to the difference in local volume fraction (ϕ_0) in the confocal images we used from S1 and L1.

The results of Experiment S2 shows no obvious increase or decrease of r_f or $g(r_f)$ upon Λ. This can be understood because in Experiment S2 we only increased Λ up to $\Lambda \approx 5$, where for Experiment S1 (same particle size) r_f and $g(r_f)$ are still steady. r_f of S2 collapse into that of S1 as expected. However, $g(r_f)$ is more sensitive to local volume fraction so that $g(r_f)$ of S2 does not perfectly collapse on S1 due to errors in volume fraction determination.

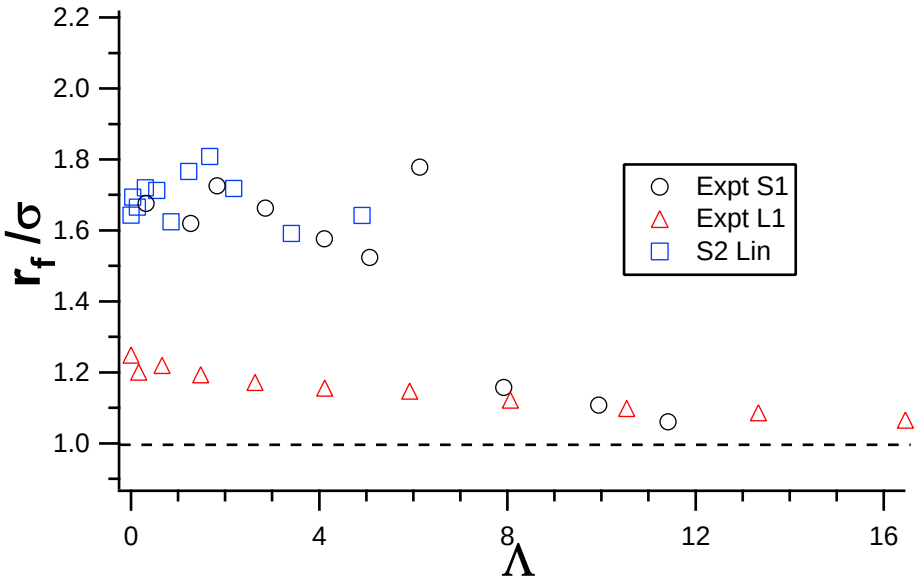

(a) r_f/σ vs Λ.

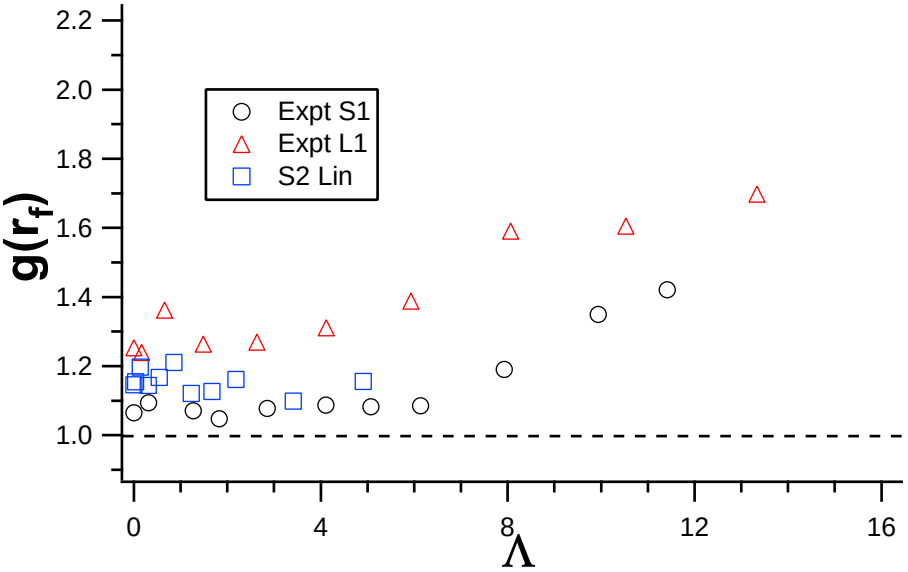

(b) $g(r_f)$ vs Λ.

Figure 3.17: Pair correlation function at the first peak for Experiments S1, S2 and L1. The particle size (diameter) for Experiment S1 and S2 is 0.77 μm, and for Experiment L1 is 1.14 μm.

Osmotic Compressibility

We studied the equilibrium sedimentation profile of colloidal silica particles, using the vertical density profiles (see 2.2.2 and 3.1.3 for more details), to calculate isothermal osmotic compressibility of our colloidal system and to study its dependence on field energy.

In a colloidal silica suspension at sedimentation equilibrium, we can measure the local particle density $n(z)$, where z is the vertical coordinate measured from the bottom of the sediment, and from it, calculate the osmotic pressure of the system $\Pi(z)$. The osmotic equilibrium condition is [38], [39]

$$\frac{\mathrm{d}\Pi(z)}{\mathrm{d}z} = -mgn(z) \ . \tag{3.14}$$

Under isothermal conditions, Π depends only on $n(z)$, therefore, Equation 3.14 can be written as

$$\frac{\mathrm{d}n(z)}{\mathrm{d}z} = -l_g^{-1}\chi_{\mathrm{T}}n(z) \ , \tag{3.15}$$

where $\chi_{\mathrm{T}} = k_{\mathrm{B}}T(\partial\Pi/\partial n)_T^{-1}$ is the isothermal osmotic compressibility, and $l_g = k_{\mathrm{B}}T/mg$ is the gravitational length. In the dilute gas limit ($\chi_{\mathrm{T}} = 1$) we can obtain from Equation 3.15 the barometric law:

$$n(z) = n_0 \exp[-\frac{z}{l_g}] \ . \tag{3.16}$$

We rewrite Equation 3.15 as

$$\ln(n(z)) = \ln(n_0) - z\, l_g^{-1} \chi_{\mathrm{T}} \tag{3.17}$$

for our analysis below.

The gravitational length lg for 0.77 μm particle is calculated to be 1.92 μm, and for 1.14 μm particle is 0.59 μm, and the estimated error is 14%.

We studied the top part of the sediments (the tail of the density profile in Figure 3.18), where colloidal particles were few enough to behave like fluid and we could fit to a exponential curve as Equation 3.16. We linearly fitted $\ln \phi$ vs z (as shown in Equation 3.17) instead of direct exponential fitting, which put more weight for particles at higher ϕ. $\phi(z)$ and number density $n(z)$ only differ in a constant, i.e. the single particle volume, so they are equivalent for this purpose.

We obtained the χ_{T} from the slope of the linear fitting, plot the χ_{T} vs Λ in Figure 3.19 and observe these effects:

- With increasing field, χ_{T} increases almost linearly. This can be explained as: because of increasing field energy, the inter-particle attraction increases, so the colloids appear to be easier to compress, i.e. a larger apparent compressibility.

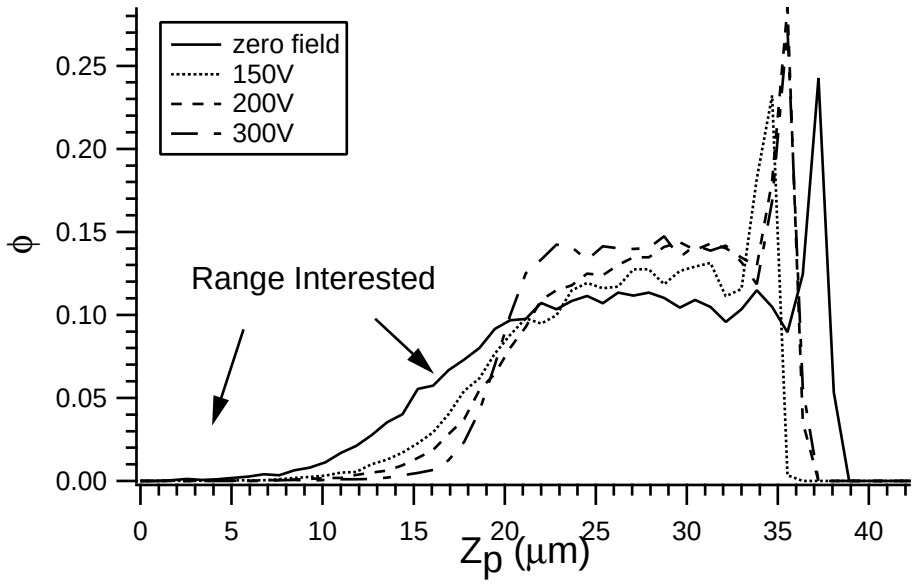

Figure 3.18: Experiment S1: ϕ vs Z_p. We observed that as we increase the field strength, the sedimentation profile became sharper. This is due to the increasing dipolar attraction between the particles which makes the particles floating on the top sediment down. The sedimentation profiles here are inversed along z from original data for the convenience of χ_{T} calculation. The "Range Interested" is roughly the range for χ_{T} calculation where the sedimentation profile is exponentially increasing. Note that Z_p is depth in real-space. $Z_p = z_0 - z$ where z is shown in Equation 3.17 and z_0 is a constant which does not affect our results.

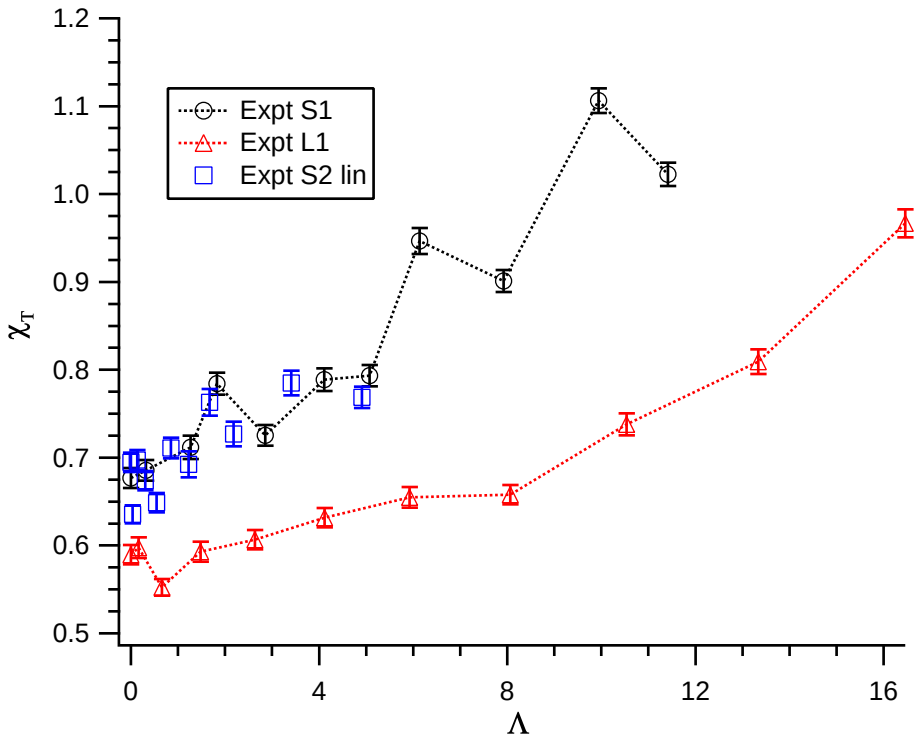

Figure 3.19: Isothermal compressibility χ_T (calculated from exponential tail of density profiles such as those in Figure 3.18) as a function of dipolar strength Λ.

- At zero field, all χ_{T} are smaller than 1, which means our systems cannot be considered as ideal gas or hard spheres at low ϕ. Softness (i.e. the repulsion in interaction potential) is a possible reason for the decrease of χ_{T}. Although our systems are very close to hard spheres ($\kappa^{-1} \approx 50nm$), deviations from ideal hard-sphere behaviors can cause small decrease in χ_{T}. Indeed these deviations are also observed in the position of the first peak of the pair correlation functions being much larger than 1 (i.e. $r_f/\sigma > 1$).

- χ_{T} for 1.14 μm particles is systematically smaller than that for 0.77 μm particles. This is reasonable because at a given number density, the effective hard-sphere repulsion is more important for larger spheres, which can make the colloidal system more difficult to compress, i.e. a smaller χ_{T}.

- The error in the determination of particle size (within 5%) and material density can cause systematic error in the gravitational length l_g, which can affect our calculation.

3.3 Conclusions

In this thesis, we have synthesized fluorescent-labeled colloids, constructed samples and software for confocal microscopy experiments, and conducted experiments where we study the behavior of quiescent colloidal sediments as well as the response of the colloidal suspension to and external electric field.

In the studies of quiescent colloidal sedimentation profiles, we observed unexpected plateau region (Figure 3.18). A further analysis of the exponential region of these sedimentation profiles showed that the values of the isothermal osmotic compressibility χ_{T} at zero-field were smaller than 1 for both 0.77 μm and 1.14 μm colloids (Figure 3.19), which indicated that our systems were not perfectly hard-sphere like.

Next, we studied colloidal ordering in the presence of a high-frequency (MHz) AC field of variable strength characterized by a dipolar strength parameter Λ (because we assumed a dipolar inter-particle interaction). For our electric field studies, we used not only the pair correlation functions but also, various bond order parameters, and isothermal osmotic compressibility, which helped us to quantify field-induced structure. We did not know beforehand which order parameter would give us the most information. We tried two bond order parameters (bond density and bond angular parameters) as described below.

The bond density parameter $\boldsymbol{\beta_1}$: The plot of the bond density parameter β_1 vs the dipolar energy parameter Λ diagram (Figure 3.10) exhibits a steady low field value for 0.77 μm experiments (S1 and S2). At high Λ, β_1 in both Experiments S1 and L1 rises to approximately 150% of the zero field value. We were unable to increase the rotating field to a high value due to sample-heating problems, so there is no high field data for Experiment S2. β_1 from all experiments did not collapse into one curve, but this is expected as β_1 is sensitive to the parameters chosen for bond density calculation; these parameters vary a bit from experiment to experiment.

The bond angular parameter $\boldsymbol{\alpha_0}$: The extrapolation of ϕ-dependence of $\langle\cos^2\theta\rangle$ to zero ϕ, α_0, turned out to be a self-consistent way to compare all experiment and superior to the bond density parameter β_1. For experiments where the $\langle\cos^2\theta\rangle$ vs ϕ profiles were flat, α_0 was also close to the average $\langle\cos^2\theta\rangle$. But we used α_0 instead of average $\langle\cos^2\theta\rangle$ because α_0 is less sensitive to the shape of $\langle\cos^2\theta\rangle$ vs ϕ profiles. We note the following:

- For linear fields, α_0 increases from random bond-orientation ($\alpha_0 \approx 0.5$) to highly anisotropic along the field direction ($\alpha_0 > 0.8$). All linear experiments (different particle sizes) had α_0 vs Λ curves that collapsed onto one master curve (Figure 3.13). This is a strong indication that, at least at these field values, the dipolar approximation is valid. Moreover, the Λ parameter at the onset for chain formation is approximately 6

instead of 1. Thus although the dipolar approximation is valid, we must still view it as an effective dipolar interaction.

- For rotating fields, bond orientation was absent as expected, causing α_0 to be different from linear field results in the same sample (Figure 3.14).

In summary, we found that while β_1 was very sensitive to software parameters, α_0 was a robust parameter that accurately reflected colloidal response to an electric field. When plotted against a dipolar strength parameter (which has all particle size dependence absorbed), results for different particle sizes fall on one curve. This suggests strongly the validity of the dipolar interaction. Moreover, we proved that we can switch the colloidal system between anisotropic phase and isotropic phase by switching the external electric field directions between linear and rotating.

The pair correlation function $g(r)$: The results from pair correlation function calculation supported that as field energy increases, more particles come closer to each other due to the increased inter-particle attraction. The position of the first peak of g(r), r_f, approached the particle diameters, i.e. $r_f/\sigma \rightarrow 1$, as the external field was increased. The magnitude of $g(r_f)$ also increased with field, with the structure approaching liquid-like behaviors (Figure 3.17).

The isothermal compressibility $\chi_{\mathbf{T}}$: In the presence of an external high-frequency AC field, χ_{T} increased dramatically at moderate values of Λ (Figure 3.19). Increase in χ_{T} is reasonable: increasing Λ increases dipole-dipole interaction which compresses the colloidal sediment.

Outlook

The experiments described in this thesis quantify colloid structure at low volume fractions in the presence of gravity and low electric fields. First, the measurements presented make quantitative statements about structure in a quiescent colloidal sediment. Several questions remain to be definitively answered:

- What causes the plateau region? We already know that there must be an inter-particle repulsion (from pair correlation as well as the less-than-unity zero-field value of χ_{T}). Could this cause the plateau region or must van der Waals attraction be taken into account? Comparison of experiments with computer simulations currently under way could shed light on this.

- Why is the isothermal compressibility χ_{T} at zero field lower than unity? The could be caused by the softness of the zero-field interaction potential. While we estimated $\kappa^{-1} < 50$ nm, we nevertheless observed that the first peak of pair correlation function g(r) was at $r_f/\sigma \approx 1.6$ for 0.77 μm diameter colloidal particles. It is reasonable that softness decreases compressibility: again a comparison with simulation would be interesting.

Second, while the field-induced structure appears to be consistent with dipolar interaction, it is nevertheless curious that colloids feel the presence of the

electric field at $\Lambda \approx O(10)$ rather than $O(1)$.

Finally, we successfully tested modification of interactions in a rotating electric field. But we still have problem to solve such as:

- modify cell to achieve higher fields,
- study phase behavior in rotating fields.

Bibliography

[1] W. B. Russel, D. A. Saville, and W. R. Schowalter. *Colloidal Dispersions*. Cambridge University Press, 1989.

[2] D. Fennell Evans and H. Wennerström. *The Colloidal Domain: Where Physics, Chemistry, Biology, and Technology Meet*. Advances in Interfacial Engineering. VCH, 1994.

[3] A. Vrij, E. A. Nieuwenhuis, H. M. Fijnaut, and W. G. M. Agterof. Application of modern concepts in liquid state theory to concentrated particle dispersions. *Faraday Discuss.*, 65:101–113, 1978.

[4] P. N. Pusey and W. van Megen. Phase behaviour of concentrated suspensions of nearly hard colloidal spheres. *Nature*, 320:340–342, 1986.

[5] P. N. Pusey and W. van Megen. Observation of a glass transition in suspensions of spherical colloidal particles. *Phys. Rev. Lett.*, 59(18):2083–2086, 1987.

[6] V. Prasad, D. Semwogerere, and E. Weeks. Confocal microscopy of colloids. *J. Phys.: Condens. Matter*, 19, 2007.

[7] T. G. M. van de Ven. *Colloidal Hydrodynamics*. Colloid Science. Academic Press, 1988.

[8] H.C. Hamaker. The London – van der Waals attraction between spherical particles. *Physica*, 4(10):1058–1072, 1937.

[9] Malvern Instruments Website. http://www.malvern.com /labeng /industry /colloids /dlvo_theory.htm.

[10] A. Hynninen and M. Dijkstra. Phase behavior of dipolar hard and soft spheres. *Phys. Rev. E*, 72(5), 2005.

[11] A. Yethiraj. Tunable colloids: control of colloidal phase transitions with tunable interactions. *Soft Matter*, 3:1099–1115, 2007.

[12] R. Tao, J. T. Woestman, and N. K. Jaggi. Electric field induced solidification. *Appl. Phys. Lett.*, 55(18):1844–1846, 1989.

[13] R. Tao and J. M. Sun. Three-dimensional structure of induced electrorheological solid. *Phys. Rev. Lett.*, 67(3):398–401, 1991.

[14] R. Tao and J. M. Sun. Ground state of electrorheological fluids from monte carlo simulations. *Phys. Rev. A*, 44(10):R6181–R6184, 1991.

[15] T. Chen, R. N. Zitter, and R. Tao. Laser diffraction determination of the crystalline structure of an electrorheological fluid. *Phys. Rev. Lett.*, 68(16):2555–2558, 1992.

[16] U. Dassanayake, S. Fraden, and A. van Blaaderen. Structure of electrorheological fluids. *J. Chem. Phys.*, 112(8):3851–3858, 2000.

[17] A. Yethiraj and A. van Blaaderen. A colloidal model system with an interaction tunable from hard sphere to soft and dipolar. *Nature*, 421:513–517, 2003.

[18] A. Yethiraj, A. Wouterse, B. Groh, and A. van Blaaderen. Nature of an electric-field-induced colloidal martensitic transition. *Phys. Rev. Lett.*, 92(5), 2004.

[19] S. Fraden, A. J. Hurd, and R. B. Meyer. Electric-field-induced association of colloidal particles. *Phys. Rev. Lett.*, 63(21):2373–2376, 1989.

[20] G. Bossis, C. Métayer, and A. Zubarev. Analysis of chaining structures in colloidal suspensions subjected to an electric field. *Phys. Rev. E*, 67(041401), 2007.

[21] J. C. van der Werff and C. G. de Kruif. Hard-sphere colloidal dispersions: The scaling of rheological properties with particle size, volume fraction, and shear rate. *J. Rheol.*, 33(3):421–454, 1989.

[22] T. G. Mason and D. A. Weitz. Optical measurements of frequency-dependent linear viscoelastic moduli of complex fluids. *Phys. Rev. Lett.*, 74(7):1250–1253, 1995.

[23] J. C. Crocker, M. T. Valentine, E. R. Weeks, T. Gisler, P. D. Kaplan, A. G. Yodh, and D. A. Weitz. Two-point microrheology of inhomogeneous soft materials. *Phys. Rev. Lett.*, 85(4):888–891, 2000.

[24] J. Hoogenboom. *Colloidal Epitaxy: A Real-Space Analysis*. PhD thesis, Universiteit Utrecht, 2002.

[25] M. Born and E. Wolf. *Principles of Optics*. Cambridge U. Press, Cambridge, 7th expanded edition, 1999.

[26] W. Stöber, A. Fink, and E. Bohn. Controlled growth of monodisperse silica spheres in micron size range. *J. Colloid Interface Sci.*, 26(62), 1968.

[27] H. Giesche. Synthesis of monodispersed silica powders i: particle properties and reaction kinetics. *J. Eur. Ceram. Soc.*, 14(3):189–204, 1994.

[28] H. Giesche. Synthesis of monodispersed silica powders ii: controlled growth reactions and continuous production processes. *J. Eur. Ceram. Soc.*, 14(3):205–214, 1994.

[29] D. 't Hart. Inverse silicon air sphere photonic crystals. Chapter 3: Synthesis of silica colloids. Master's thesis, Utrecht University, January 2004.

[30] A. van Blaaderen and A. Vrij. Synthesis and characterization of colloidal dispersions of fluorescent monodisperse silica spheres. *Langmuir*, 8:2921–2931, 1992.

[31] J. W. Zubrick. *The Organic Chem Lab Survival Manual*. John Wiley & Sons, Inc., sixth edition, 2004.

[32] N. A. M. Verhaegh and A. van Blaaderen. Dispersions of rhodamine-labeled silica spheres - synthesis, characterization, and fluorescence confocal scanning laser microscopy. *Langmuir*, 10:1427–1438, 1994.

[33] Mandel Scientific Company Inc. http://www.mandel.ca/products/ liquid_handling/pumps_tubing/tubing/index.htm.

[34] Solutions At Work For You. *Minipuls 3 Peristaltic Pump User's Guide*. Gilson.

[35] J. Crocker and D. Grier. Methods of digital video microscopy for colloidal studies. *J. Colloid Interface Sci.*, 179:298–310, 1996.

[36] J. Crocker and E. Weeks. http://www.physics.emory.edu/∼weeks/idl/index.html.

[37] J. O'M. Bockris and A. K. N. Reddy. *Modern Electrochemistry*, volume 1. Plenum Press, second edition, 1998.

[38] R. Piazza, T. Bellini, and V. Degiorgio. Equilibrium sedimentation profiles of screened charged colloids - a test of the hard-sphere equation of state. *Phys. Rev. Lett.*, 71(25):4267–4270, 1993.

[39] V. Degiorgio, R. Piazza, and T. Bellini. Depolarized light-scattering study of equilibrium sedimentation profiles of colloidal dispersions. *Nuovo Cimento D*, 16(8):1091–1101, 1994.

Appendix A

IDL procedures

Appendix B

Igor Pro procedures